MODIFIED-TiO_2 PHOTOCATALYTIC MEMBRANE FOR DISINFECTION AND DEGRADATION OF ORGANIC POLLUTANTS IN WASTEWATER

By

NELSON KIPCHUMBA

A Thesis Submitted to the School of Engineering, Department of Chemical and Process Engineering in Partial Fulfillment of the Requirements for the Degree of Master of Science in Chemical Engineering

Moi University

2023

DECLARATION

Declaration by the Student

This thesis is my original work and has not been presented for a degree in any other university. No part of this thesis may be reproduced without prior written permission of the author and/or Moi University.

Signature:_____Date: _____

Nelson Kipchumba

MSC/CE/5520/21

Declaration by the Supervisors

We declare that this thesis has been submitted for examination with our approval as university supervisors.

Signature:_____Date: _____

Dr. Cleophas Achisa Mecha

Department of Chemical & Process Engineering,

School of Engineering,

Moi University, Kenya

Signature:_____Date: _____

For Prof. Er. Anil Kumar

Department of Chemical & Process Engineering,

School of Engineering,

Moi University, Kenya

DEDICATIONS

I dedicate this thesis to Brielle, Bradley, Meghan and Maxwell. Be inspired.

ACKNOWLEGEMENTS

I would like to express my sincere gratitude and appreciation to the following for their contributions in making this study successful.

1. Dr. Cleophas Achisa Mecha (supervisor) and Prof. Er. Anil Kumar (co-supervisor) for their strong mentorship, positive criticism and unwavering support that made this work be of quality and timely finish.

2. Department of Chemical and process engineering under the leadership of the chair of the department (Dr. Milton Arimi) and postgraduate coordinator (Dr. Cleophas Achisa Mecha) for enabling timely finish through assessment and monitoring of progress regularly and organizing informative workshops, access of lab equipment and labs, especially during the holidays. May you be blessed abundantly.

3. The National Research Fund (PI Dr. Milton Arimi,) for funding this research [Grant number 2/MMC/825].

4. The Renewable Energy, Nanomaterials, and Water Research Group (RENWA), Department of Chemical and Process Engineering and research group members (patron Dr. Cleophas Achisa Mecha) for mentorship, acquisition of valuable research skills, encouragement and inspiration.

5. My parents (Stephen Kiprop and Peninah Jemutai), my wife (Prudence), and my siblings (Mercy, Miller, and Brian) for their encouragement and enormous support they offered. May you be blessed.

ABSTRACT

The increasing microbial and persistent emerging organic contaminants presence pose detrimental effects on the environment and ecosystem, such as diseases and toxicity. Conventional water treatment methods are ineffective, necessitating advanced techniques such as photocatalysis and membrane processes. This study aimed to synthesize and apply solar photocatalytic membranes for disinfection and degradation of organic pollutants in wastewater. The specific objectives were to: synthesize and characterize nitrogen-doped titanium dioxide nanoparticles and membrane; determine optimum conditions for degradation and disinfection of pollutants in wastewater using solar photocatalysis and filtration; and assess the performance of the photocatalytic membranes, durability, and reuse. Nitrogen-doped nanoparticles(N-TiO_2) were synthesized and immobilized onto the polyvinylidene fluoride (PVDF) membrane. Characterization was by Fourier transform infrared spectra, X-ray diffraction, water contact angle, Scanning Electron Microscopy-Energy Dispersive X-ray (SEM-EDX). The combined effects of pH and sodium chloride (NaCl) concentration were modelled and optimized for two experimental sets with N-TiO_2-PVDF. Sulphamethoxazole degradation, flux and TOC removal were responses for 1st and *E.coli* removal and flux for 2nd sets. N-TiO_2-PVDF performance was assessed at pH 4-10, 6-14 mg/l sulphamethoxazole and $2.6x10^8$-$10.4x10^8$ CFU/l *E.coli*. N-TiO_2-PVDF reuse and durability was assessed with 5 repeated cycles of 6mg/l sulphamethoxazole and $10.4x10^8$ CFU/l *E.coli* removal. Nitrogen doping red-shifted the light absorption to a visible range of 440nm. Nitrogen dopant was detected at 1170 cm^{-1} for N-TiO_2 and 1346-1417 cm^{-1} for nitrogen-doped titanium dioxide PVDF(N-TiO_2-PVDF) membrane. SEM-EDX identified 0.01wt% nitrogen in N-TiO_2-PVDF. The water contact angle reduced by 81.39^o because of polyvinyl alcohol and N-TiO_2. The analysis of variance had high predictability with R^2 of 0.73, 0.93 and 0.75 for 1st set, and 0.83 for 2nd set, with coefficients of variance under 10%, indicating adequate response variation. The optimum conditions for 1st set were pH 4.6 and 7.8 g/l NaCl for 76.5% degradation, pH 4.6 and 7.8 g/l NaCl for 9.8 ml/7cmD/min flux and, pH 7.3 and 11.7 g/l NaCl for 58% TOC removal. The optimum condition for 2nd set was pH 4.6 and 7.8 g/l NaCl for 5.3 ml/7cmD/min flux. However, *E.coli* removal could not be modelled due to total *E.coli* elimination by size exclusion. Sulphamethoxazole's highest degradation and relative flux were 81.31% and 0.77 at pH 4, caused by the surface charges enhancement and N-TiO_2 antifouling. 65.0% highest TOC removal was at pH 7 and attributed to degradation intermediates properties. 6mg/L sulphamethoxazole had the highest degradation of 69.87%, 0.73 relative flux and 69.87% TOC removal, and depended on the N-TiO_2 inactivation and foulants. *E.coli* highest disinfection was 99.04%(2.017 log reduction) at pH 7 and at 0.3017 relative flux, and attributed to weak repulsive surface charges and N-TiO_2 antifouling. $2.6x10^8$ CFU/l *E.coli* had 96.15%(1.415 log reduction) highest disinfection and relative flux of 0.42 and attributed to light hindrance and bio-fouling. N-TiO_2-PVDF had a decline of 10.13% degradation, 0.29 relative flux and 13.59% TOC removal, and of 1.92% disinfection and 0.07 relative flux with reuse cycles. In conclusion, N-TiO_2-PVDF effectively eliminated pollutants and with high durability and reuse. More antifouling, decontamination and reuse clean-up strategies on N-TiO_2-PVDF are recommended.

TABLE OF CONTENTS

LIST OF TABLES

LIST OF FIGURES

ACRONYMS AND ABBREVIATIONS

ANOVA	Analysis of Variance
CCD	Central Composite Design
CFU/l	Colony Forming Units per liter
$CTM^{\cdot}$	Contaminant radical
EDX	Energy-Dispersive X-Ray spectroscopy
FTIR	Fourier Transform Infrared Spectroscopy
FWHM	Full Width at Half Maximum
HCTM	Hydrogen containing contaminant
N-TiO_2	Nitrogen doped titanium dioxide
N-TiO_2-PVDF	Nitrogen-doped titanium dioxide Polyvinylidene fluoride
$OH^{\cdot}$	Hydroxyl radical
PL	Photoluminesce Spectra
PVDF	Polyvinylidene fluoride
RSM	Response Surface Methodology
SEM	Scanning Electron Microscopy
SMX	Sulphamethoxazole
TiO_2	Titanium dioxide
TOC	Total Organic Carbon
eV	Electron volts

CHAPTER ONE: INTRODUCTION

1.1 Background

The ever-growing urbanization, industrialization, population, and agricultural activities in the world have led to high demand for clean and reliable water. The world economic forum 2021 estimates that there will be a 40% gap between demand and supply by 2030 and that water shortages could displace 700 million people if no action is taken (Bell, 2021). Kenya has been identified as a water-scarce country having 41% of the population lacking access to clean water, with 9.9 million people drinking water from contaminated sources (Orina, 2021). With the high demand in the country, vast volumes of wastewater are generated. They are loaded with emerging pollutants such as pharmaceuticals (K'oreje, Vergeynst, Ombaka, Wispelaere, & c, 2016), agrochemicals (Ndunda, Madadi, & Wandiga, 2018), plastics, and dyes that cannot be handled effectively by secondary biological treatment.

The sources of pollutants are industries, pharmaceutical, and personal care products that release pollutants such as phenol, sulfamethoxazole, diphenhydramine, trimethoprim, amoxicillin, bisphenol A, rhodamine, ibuprofen, humic acid, and dyes (Jingli, et al., 2018) , (Ngumba, Gachanja, & Tuhkanena, 2015), (Kenneth, et al., 2018) are highly stable, persistent, and stubborn to biological degradation in nature. They are discharged as well as with microbes such as *Escherichia coli*, *Klebsiella aerogenes, Enterococcus faecalis, Salmonella typhi, Salmonella paratyphi, Pseudomonas aeruginosa, Vibrio cholerae, Vibrio parahaemolyticus, Proteus mirabilis* and *Shigella flexneri* (Musyoki, Suleiman, Mbithi, & Maingi, 2013). Of late, antibiotics (such as sulphamethoxazole, diphenhydramine, trimethoprim, amoxicillin, and others) have been spotted in high concentrations upstream and downstream of wastewater biological treatment plants in the country, particularly Machakos, Nyeri, and Meru (Kairigo, Ngumbac, Sundberg,

Gachanja, & Tuhkanena, 2020). These antibiotics have a vast potential of creating microbial resistance to drugs if allowed to accumulate in surface and ground waters. A concentration lower than minimum inhibitory concentration highly promotes microbial resistance (Kowalska, et al., 2019). Therefore, it is necessary that water having these microbes and pollutant drugs be treated using tertiary methods. This will facilitate safe water reuse (Shon, Phuntsho, & Vigneswaran, 2007) and discharge to water bodies without causing related harm. This will also relieve the natural water resources from the pressure of demand for clean water.

Among the tertiary methods are chlorination, UV/H_2O_2 photo-fenton oxidation and Ozonation, membrane separation, and photocatalytic oxidation. Chlorination suffers weaknesses such as incompatibility of combination with methods like membrane technology, pH specificity of 3.5-6.5, vulnerability to microbes, loss of performance by conversion of poly acetyls to hydroxyls, and generation of unwanted chemicals like chlorophenols (Al-Abri, et al., 2019). UV/H_2O_2 photo-fenton oxidation is a method that suffers from setbacks of specificity to compounds to be degraded in terms of dosage and condition as well formation of vast amounts of ferrous sludge (Hansson, Kaczala, Marques, & Hogland, 2012). Ozonation is a method that suffers setbacks such as oxidant dependent performance, corrosively, high power consumption, short half-life, and formation of other chemicals (Crini & Lichtfouse, 2019).

Membrane filtration (in polymeric or ceramic forms) is applied in the filtration process that produces clean water devoid of pathogens and pollutants due to its selectivity created by pore size. Microfiltration membranes have a pore size of 0.1-10 µm and operate at a pressure of 0-3 bars. This membrane is ideal for removing solids, organic colloids, and bacteria. Ultrafiltration membranes have a pore size of 0.005-0.1 µm and

operate at a pressure of 0.5-10 bars. This membrane is ideal for removing pathogens, viruses, and colloids. Classification of polymeric membranes by material can be of polyvinylidene fluoride (PVDF), polyacrylonitrile (PAN), polytetra fluoroethylene (PTFE), and others. The type of material used to make the membranes imparts different qualities that can be chosen; superior among all is PVDF as it has high thermal stability, good chemical resistance, and excellent mechanical property. Despite the advantages, membranes fail to eliminate pollutants and microbes fully. It separates the pollutants and microbes by size exclusion creating another phase containing more concentrated pollutants and microbes. Also, after several rounds of membrane application, the membrane suffers low permeate flux due to fouling, whereby contaminants accumulate to the surface and pores of the membrane. The contaminants that cause fouling are organic colloids, organic macromolecules, inorganic suspended solids, soluble organics, and microorganisms. (Nascimbén, Zsuzsanna, Cecilia, Gangasalam, & Gábor, 2020). Chief among the types of fouling is biofouling caused by microorganisms, microorganism DNA, and their enzymatic reactions (Shon, Phuntsho, & Vigneswaran, 2007).

Photocatalysis incorporates a semiconductor as photocatalysts and begins with the falling of light energy photons that should be enough to cause electrons(e-) to get excited and move from valence band to conduction band, leaving a hole(h+) that is positively charged (Nascimbén, Zsuzsanna, Cecilia, Gangasalam, & Gábor, 2020). The electron and hole can attack pollutants and denature them directly. Also, the electron and hole will oxidize water and hydroxyl groups and reduce dissolved oxygen-producing highly reactive radicals like hydroxyl (HO·), superoxide (O·2-), and perhydroxyl(HOO·), which will attack organics and mineralize them to carbon dioxide, water and low molecular organics hence detoxify water.

Hydroxyl radicals (HO·), owing to their size, will also attack microbes by passing through the outer cell wall and attacking lipids and proteins in the cell membrane incapacitating the microbes. Hydroxyl radicals can attack deoxyribonucleic acid (DNA) and ribonucleic acid (RNA) therefore having an added advantage of rendering viruses harmless (OBE, Davenport, Mole, & Wyatt, 2020). This disinfects water.

The semiconductors that can be used are Titanium dioxide (TiO_2), Copper oxide (CuO_2), Zinc oxide (ZnO), Silver phosphate (Ag_3PO_4) (Jingli, et al., 2018). Among the semiconductors, TiO_2 stands attractive due to numerous advantages of having the ability to decompose pollutants and microbes, ambient operating conditions, environmental friendliness, availability, ease of modification, and the issue of cost (Wang, Liu, & Qu, 2013), (M.S., W.I., H., M.A.M., & K., 2017), (Wanichaya & Wisanu, 2011). Despite the mentioned advantages, TiO_2 is only photo-activated at a light wavelength of λ=365nm (Hatat-Fraile, et al., 2017) and therefore will only utilize up to 5% of sunlight or visible spectrum. This weakness is due to the nature of TiO_2 having a bandgap of 3.2ev (Wang, Liu, & Qu, 2013).

Recombining holes and electrons is also a concern with the use of TiO_2 and leads to the discharge of energy through heat. This reduces the number of holes and electrons and reduces the number of reactive radicals produced. A reduced number of radicals reduces the ability of the conductor to detoxify and disinfect wastewater.

A good quality semiconductor should have slow recombination of electrons and holes to allow easy formation of radicals and have a shorter bandgap to reduce the amount of energy to photoexcite it. This will imply that it will be able to use visible solar light of wavelength (λ=320nm-400nm) (Huiru, et al., 2020). To reduce the bandgap, doping is introduced. Doping introduces different energy levels between the conduction band and

valence band (Wu, et al., 2023). Doping can be done by use of noble metals (like silver, gold, and platinum), transition metals (like aluminum, copper, and molybdenum), or non-metals (like nitrogen, Sulphur, fluorine, and carbon). Metal dopants present cost challenges in the application and a risk to secondary pollution caused by leaching (João, João, Eva, M., & C., 2019). Among the non-metals, nitrogen is the most preferred due to its smallest bandgap (Pangestuti & Gunlazuardi, 2018), its abundance, low toxicity, environmental friendliness, and it is bound in low-cost compounds. Nitrogen reduces the bandgap from 3.18eV to 2.20eV by getting into the matrix arrangement of TiO_2 and creating interbands that are low lying (Loeb, et al., 2021), (Wanichaya & Wisanu, 2011).

Apart from the mentioned advantage of doping, it makes the resulting semiconductor more porous, increasing the surface area besides making it more economical by using solar as an energy source and avoiding the use of electric lamps that are energy-consuming.

Several doping methods have been done, including solvothermal, hydrothermal, calcination and electrochemical oxidation, and the sol-gel method. The method of doping will majorly depend on the availability of resources and equipment.

1.2 Statement of the Problem

Faced with water shortage or water scarcity, there is a need to use wastewater as another water source. This will only be possible if its safety is guaranteed. For the minimum accepted level to be met, wastewater should further be treated by some effective tertiary means after standard conventional methods like biological methods.

Modern-day wastewater is heavily loaded with both organic and microbial contaminants that have led to pollution of water sources. Most of the organic pollutants

are persistent and are stubborn to biological degradation. Microbial contaminants have also been a source of water-related illnesses among populations downstream. To prevent this, tertiary means will be of the essence. Among the tertiary methods are chlorination, ozone treatment, UV/H_2O_2 fenton, membrane separation, and photocatalysis. All the methods are faced with numerous challenges such as ineffectiveness, creation of toxic byproducts, phototoxicity, and high cost of implementation (Zagklis & Bampos, 2022).

The sole use of photocatalyst semiconductors in cleaning water poses a significant challenge in recovery by separation and poses a pollution risk. Apart from the desired catalyst reuse for economic purposes, sole use discourages this.

The sole use of membrane-based separation merely separates the pollutants and does not eliminate the pollutants. It instead creates a second phase with a high concentration of pollutants. Hindering its long-term use is a significant problem of fouling and biofouling.

Developing a photocatalytic membrane as a hybrid of photocatalysis and membrane-based separation will enhance the advantages of both technologies. The low molecular organics not fully broken down will be among the retentate of the microfiltration membrane, allowing more time for the catalyst to break down more organics. Also, the membrane will solve the hectic problem of separation of catalyst from the treated wastewater by creating a barrier where catalysts will be retained without using expensive separation methods.

1.3 Aim and Objectives

1.3.1 Aim

Synthesize and apply solar photocatalytic membranes for disinfection and degradation of organic pollutants in wastewater.

1.3.2 Specific objectives

i. To synthesize and characterize nitrogen-doped TiO_2 nanoparticles and membrane.
ii. To determine optimum conditions for degradation and disinfection of pollutants in wastewater using solar photocatalysis and filtration.
iii. To assess the performance of the photocatalytic membranes, durability, and reuse.

1.3.3 Research questions

i. What are the morphological and chemical composition changes with synthesizing nitrogen-doped titanium nanoparticles and membranes?
ii. What are the optimum conditions for the degradation and disinfection of pollutants in wastewater using solar photocatalysis and filtration?
iii. What is the performance of the photocatalytic membranes, durability and reuse?

1.4 Justification of the Study

Urbanization, industrial and population growth have led to high demand for water free of contaminants (He, et al., 2021). Progress in health care and agricultural livestock rearing has led to an increase in over-reliance on antibiotics in curing and preventing illnesses (Polianciuc, Gurzău, Kiss, Ştefan, & Loghin, 2020). Poor metabolic utilization of antibiotics and poor disposal of drugs result in the discharge of wastewater containing antibiotics into conventional wastewater treatment facilities. These conventional facilities cannot fully eliminate emerging antibiotic pollutants due to their stability and resistance to degradation and persistence. This

has led to their detection in surface and groundwater (Fu, et al., 2022). The presence and exposure of low concentrations in the environment that is less than therapeutic effectiveness amount to microbes have led to the development of drug-resisting genes (Bai, et al., 2022). This causes long patient therapeutic time, less effectiveness of drugs in treating illnesses and high mortality (Dadgostar, 2019). With the current water demand and pollution of the environment, water-related illnesses and epidemics have also increased lately (Park, et al., 2018). This is caused by microbial contaminants present in natural water resources caused by wastewater contamination. A tertiary means of treating the biological wastewater treatment discharge is of necessity so as to address the problem of water scarcity, emerging stubborn pharmaceutical pollutants and pathogens so that the enormous volumes may be reused as a resource but in a safe and clean condition such that to create public confidence (Gerba & Pepper, 2019).

1.5 Scope of the study

The study focused on 2 contaminants, namely sulphamethoxazole(a sulphonamide antibiotic) and E.coli (a gram-negative bacteria) spiked synthetic wastewater to study degradation, disinfection, flux and TOC removal with multivariate factor design, performance, reuse and durability. The photocatalytic membrane had a pore rating of ultrafiltration. The experiments were performed with a solar intensity range of $950W/m^2$-$1050W/m^2$.

1.6 Significance of the study

The Kenyas' 3rd schedule for standard for effluent discharge into the environment under environmental management and coordination (water quality) regulation, 2006-legislature supplement no 36, requires the maximum allowable limit of 0.05mg/l COD and nil/100ml of *E.coli*. This research aimed to attain this by synthesizing and applying visible-light-driven photocatalytic membranes to eliminate organic pharmaceutical compounds and microbial contaminants in simulated wastewater by assessing its optimal conditions for multivariate factors, performance, reuse, and durability. The results from this research can be used in the

scale-up of the system to provide recyclable water for general purposes such as cleaning and irrigation.

CHAPTER TWO: LITERATURE REVIEW

The literature review section covers the current water situation, types of waste water, types of waste water pollutants, contaminants of focus, technologies applied to treat waste water with related challenges and motivation for application of photocatalytic membrane.

2.1 Water Situation on the Globe, Africa, and Kenya

According to the United States geological survey, 71% of the earth's total surface is water-covered. Of the total amount of water, 96.5% exist in oceans, and 0.9% appear in other salty sources within the land. This leaves only 2.5% of all the water be freshwater. The total freshwater is distributed in glaziers and ice caps 68.7%, groundwater 30.1%, and surface water 1.2%. surface water is further distributed as follows: ground ice and frost 69%, lakes 20.9%, soil moisture 3.8%, swamp and marshes 2.6%, rivers 0.49%biological living bodies 0.26% and atmosphere 3.0%. (Survey, 2019) .

With ever-growing urbanization, industrialization, population, and agricultural activities, the little accessible freshwater becomes less and less, leading to water shortages. Over 2.8 billion will face water scarcity or stress in 48 nations by 2025 (GRID-Arendal, 2021). Water stress is when a population in a geographical location receives less than $1700m^3$ per year per person. In contrast, water scarcity is when a population in a geographical location receives less than $1000m^3$ per year per person.

According to World Bank, more than 25 nations in Africa will face water stress by 2025. This is a sharp increase compared with 13 nations in 1995 facing water stress. By 2025 in the 25 nations, 16% of the population will face water scarcity, and 32% will face water stress. It is also anticipated that the agricultural sector will lead the

consumption of water at 85%, 9% for human use, and 6% for industrial sector use (bank, 2017).

Kenya has been identified as a water-scarce country having 41% of the population lacking access to clean water, with 9.9 million people drinking water from contaminated sources (Orina, 2021). The contamination results from wastewater discharge loaded with pollutants onto surface waters due to ineffective treatment by secondary biological means within the municipalities.

2.2 Types of Wastewater

Wastewater can be classified as per the origin (Ambulkar, 2021): (1) Domestic wastewater is water that originates from the use of water at residential places. The wastewater carries pollutants and originates from urine, feces, sweat, laundry, disinfectants, and personal care products, (2) Industrial wastewater originates from the industrial use of water in industry and economic activities like cleaning spillages. It carries various types of pollutants depending on the industry materials used, and (3) Storm wastewater that originates from rain and accumulates on the ground surface resulting in run-offs and finding ways to water bodies and sewer lines. It carries pollutants from the ground surface that is mainly dependent on social-economic factors.

2.3 Types of Wastewater Pollutants

Pollutants can be classified as Solid particles pollutants, nutrients pollutants, organic pollutants and microbial pollutants. Solid particles pollutants are solids that are suspended in the wastewater. They are easily removed through a combination of coagulation and settling ponds or centrifugation means. Nutrients pollutants are the dissolved salts of nitrogen and phosphorus that plants require for development. In high levels, it causes eutrophication (Warmadewanthi & Bachtiar, 2019). They can be

removed through biological techniques, ion exchange techniques, or crystallization techniques. Organic pollutants are pollutants that emerge from a household, industrial chemicals, pharmaceuticals, pesticides, and personal care products. They are dissolved in wastewater and depending on their stability; they can be classified as readily degradable, relatively degradable, or stubborn to degradation as per biological means of degradation. The amount of dissolved oxygen is a clear indication of how the water is polluted. Highly polluted wastewater has less dissolved oxygen. Examples of these pollutants are: dyes, humic chemicals, phenolic compounds, pesticides compounds, pharmaceutical compounds. Microbial pollutants are caused by microorganisms in wastewater discharge and comprise fungi, bacteria, and protozoa groups. They cause toxification of water apart from being disease-causing. Examples are: *Escherichia coli* (*E.coli*), *Campylobacter jejuni*, *Hepatitis A virus (HAV), Giardia lambia, Salmonella bacteria*, *Cryptosporidium*.

2.4 Contaminants of Focus

2.4.1 Sulphamethoxazole

Sulphamethoxazole ($C_{10}H_{11}N_3O_3S$) is an antibiotic belonging to the sulphonamide group that acts on bacteria by inhibiting the folic acid synthesis in a bacterial cell. It is used to treat various body infections. It has a molecular weight of 253.28, a solubility of 610mg/ liter of water, and an acidity proton value(pKa1) of 1.7 (Kutuzova, Dontsova, & Kwapinski, 2021). It has been detected in high levels in the country both at wastewater effluents and water sources (Otieno, et al., 2018). It has adverse effects even in extremely low concentrations. The sources of sulphamethoxazole pollutants are; (1) Pharmaceutical industries that produce sulphamethoxazole as a drug, (2) Improper disposal of expired drugs into the sewer lines, (3) Poor drug intake of 70% to 10% by

humans and animals leading excretion of the drug (Zhou, Yun, Wang, Li, & Wang, 2022). The chemical structure is shown in Figure 2.1.

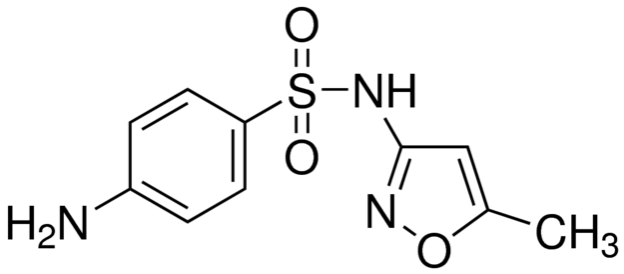

Figure 2.1: Chemical structure of sulphamethoxazole (MedChemExpress, 2023)

Sulphamethoxazole resists biodegradation because it is antibiotic and toxic to degrading bacteria and algae in the wastewater (Xu, Xie, & Li, 2022). Its presence in the aquatic ecosystem causes bacteria to experience selective and long-duration exposure to low concentrations of sulphamethoxazole and, in turn, develops adaptive genes to develop resistance to sulphamethoxazole. This limits the treatment options of bacterial infections for patients and the high cost of treating a bacterial infection in the future through research for a new formulation of drugs. Currently, it is estimated that 700000 deaths are caused by microbial tolerance to antibiotics (Kutuzova, Dontsova, & Kwapinski, 2021).

2.4.2 *E.coli*

E.coli is a facultative anaerobic bacterium primarily rod-shaped with 2-6 µm length and width of 1.1-1.5 µm. Flagella enhances its movement. Its cell wall is capsulated by acidic polysaccharides. The structure of *E.coli* is shown in Figure 2.2.

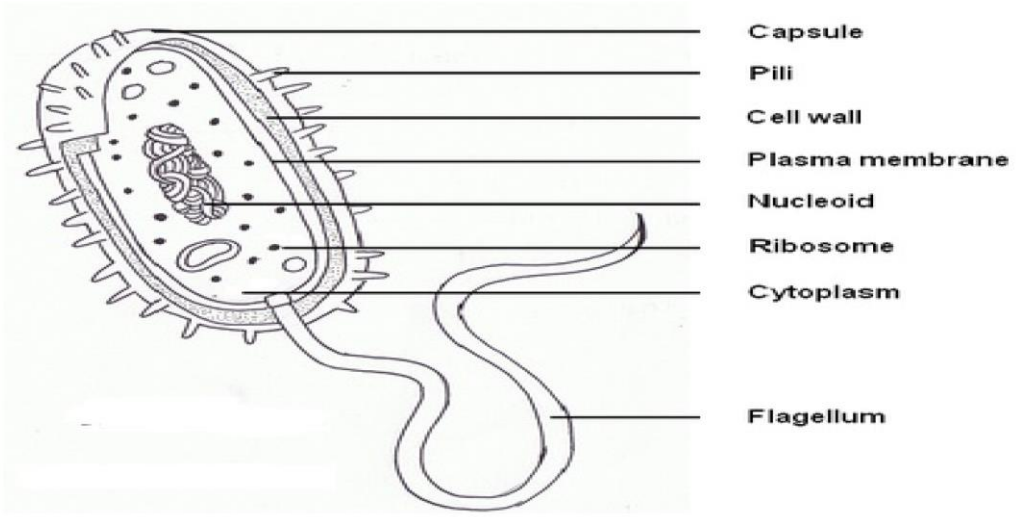

Figure 2.2: Structure of *E.coli* (Ajiboye, Babalola, & Onwudiwe, 2021)

E.coli originates from the lower digestive system of animals and human beings. Its detection is a sure way to indicate water contamination with fecal matter. *E.coli* bacteria have different strains: Enteropathogenic *E.coli*, Enterotoxigenic *E.coli*, Vercytotoxigenic *E.coli*, Enteroaggregative *E.coli* and Diffuse adherent *E.coli*. These strains cause different illnesses ranging from diarrhea, vomiting, fevers, and dysentery-like symptoms by attaching to the intestines.

2.5 Technologies for Wastewater Treatment

Faced with the emerging organic pollutants, municipal wastewater treatment methods proves to be inefficient in eliminating them due to their chemical stability and are therefore stubborn to biological methods of degradation. Biological methods of degradation use myco-bacteria, rhodococcus, norcardia and corynobacteria to cause decomposition through processes such as acetogenesis, hydrolysis, methogenesis and fermentation in aerobic and anaerobic conditions (Zhang, Xu, & Zhu, 2018). The bioreactions naturally are slow. Additionally; biological methods were not designed to handle the stable emerging pollutants that take long for degradation. Also, biological methods currently used fail to eliminate biological contaminants making downstream

users open to challenges of contracting waterborne diseases. Therefore, additional methods must remove contaminants before discharge or reuse. This will reduce the cost of portable water treatment and attract reuse as an additional source of water as its safety conditions will be met. Having an additional water source from wastewater will relieve other water sources of the pressure of demand, therefore, reducing water scarcity and stress. Among the additional treatment methods are:

2.5.1 Chlorination method

This is a majorly applied method to deal with microbial contaminants and less organic contaminants. Hypochlorous acid (HOCl) and sodium hypochlorite are added as decontaminants in concentrations of about 1mg per liter of water. They hydrolyze in water to give hypochlorite ions as reactive chlorine ions (OCl^-) as shown in equations 2.1 and 2.2.

$HOCL \leftrightarrow H^+ + OCl^-$ Equation 2.1

$NaOCl \leftrightarrow Na^+ + OCl^-$ Equation 2.2

Hypochlorite ions have an oxidation potential of 1.4eV. Hypochlorite may also react with ammonia in water to give ammonium chloride (NH_4Cl) another decontaminant. Chlorine reacts with the cell membrane making it porous. The cell contents, including cell proteins, DNA, and RNA, will leave, leading to the ultimate death of microbes (Ghernaout, 2017). Of the three decontaminants, HOCl is the most effective.

Chlorination is a low-cost method with effortless scalability and effectiveness in reducing most bacterial and viral contaminants. The method suffers from serious setbacks such as (1) Low or minimal protection against some forms of disease-causing protozoa. (2) Poor decontamination capability in highly turbid waters. (3) Creation of

bad taste and odor in decontaminated water. (4) Sensitivity to pH and only optimal at a pH range of 3.5 to 6.5. (5) Formation of more toxic products such as trihalomethane, haloacetic acid, haloceanitrile, and chlorophenols as side reactions between chlorine and organic pollutants. This additionally leads to loss of hypochlorite ions and hence loss of performance.

2.5.2 Ozone treatment method

Ozone treatment is one of the methods in the advanced oxidation process. Ozone (O_3) is a gas that can directly oxidize microbes and organics with an oxidation potential of 2.07eV and is also applied to water to create hydroperoxy radicals and hydroxyl radicals that readily attack and oxidize microbes' cell walls and organic contaminants effectively.

Ozonation can remove taste and smell, metals, and other anionic compounds. Although ozonation operates in a wide range of pH and temperatures, it suffers from setbacks such as (1) Partial and low solubility in water of 0.4kg/m^3 of water at 30^0C, which will require complex mixing means and will be power intensive. (2) Side reactions with organics lead to the generation of aldehydes and ketones that are toxic. (3) High cost of large-scale installation and treatment. (4) Irritation and toxication risk to personnel handling ozone water treatment and (5) High reactivity and corrosivity will require unique material for equipment that will offer resistance, for example, stainless steel.

2.5.3 UV/H_2O_2/Fenton process

This homogenous advanced oxidation process uses hydrogen peroxide and iron (II) sulfate to generate hydroxyl radicals. Hydroxyl radical and hydroxyl ion is generated through the oxidation of iron II ions to iron III ions in similar molar concentration. Hydrogen peroxide will cause the reduction reaction of iron III to iron II generating

hydroxyperoxy radical and protons. Application of ultra-violent light with energy photons more than the bandgap will cause iron II ions to revert to iron III ions in reacting with water molecules but with the generation of hydroxyl radical and a proton.

The generated radicals will attack organics and mineralize them to low-level organics, carbon dioxide, and water. Microbes will also be attacked at the cell wall and its internal organelles by the radicals, causing cell death.

This method is homogenous and provides high reactions due to interactions between radicals, pollutants, and microbes. Despite the merits, this method suffers from setbacks such as (1) Requirements of running under low pH to prevent or reduce precipitation of iron III ions. (2) High consumption of fenton reagents rendering it uneconomical. (3) Requirement of an additional separation process of iron ions from water. (4) Production of massive ferrous sludge poses a risk of environmental pollution.

2.5.4 Membrane-based separation

A membrane is a physical barrier. It selectively allows substances to pass through it while preventing some from passing through by influencing transportation differences like concentration difference or pressure. When applied in wastewater, it allows water-free contaminants to pass through to the permeate side while preventing contaminants from passing through and retaining them as retentate. The efficiency of a membrane depends on the material used for fabrication, pore size, and mechanical properties (Huiru, et al., 2020).

The membrane can either be operated as a dead-ended or cross-flow operation in the wastewater separation process. For dead-ended operations, all the wastewater is forced through a membrane utilizing a pump in which contaminants free water will pass through, and retentate will be contaminant concentrated water. This operation is

exposed to conditions like gelling of organic pollutants or caking of colloids at the boundary surface of the membrane, causing clogging. This will need more pressure increase to maintain permeate flux through the membrane. Filtration will proceed until the total or partial blockage is observed. This operation only favors batch operations. In a cross-flow operation, the feed wastewater is pumped along the membrane, and water-free contaminants will be collected as it flows down the membrane position. The retentate or pollutant concentrated water is eliminated from the membrane or recycled back to the feed wastewater. This operation outperforms the dead-ended operation in that there will be less deposition on the membrane surface due to the transport mechanism of the flow of wastewater. It is, therefore, suitable for continuous operation.

The membrane can either be made of ceramic materials or polymeric materials. Ceramic membranes are not popular due to their high manufacturing cost and difficulty scaling up to industrial size applications.

Polymeric membranes can be made of the following polymers: polyvinylidene fluoride(PVDF), Polyvinyl alcohol(PVA), Polyacrylonitrile(PAN), Polysulphone(PS), Polyamide(PA), Cellulose acetate(CA) with the following chemical composition $(CH_2CF_2)_n$, $(C_2H_6O_2)_n$, $(C_3H_3N)_n$, $(C_{27}H_{26}O_6S)_n$, $(CONH_2)_n$, $(C_6H_7(OH)_3)_n$ respectively (Chen, Hu, Xie, & Wang, 2018).

Polymeric membrane is fabricated and operated as per different modes. Microfiltration (MF) is used to separate colloidal particles, bacterial and protozoan cell forms owing to a pore size of 0.1µm - 10µm separation while operating at a pressure range of 0.1 bar-2 bar. Ultrafiltration (UF) separates colloidal particles, protein molecules, sugar molecules, protein molecules, viruses, bacterial and protozoan cell forms owing to a pore size of 0.001 µm – 0.1 µm while operating at a pressure range of 1 bar-10 bar.

Nanofiltration (NF) is used to separate viruses, organic molecules, and ionic salts owing to a pore size of 0.0001 µm – 0.001 µm while operating at a pressure range of 5 bar-20 bar. Reverse osmosis (RO) is used to separate virtually all contaminants owing to a pore size of Less than 0.0001 µm while operating at a pressure range of 10 bars-100 bars.

The membrane separation process uses no chemicals, gives quality permeate water, consumes less energy, is easy for operations, and can easily be scaled up to large operation (Argurio, Fontananova, Molinari, & Drioli, 2018).

Polymeric membranes are made up of hydrocarbons and are therefore hydrophobic. Organic pollutants, proteins, and sugar will attach to the membrane surface and pores through electrostatic attractions lowering permeability (Huiru, et al., 2020). This causes problems in that attachment is nearly permanent and leads to organic fouling and biofouling. A point is reached where the membrane is fouled; operations stopped regularly and will require methods like flushing, backwashing, air scouring, and chemical cleaning as a remedy to fouling and biofouling. The cleaning techniques also lower the number of times a membrane can be reused and increase operating costs.

2.5.5 Photocatalysis

Photocatalysis incorporates semiconductors as photocatalysts. Examples of semiconductors are TiO_2 (anatese), TiO_2 (rutile), Fe_2O_3, ZnO, ZnS, Cuo, Cu_2O, CdS, WO_3, NiO. The process begins with the falling of light of a particular wavelength and has energy photons that should be enough to cause electrons (e^-) to get excited and move from valence band (VB*) to conduction band (CB*) leaving a hole (h^+) that is positively charged (Nascimbén, Zsuzsanna, Cecilia, Gangasalam, & Gábor, 2020). The holes and electrons lead to the formation of radicals that disinfect and cause organic degradation. Radicals are molecules that have one or more unpaired electrons. The

Photocatalysis process is heterogenous, having three phases: wastewater, solid photocatalyst, and photons (Lin, Jiang, Chen, Xu, & Wang, 2020). Each photocatalyst has different locations of CB* and VB* and hence the bandgap energy (Eg*). Below are the examples (Tamirat, Rick, Dubale, Su, & Hwang, 2016) in Table 2.1.

Table 2.1: Examples of semiconductors with conduction band, valence band and band gap

Photocatalyst	**CB*in eV**	**VB*in eV**	**Band gap (Eg*) in eV**
TiO_2(anatase)	-0.1	3.1	3.2
TiO_2(rutile)	-0.05-0.15	2.92-2.95	3.0-3.7
Fe_2O_3	0.3-0.6	2.4-2.7	2-2.2
ZnO	-0.25	2.95	2.95
ZnS	-0.91	2.44	3.35
CuO	-0.51	1.04	1.55

The light wavelength (λ) enough for each semiconductor can easily be calculated as follows:

$Eg^* = hV$ Equation 2.3

Where h is planks constant and V is the wave frequency given as

$V = c\lambda$ Equation 2.4

Where

c is the speed of light. Replacing Equation 2.4 in 2.3. Then,

$Eg^* = hc/\lambda$ Equation 2.5

A perfect semiconductor in water disinfection and degradation should show qualities such as (1) High photocatalytic activity, pollutant non-selectivity, and a high surface area. (2) Longer separation duration times of holes and electrons. (3) Resistance to pollutant catalyst poisoning is therefore durable. (4) High mechanical and chemical

stability. (5) Insolubility in water. (6) Readily available and at a low cost and (7) nontoxic. (Mozia, 2010)

Titanium dioxide (TiO_2) closely fits the description of a promising photocatalyst and is used chiefly among semiconductors. TiO_2 naturally exists in 3 allotropes: metastable anatase, stable rutile, and metastable brookite, with each having different characteristics. Anatase has a tetragonal structure with more distortion, rutile tetragonal structure with less distortion, while brookite has orthombic and monoclinic structure. Anatase has an allotrope unit volume of 34.02Å^3, 31.12Å^3 for rutile and 32.02Å^3 for brookite (Rahimi, Pax, & Gray, 2016). Rutile and anatase are the most common allotropes of titanium dioxide, with brookite rarely existing in its pure form. Among the three, anatase has been shown through various researches to have higher photocatalytic activity than the other two because of a quicker photoelectrons migration and extended time of separation of holes and electrons.

2.5.5.1 Photocatalysis mechanism in pollutant degradation and disinfection

Photocatalysis has its genesis from the falling of light photons energy on a TiO_2 photocatalyst that is at least high enough than the bandgap energy. This will trigger electron (e^-) in the valence band (VB*) to get excited and will then move across to the conduction band (CB*). The gap left on the valence band will be a positive charge absence called a hole (h^+) as shown in Equation 2.6.

$TiO_2 + photons \rightarrow h^+ + e^-$ Equation 2.6

The resulting hole in the valence band may react with a water molecule or a hydroxide water anion, each resulting in hydroxide radicals with hydrogen ions only in the first scenario as shown in Equations 2.7 and 2.8.

$h^+ + H_2O \rightarrow H^+ + \cdot OH$ Equation 2.7

$h^+ + OH^- \rightarrow \cdot OH$ Equation 2.8

The electron in the conduction band will get attached to dissolve oxygen resulting in the generation of superoxide radicals as shown in Equation 2.9.

$e^- + O_2 \rightarrow \cdot O_2^-$ Equation 2.9

The superoxide radical may again react with hydroxide radical, yielding a hydroperoxyl radical as shown in Equation 2.10.

$\cdot O_2^- + \cdot OH \rightarrow HO_2^{\cdot}$ Equation 2.10

The hydroperoxyl radical may then react with hydrogen protons and electrons from the conduction band, leading to the formation of hydroxyl ions and more hydroxyl radical as shown in Equation 2.11.

$HO_2^{\cdot} + H^+ \rightarrow OH^- + \cdot OH$ Equation 2.11

The hydroxyl radical (having an oxidative potential of 2.8eV) will attack the hydrogen-containing contaminant (Hctm) with the formation of contaminant radicals (ctm·) and water molecule and hence more degradation, which may finally end with water and carbon dioxide as shown in Equation 2.12.

$Hctm + \cdot OH \rightarrow ctm^{\cdot} + H_2O$ Equation 2.12

The contaminant radical will attack other contaminants leading to low-level organics eventually. The superoxide radicals may also react with hydrogen ions, leading to hydrogen peroxide, which has an oxidative potential of 1.77eV and ready attacks pollutants degrading them as shown in Equation 2.13.

$\cdot O_2^- + 2H^+ \rightarrow H_2O_2$ Equation 2.13

All radicals formed as well attack water contaminants of either microbic nature or an organic pollutant. Superoxide radical has a reductive potential of -2.4eV, and perhydroxy radical has an oxidative potential of 1.7eV. Both reactions will lead to low-level molecular organics or carbon dioxide and water. Besides the formation of radicals, holes in the valence band can carry direct oxidation on contaminants. Also, an electron in the conduction band can carry a direct reduction of contaminants. Radicals attack the cell peptidoglycan layer, DNA, RNA, and proteins for microbes, causing oxidative stress. Peroxidation of lipid membrane leads to weakening and eventual rapture and release of cytoplasm contents. Also peroxidation of sugar rings and polypeptides leads to the formation of aldehydes, ketones, and carboxylic acid. All this leads to oxidative stress and the eventual death of a microorganism (Regmi, Joshi, Ray, Gyawali, & Pandey, 2018). Absence or access delay of a water molecule or dissolved oxygen that readily combines with electron and hole leads to recombination, resulting in heat dissipation and less radical generation, hence photocatalyst inefficiencies as shown in Equation 2.14.

$h^+ + e^- \rightarrow heat\ dissipation$ Equation 2.12

2.5.5.2 TiO_2 photocatalysis setbacks and need for modification

Titanium dioxide faces various setbacks that hinder its full performance and perhaps even in real industrial applications. Anatase allotrope has a bandgap of 3.2eV corresponding to an excitation wavelength of 388nm. Rutile allotrope has a bandgap of 3.0eV corresponding to an excitation wavelength of 410nm. This presents a narrow photocatalytic UV activation region, which is less than 5% of sunlight irradiation (Molinari, Lavorato, & Argurio, 2021). Solar light irradiation is composed of 5% UV light, 45% visible light and 50% infrared light. This will call for measures that will modify both titanium allotropes to utilize solar irradiation's larger 45% visible light

spectrum. This will make modified TiO_2 more and easily photoresponsive. This will eliminate the use of lamps and high dependence on electricity to cause electrons and holes separation making photocatalysis greener and appealing.

Titanium dioxide has a high electron and hole recombination which lowers the number of reactive radicals generated for degradation and disinfection. Recombination of electrons and holes leads to the release of photon energy into heat energy. It has been observed that 90% of holes and electrons recombine in a fraction of a nanosecond from the time of separation (Ribao, Rivero, & Ortiz, 2017). This dramatically lowers the performance of TiO_2 photocatalysis. Therefore, it is necessary to find a means to make TiO_2 visible light-sensitive and reduce the high recombination of holes and electrons. Doping is a means to achieve this.

TiO_2 has a chemical characteristic of being hydrophilic, i.e., water-loving. The pollutants are made of hydrocarbons as their basis, making them hydrophobic. This causes challenges of hindering interactions between the catalyst and pollutants, which slows down the photocatalytic radicals' attack on pollutants. This will call for measures like increasing the surface area of TiO_2 by making them through a process that optimizes small nanoparticles. Additionally, measures to concentrate pollutants have to be effected. This will maximize the interaction between pollutants and TiO_2. One of the attractive measures includes using a polymeric membrane that only leaves a concentrated retentate to be acted upon by photocatalyst.

The use of TiO_2 photocatalyst in wastewater treatment may lead to the discharge of nanoparticles of TiO_2 into the environment causing secondary pollution. TiO_2 has been shown to cause fish embryos to malfunction and die because of phototoxicity (Bar-Ilan, et al., 2012). Presence of titanium dioxide nanoparticles in the environment combines

with UV light and creates oxidative stress-related problems to aquatic organisms (Du, et al., 2019). In humans, the presence of nanoparticles in inhalation has been shown to increase the risk of pulmonary and cardiovascular diseases (Reijnders, 2009). To minimize the environment from exposure of phototoxicity caused by TiO_2; it will be immobilized on surfaces like polymerics to restrict and stabilize it.

2.5.5.3 Doping of titanium dioxide

Doping of titanium dioxide involves the introduction of noble metal or anions into titanium dioxide crystals either substitutionally or interstitially, which will change its photocatalytic properties to absorb the longer visible light wavelengths (Nie, Zhuo, Maeng, & Sohlberg, 2009).

Metal doping utilizes materials such as noble metals, transition metals and rare earth metals. Noble metal dopants such as platinum, gold, silver, lead, nickel, and rhodium can be introduced into titanium dioxide to make it visible light active (Park, 2021). Fermi levels, which are lower than for semiconductors, play a crucial role in separating electrons. Electrons will therefore counterbalance till some form of equilibrium is achieved. With the clustering of metal dopants, a Schottky barricade is formed, making metal dopants sink or trap electrons. This dramatically enhances the recombination reduction and enhances more time for the separation of holes and electrons. This will give more time for the generation of radicals. This boosts the performance of a TiO_2 semiconductor (Dong, et al., 2015). Transition metal dopants are metals characterized by 3d and 4d structures of electrons. Examples are iron, chromium, copper, and niobium. Doping with TiO_2 reduces the bandgap energy, modifies band position, Fermi level, and the d structure of electrons of TiO_2. New intermediate energy levels lower than conduction band are formed from partially filled d orbits, thereby inducing red shifting in bandgap hence making TiO_2 be visible light-responsive and hence smaller

wavelengths of light to activate. Also, equilibrium concentrations between hole and electrons are altered, causing charge trapping and suppression of recombination. Rare earth metal dopants are metals characterized by the existence of 4f, 5d, and 6s structures of electrons. Examples are lanthanide, cerium, and gadolinium. They form complexes with lewis-typed organics by interacting with its functional groups with orbits, thereby improving photocatalysis. The doping of rare earth metals with TiO_2 will result in wavelengths conversion to the utilizable range, thereby increasing TiO_2 photocatalysis efficiency.

Metal doping is effective in making TiO_2 visible light-sensitive and decreases recombination rates but suffer from setbacks such as (1) Thermal instability shortens the lifespan of the TiO_2 photocatalyst (Huang, Yan, & Zhao, 2016), (2) Noble metals, transition, and rare-earth metals are expensive and therefore unattractive in scaling up operations. (3) Synthesis methods of implanting metal into titanium dioxide are expensive. (4) Metal ions can act as recombination points, thereby lowering the efficiency of photocatalysis. (5) Low metallic solid diffusion at low temperatures. This always results in uneven doping of TiO_2 photocatalyst. (6) Metal dopants under operations leach, decreasing enhanced photocatalysis and its repeated use (Akhter, Arshad, Saleem, & Hussain, 2022).

Anions such as carbon, phosphorus, Sulphur, and nitrogen can be introduced into titanium dioxide lattice interstitially and substitutionally. The anions create localized states and smaller bandgaps by red and blue shifting of the absorption edge in TiO_2. This will require less photon energy to be activated and hence a smaller wavelength of light to be responsive in visible light. Carbon and nitrogen doping has been shown to cause a redshifting of 50nm (Julián, Pilar, & Sixto, 2007). Anions suppress the formation of recombination centers, unlike metallic dopants. Among the anions, carbon

and phosphorus doping results in creating deep states between the valence band and conduction band of TiO_2 and will not narrow the bandgap according to (Nazanin, A., & MacA., 2016).

In comparison, anion doping outperforms metallic doping in photocatalytic activity. Anion doping has been shown to instill superior thermal stability compared to metallic doping. More so, the process used in doping of anions doesn't require specialized equipment and is cost-effective (Al-Mamuna, Kaderb, Islamb, & Khana, 2019). Most anionic dopants are found in widely available precursors. Among the anion dopants, nitrogen is the most promising and researched more (Asahi, Morikawa, Irie, & Ohwaki, 2014).

Nitrogen can be doped into TiO_2 and modifies it by either substitutional or interstitial mechanisms (Piątkowska, Janus, Szymański, & Mozia, 2021). The substitutional mechanism is responsible for changing surface characteristics, while the interstitial mechanism is responsible for changing the lattice of TiO_2. Among the non-metal dopants, nitrogen displays superior stability to phosphorus, sulphur, and carbon, making n-doped repeatedly used for degradation and disinfection purposes.

With nitrogen doping, P states hybridize with O_{2p} and result in band narrowing. Sulphur has been shown to have this same effect as a dopant but suffers a setback due to higher energy of formation of 4.1eV compared with 1.6eV for nitrogen. Carbon and phosphorus doping do not show a bandgap narrowing effect, according to (Nazanin, A., & MacA., 2016). Nitrogen has an atomic size radius of 1.71Å, whereas oxygen has an atomic radius of 1.40Å. These sizes are comparable and make nitrogen a better and more suitable substitutional replacement in TiO_2 lattice. Nitrogen with ionization energy of 1402.3kJ/mol is comparable with 1313.9kJ/mol for oxygen which alters the

electronic and surface characteristic of TiO_2, leading to better photocatalytic performance (Kaur, et al., 2020).

2.6 Motivation For use of Photocatalytic Membrane

Photocatalysis and membrane separation process in the sole use of water treatment is faced with challenges that may hinder the full exploitation of both methods. Combining the two in a single setup hybrid will be synergistic. There are two ways to hybridize the two technologies: (1) Photocatalyst suspended in slurry and membrane barricading the catalyst with fed wastewater. (2) Photocatalyst immobilized on or into a membrane.

In hybridization, the membrane confines the catalyst, wastewater feed, partially broken organics, and microbe in a single environment. This is advantageous because the hydrophilic contaminants, microbes, partially broken microbes, and organics will be concentrated, increasing photocatalyst interactions. This will increase photocatalytic efficiency and increase the quality of permeate.

In both hybridization ways, catalyst recovery is enhanced, and the loss of catalyst in the form of nanoparticles is prevented by the membrane, thereby allowing for repeated catalyst use.

The use of membrane photocatalysis leads to better control of the performance of photocatalytic reactions. Persistent organics and some microbes that take more time for complete degradation and disinfection are not permitted to pass through the membrane. This requires more residence time that the selectivity of the membrane will enhance.

By incorporating membrane and photocatalysis technologies, reactions are allowed to take place on the surface of the membrane. This arrests the hectic problem of membrane fouling caused by organic and bio-molecules. This increases the lifespan of a membrane.

Photocatalyst suspended in slurry and barricaded by membrane type of hybridization has been shown to have higher photocatalytic action than photocatalyst immobilized on or into the membrane (Raffaele, Cristina, & Pietro, 2021). Nevertheless, a loss of consistent performance is observed. The scattering of light causes this by catalyst particles leading to eventual loss of the number of radicals generated by hindering full use of light. Also, aggregation of photocatalyst in slurry type has been observed. This highly reduces the surface area for exposure to light and results in less radical formation. This eventually reduces the photocatalytic reactions.

Permeate flux has been observed to fall by use of slurry type with membrane sharply. This is caused by photocatalyst nanoparticles getting deposited in the membrane pores, causing blockage and hindering further usability.

2.6.1 Immobilized photocatalyst on membrane

The selection of the type of membrane is key to prolonged usage. The membrane should display good mechanical strength, resistance to radical oxidation, resistance to radical reduction, resistance to UV decomposition, resistance to fouling, and high selectivity. PVDF polymeric membrane matches the attributes mentioned, only being faced with hydrophobicity. Hydrophobicity causes problems by attracting organic and bio foulants due to their hydrophobicity. This attraction eventually leads to fouling. Nitrogen-doped TiO_2 catalyst is hydrophilic. Immobilizing nitrogen dopped-TiO_2 on membrane reduces hydrophobicity of membrane and thereby reduces fouling.

With immobilized photocatalyst on a membrane, photocatalyst nanoparticle fouling as observed in slurry type is avoided. This leads to more prolonged use with quality permeate. Furthermore, the aggregation of photocatalyst and light scattering is minimized, leading to consistent quality permeate flux.

The use of immobilized photocatalyst on the membrane is economically cheap and attractive and will attract industrial scale.

Immobilization into the membrane is not favorable as it hinders and minimizes direct contact of pollutants with photocatalyst leading to low performance.

2.7 Summary

The literature review section has identified current and future water scarcity and water shortage problems that will be faced. A possible additional source of water can be secondary wastewater. To make these possible, tertiary methods have to be applied to assure quality for water to be reused. Todays' wastewater is heavily loaded with biological contaminants and organic contaminants that are recalcitrant and end up getting released. Among the contaminants, *E.coli* and sulphamethoxazole were selected as biological and organic contaminants of focus. Several tertiary methods were identified and their setbacks that hinder full implementation of the technologies. Among the methods discussed, photocatalysis and membrane were of interest. Photocatalysis utilizes semiconductors and light of equal or higher photon energy to promote electrons from valence band to conduction band, creating holes. The hole and radical will lead to radicals that mineralise organics and destroy microbes. TiO_2 appeared to edge out other photocatalysts in wastewater reclamation due to its superiority. It was of interest both economically and applicability to increase its efficiency and make it utilize sunlight to avoid using electric lamps. TiO_2 doping realized this. Among the anionic dopants, nitrogen effectiveness, modification, and doping mechanism was researched. Membrane separation utilizes size exclusion as its primary separation mechanism and does only phase transformation to more concreted phases.

Hybridization of photocatalysis and membrane separation enhanced each other by addressing setbacks faced by sole use of each technology in organic degradation and disinfection in wastewater. Therefore, this research addressed the issues such as photocatalyst secondary pollution, photocatalyst sunlight utilization, hydrophobicity of membranes, membrane fouling, photocatalyst reusability, membrane lifespan, and the effectiveness of photocatalytic membranes in handling contaminants of focus. Below are articles showing its findings and research gaps or future prospects that have been identified.

Table 2.2: Articles, findings and their research gaps or future prospects

Publication	Findings	Research gaps
(Kairigo, Ngumba, Sundberg, Gachanja, & Tuhkanen, 2020)	• Antibiotic levels in wwtp and water bodies.	• Prioritization of mitigation and prevention in areas affected.
(K'oreje, et al., Occurrence patterns of pharmaceutical residues inwastewater, surface water and groundwater of Nairobi and Kisumu city, Kenya, 2016)	• Identified water quality parameters and concentration in wwtp, rivers and ground water in Nairobi.	• Measures to eliminate pharmaceuticals in water.
(Rivero, Ribao, Gomez-Ruiz, Urtiaga, & Ortiz, 2020)	• Deposited TiO_2 on cellulose fabric and carried disinfection of ecoli using lamp.	• Unattractive use of lamps in applicability. • Poor uv responsiveness of TiO2 in disinfection.
(Ezugbe & Rathilal, 2020)	• Identified fouling types, cleaning techniques and membrane modules.	• Development of fouling resistant membranes • High energy concerns.
(Du, et al., The ecotoxicology of titanium dioxide nanoparticles, an important engineering nanomaterial, 2019)	• Identified human health hazard related to TiO_2 nanoparticles exposure. • Identified toxicity mechanism on TiO_2 nanoparticles.	• Prevention of nanoparticle pollution in application of TiO_2 nanoparticles.
(Mohammed, Palaniandy, & Shaik, 2021)	• Identified different reactor configuration. • Evaluated performance of photocatalytic membrane.	• Development of visible light responsive photocatalyst.
(Natarajan, Mozhiarasi, & Tayade, 2021)	• Identified different doping methods and properties. • Illustrated structural, electrical and morphological changes in doping	• Catalyst challenges in recovery and reusability.
(Subramaniam, Goh, Lau, Ng, & Ismail, 2019)	• Explored characteristics of pollutants. • Explored methods for effluent treatment • Explored photocatalytic degradation.	• Nanoparticle agglomeration. • Sunlight utilization.
(Subramaniam M. N., Goh, Kanakaraju, Lim, Lau, & Ismail, 2021)	• Identified roles of photocatalysis and membrane technologies in photocatalytic membrane. • Identified persistent organic pollutants origin and effects. • Identified mechanisms and designs of photocatalysts.	• Use of sunlight for feasibility • Better deposition of photocatalyst.

	• Catalyst deposition by physical vapour deposition.	
(Chen, Hu, Xie, & Wang, Materials and Design of Photocatalytic Membranes, 2018)	• Identified different membrane configuration. • Identified materials for membranes and photocatlytic membrane applications • Identified fabrication techniques	• Lower contact area between pollutant and catalyst. • Utilization of sunlight.
(Tung, Ananpattarachai, & Kajitvichyanukul, 2018)	• Application and decomposition of persistent organic pollutants. • Analyzed suspended and immobilized TiO_2 membranes. • Identified factors affecting photocatalytic membrane	• Utilization of sunlight. • Uv responsiveness of TiO_2

CHAPTER THREE: MATERIALS AND METHODS

3.1 Materials and Equipment

The following materials in Table 3.1 were used.

Table 3.1: Materials used with their sources.

Item number	materials	Sources
1	15nm TiO_2 anatase powder	Department30413 store, AliExpress, (china)
2	Urea (AR)	Sigma-Aldrich (Kenya)
3	Deionized water	Gelsup E.A(Kenya)
4	Polyvinyl alcohol (PVA),	Gelsup E.A(Kenya)
5	glutaraldehyde 25%,	Kobian scientific (Kenya)
6	sulphuric acid	Gelsup E.A(Kenya)
7	PVDF ultra-filtration membranes	Linyeuyue labolatory supplies factory store, AliExpress, (china)
8	Distilled water	P.L Huisman Lab (Moi university)
9	Hydrochloric acid	Gelsup E.A(Kenya)
10	Sodium chloride	Gelsup E.A(Kenya)
11	Sodium hydroxide	Gelsup E.A(Kenya)
12	*E.coli* culture	Moi Teaching and Referral Hospital
13	Tryptic soy agar	Gelsup E.A(Kenya)
14	Sulphamethoxazole.	Sigma-Aldrich,
15	Ethanol	Gelsup E.A(Kenya)
16	Cotton wool	Eldo-Laboratory Supplies. (Kenya)
17	Culturing petri dishes	Eldo-Laboratory Supplies. (Kenya)
18	Cheesecloth	Eldo-Laboratory Supplies. (Kenya)

The following equipment were used: High precision balance (model HZT-A200), twin blade mixer (nutribullet 600 series), Magnetic stirrer hotplate, Homogenizer bath (Rico scientific inds. Usbt-6-liters) , muffle furnace (CARBOLITE GERO ELF 11/14B), oven (Labtech LDO-150),UV-Vis spectrophotometer (General purpose UV/Vis

spectrophotometer (DU 720), photoluminesce spectra(Horiba, LabRam HR model), X-ray diffractionator(Rigaku, Smartlab X-Ray Diffractometer), Scanning electron microscopy/Energy-dispersive X-Ray spectroscopy(Zeiss, Ultra55), Fourier transform infrared spectroscopy(Perkinelmer, Frontier), parabolic dish reflector(focal point 34cm,diameter 61.85cm), water contact meter(in-house custom-made) Source tank, centrifuge, hemocytometer (MARIENFIELD 0.0025mm^2,Germany), microscope (euromex iscope series), light radiometer, UV-Vis spectrophotometer (SHIMADZU UV-1800), TOC analyzer (analytikjena multi N/C 2100S/1), water system pump(model FL-2202), Flow regulating valve, in house cross filtration setup(height 5.08cm, 7cm diameter chamber, pyrex glass 8mm), rubber seals, manual solar trucking setup, Connecting pipes, jic fittings, aluminum reflective tape, aluminum foil, dc voltage inverter, syringe, syringe filters, weighing balance, wire loop, autoclave (tuttnaver LAB048-0070-A), lamina flow hood(Telstar Aeolus H), micropipette, incubator(VWR INCU-Line ILIO), glass rod, pH meter (senION+ HACH-LANGE,S.L.U)

3.2 Methods

3.2.1 Synthesis and characterization of nitrogen doped TiO_2 nanoparticles (N-TiO_2) and membrane

3.2.1.1 Synthesis of N-TiO_2 nanoparticles

Equimolar amounts of TiO_2 and urea were mixed and blended using a mixer for 10 minutes (Selvaraj, Parimiladevi, & Rajesh, Synthesis of Nitrogen Doped Titanium Dioxide (TiO2) and its Photocatalytic Performance for the Degradation of Indigo Carmine Dye, 2013). The TiO_2 - urea mixture was then put in a crucible and heated for 5 hours at temperatures of 500^{O}C. The mixture in the crucible was left to cool to room temperature and blended for 10 minutes.

3.2.1.2 N-TiO_2 nanoparticles immobilization on membrane

The first step to the membrane immobilization entailed rinsing the PVDF membrane with ethanol and thereafter drying the membrane; these were attained at room temperature. In the second step, 2wt% PVA particles were mixed with deionized water at 97^{o}C for 300 minutes and cooled. Next (3rd step), to attain homogenization, 1wt% N-TiO_2 nanoparticles were added to 2wt% PVA solution in the beaker and homogenized using sonic bath for 90 minutes. In the fourth step, the PVDF membrane was then dipped into a PVA/N-TiO_2 slurry for 13 minutes to immobilize N-TiO_2 onto the PVDF membrane. The membrane was then removed from the slurry mixture and open-air-dried for 30 minutes and thereafter prepared for functional group cross-linking.

Meanwhile, 600 ml of the functional groups linking solution was prepared. This was done by mixing 2wt% glutaraldehyde ($C_5H_8O_2$) 25% and 0.5wt% sulphuric acid 98% and divided into two portions. The first portion, 300 ml was stored at room temperature and the second portion, 300 ml was stored at 60^{o}C in an oven; the selected temperature was to prevent the membrane from swelling.

The membranes from step 4 were then placed in these linking solutions for 5 minutes and 2 minutes for the first portion and second portion respectively to enable cross-linking and the process repeated twice. The final step entailed removing the cross-linked and PVA/N-TiO_2 immobilized membranes from the linking solution and oven-drying them for 5 minutes at 59^{o}C after they were washed with deionized water and dried. The membranes were now ready for characterization.

3.2.1.3 Nanoparticles and membranes characterization

Samples of N-TiO_2 and TiO_2 were characterized for doping effects through absorbance at full wavelength scan range(250nm-800nm) by UV/Vis spectroscopy. The band gap energies were evaluated with the following Equation 3.1:

$$Eg = \frac{hc}{\lambda}$$ Equation 3.1

Where h is the planc's constant ($4.1357x10^{-6}$ eV.nm), C light velocity ($2.979x10^{8}$m/s) and λ wavelength of the tangential arrow from the linear part of the curve.

The effectiveness of charge separation and suppression of recombination using 266nm laser was conducted through photoluminesce test. X-ray diffraction (XRD) was used in determination of crystallinity of TiO_2, N-TiO_2, PVDF and N-TiO_2-PVDF at 2θ at a scanning range of 10-90^o using XRD equipment. The crystallite size was evaluated with the following equation 3.2:

$$Crystalite\ size = \frac{k\lambda}{FWHM.COS\theta}$$ Equation 3.2

Where k is the shape factor 0.9(for spherical nanoparticles), θ is angle between X-ray source and detector and FWHM is the full width at half maximum.

Fourier transform infrared spectra (FTIR) within range of 400-4000cm^{-1} was done for TiO_2 and N-TiO_2 and within range of 650-4000 cm^{-1} for PVDF and N-TiO_2-PVDF for identification of functional groups through vibrations and stretches using FTIR equipment. Scanning electron microscope/Energy dispersive X-ray (SEM-EDX) was conducted for the surface morphology and chemical composition was investigated for TiO_2, N-TiO_2, PVDF and N-TiO_2-PVDF using SEM-EDX. The hydrophilicity through water contact angles were studied for PVDF and N-TiO_2-PVDF using water contact meter.

3.2.2 Optimum conditions for disinfection and degradation of organic pollutants by solar photocatalysis

Response Surface Methodology (RSM) and Central Composite Design (CCD) were used to model and determine the optimal conditions for disinfection, degradation and flux. The independent variables were pH and sodium chloride concentration. The responses were percentage degradation and TOC for 1st set of experiments, percentage disinfection for 2nd set of experiments and flux for both sets of experiments. The range selected for independent variables is 4 to 10 for pH and 7 g/l to 40 g/l for NaCl concentration. The use of design expert version 13 software gave the following coded values as shown in Table 3.2.

Table 3.2: Coded and actual range values for independent variables

Independent variable	**-α (-1.414)**	**-1**	**0**	**1**	**α (1.414)**
pH	2.75736	4	7	10	11.2426
NaCl concentration(g/l)	0.16476	7	23.5	40	46.8345

3.2.2.1 Degradation, flux and TOC removal of sulphamethoxazole pollutant

A volume 1.2 L deionized water was pH adjusted (by HCL and NaOH) and added NaCl as per the design expert values. 7.2 mg of sulphamethoxazole was then added and sonicated for 45 minutes. The intensity of solar radiation was then determined by a light radiometer. The resulting mixture was then taken to the equipment setup in Figure 3.1.

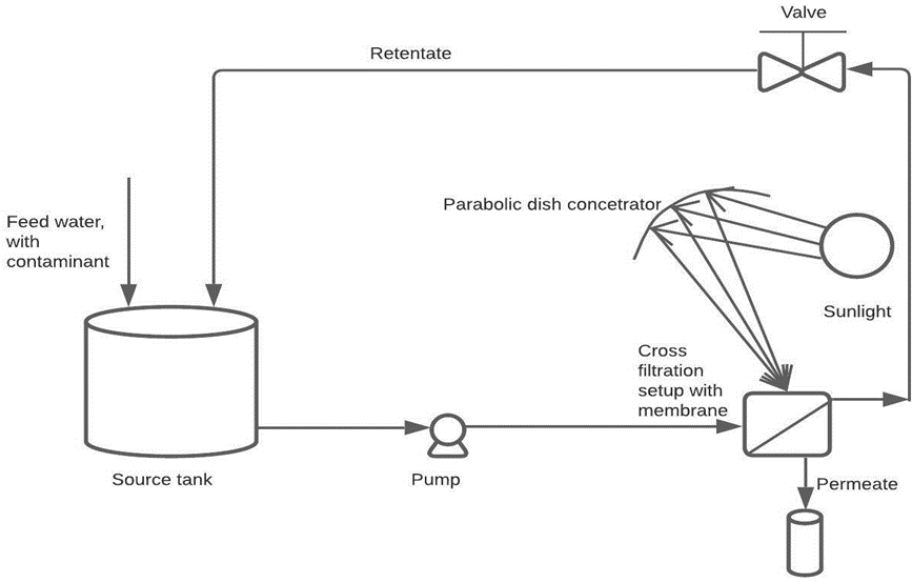

Figure 3.1: Schematic representation of photocatalytic experimental setup

A sample was drawn from measured permeate and analyzed by UV-Vis spectrophotometer and TOC analyzer to quantify sulphamethoxazole. Experiments were then repeated for the rest of the values the design expert gave.

The design expert version 13 software gave the following 5 center points and 8 non-center points, as shown in Figure 3.2.

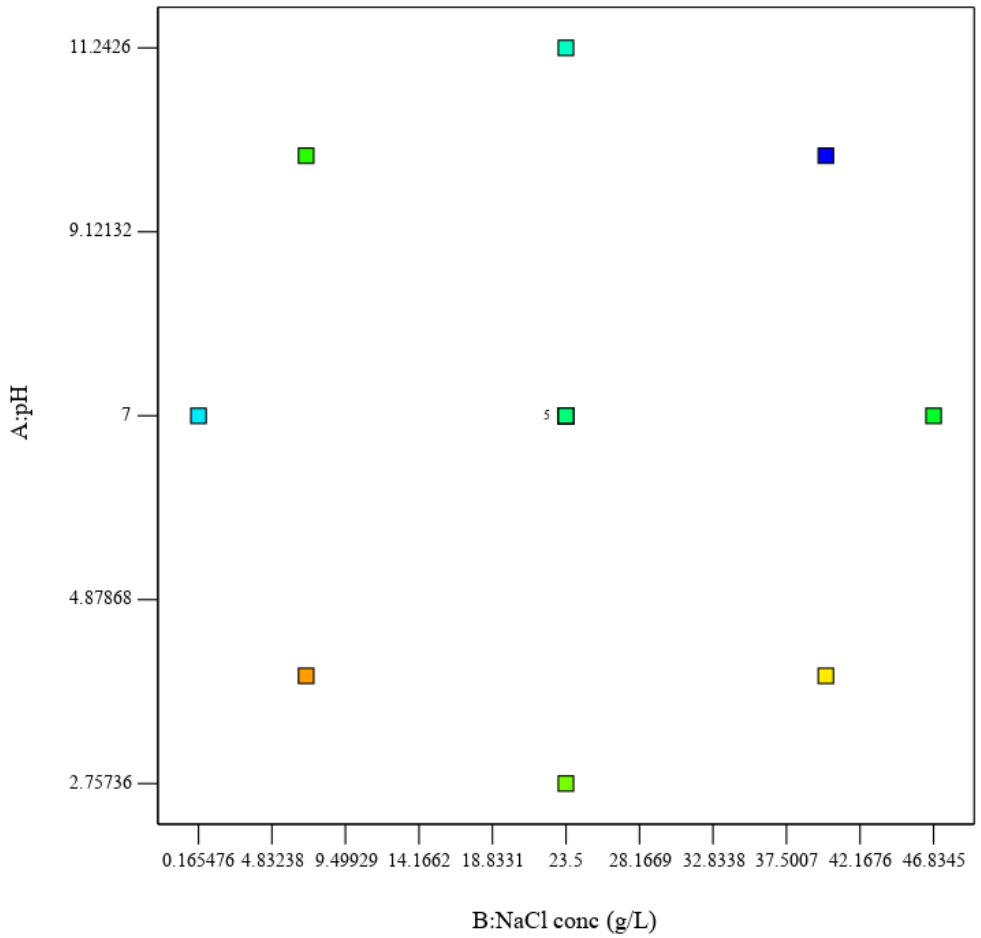

Figure 3.2: Image points for 1st set experiments

3.2.2.2 Disinfection and flux for *E.coli* pollutant

An amount 39 g of soybean agar was weighed and placed in 1.5 L conical flask and 1 L distilled water was added. The mixture was preheated using a magnetic stirring hotplate until full dissolution of soybean agar. The conical flask was then covered with sterile cotton and aluminum foil. It was autoclaved at 103.4 kPa and 120^{o}C for 20 minutes and then left to cool to 45^{o}C. The mixture was then poured into Petri dishes in a laminar flow hood and cooled into a gel. Pure culture was then flooded with distilled water and poured onto Petri dishes with the gel. The petri dishes were then covered, sealed, and incubated at 37^{o}C for 24 hours. 4 Petri dishes were then opened in a laminar flow hood, flooded with distilled water and culture disrupted using a glass rod to free the cells from the culture colonies. The suspension was then passed through double

cheesecloth into a beaker. A stock solution was prepared by topping up 700ml of distilled water and refrigerated at 4^{o}C. A drop of stock solution was put in hemocytometer (of 0.004mm^{3}) using a micro pipette, covered with a glass slip and bacteria were counted using a compound microscope at X40 and X100 magnification. 20ml of the stock solution was then added to 980ml of pH and salt-adjusted distilled water (as per the design expert). The intensity of solar radiation was then determined by light radiometer. The resulting mixture was then taken to the equipment setup in figure 3.1. To quantify *E.coli*, a sample was drawn from measured permeate and analyzed for bacterial count using a haemocytometer and a microscope. Consequently, a culturing regrowth test was also done for the samples collected pouring 20ml of permeate onto Petri dishes with soybean gel similarly prepared as earlier and incubated at 37^{o}C for 24 hrs. Experiments were then repeated for the rest of values given by the design expert. Together cultured were positive and negative culturing controls.

The design expert version 13 software gave the following 5 center points and 8 non-center points, as shown in Figure 3.3.

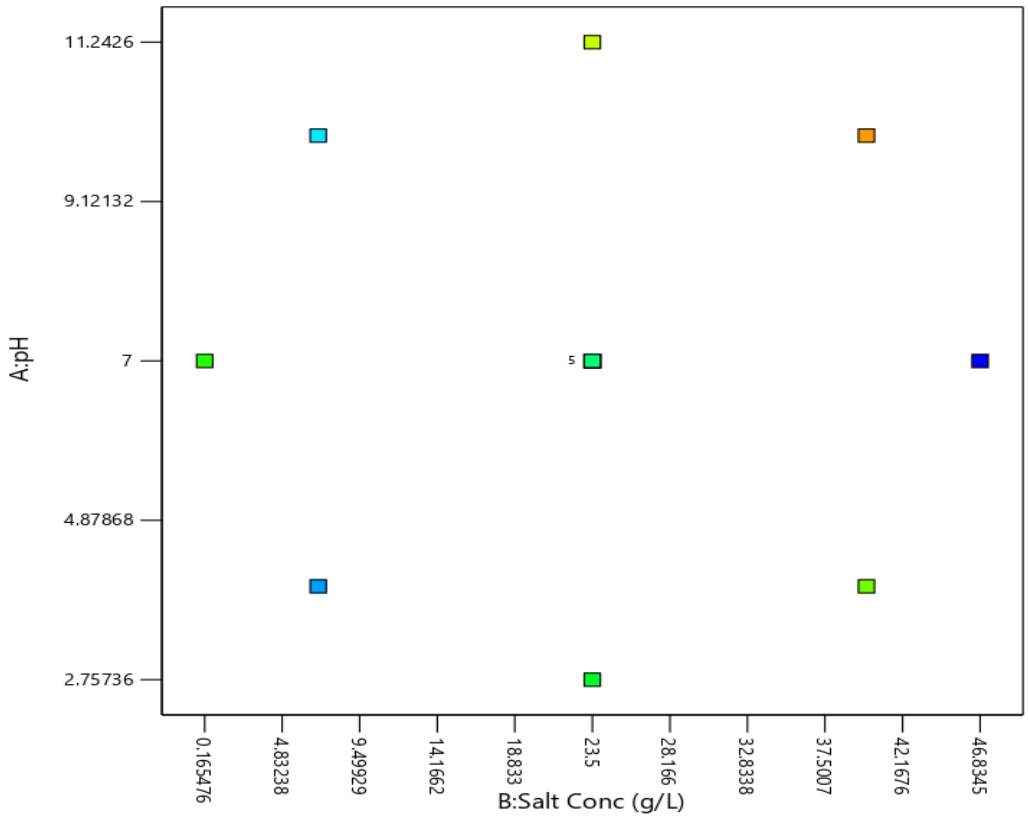

Figure 3.3: Image points for 2nd set disinfection experiments

3.2.3 Performance of photocatalytic membranes, durability and reuse

3.2.3.1 Performance, durability and reuse with sulphamethoxazole pollutant

An amount 7.2mg of sulphamethoxazole was put in 1.2 liters of distilled water and pH was adjusted to 4, 7 and 10 solutions. The mixture was then sonicated for 45 minutes. The resulting solution was taken to the experimental setup in Figure 3.1. The intensity of solar radiation was determined by light radiometer. Stopwatch was set to zero. The amount of permeate was measured and the Retentate sample was collected every 25 minutes to determine the amount of SMX remaining (by use of UV-vis spectrophotometer) and TOC remaining (by use of TOC analyzer). Amounts 7.2mg, 12mg and 16.8 each of sulphamethoxazole were put in each of 1.2 liters of distilled water and sonicated for 45 minutes. The resulting solution was taken to the experimental setup in Figure 3.1. The intensity of solar radiation was determined by a

light radiometer. Stopwatch was set to zero. The amount of permeate was measured and retentate samples were collected as well every 25 minutes for determination of the amount of SMX remaining (by use of UV-vis spectrophotometer) and TOC remaining (by use of TOC analyzer).

An amount 36mg of sulphamethoxazole was put in 6 liters of distilled water and sonicated for 45 minutes. The solution was then divided into 5 portions of 1.2 liters. 1st portion was taken to the experimental setup in Figure 3.1. The intensity of solar radiation was determined by a light radiometer. The experiment was run for 100 minutes and permeate was measured after every 25 minutes. Retentate samples were also picked after each 25 minutes for analysis of SMX remaining (by use of UV-vis spectrophotometer), TOC (by use of TOC analyzer). The photocatalytic membrane was then backwashed for 5 minutes using deionized water, and pure water flux was measured and returned to the experimental setup for the 2nd portion. The experiment was then repeated for the rest of the portions.

3.2.2.3 Performance, durability and reuse with *E.coli*

A 20ml of 5.2X10^{10} CFU/l *E.coli* stock suspension was put in 980ml of distilled water and pH was adjusted to 4, 7 and 10 solutions. The resulting solution was taken to the experimental setup in Figure 3.1. The intensity of solar radiation was determined by light radiometer. Stopwatch was set to zero. The amount of permeate was measured and retentate sample was collected as well every 25 minutes for determination of bacterial count (by use of hemocytometer and microscope). 20ml, 10ml and 5ml of 5.2X10^{10} CFU/l *E.coli* stock suspension was put in 980ml, 990ml and 995ml of distilled water. The resulting solution was taken to the experimental setup in Figure 3.1. The intensity of solar radiation was determined by light radiometer. Stopwatch was set to zero. The amount of permeate was measured and retentate samples were collected for every 25

minutes to determine bacterial count by using hemocytometer, counter and a microscope.

A 100 ml of $5.2X10^{10}$ CFU/l *E.coli* stock suspension was put in 4.9 liters of distilled water. The solution was then divided into 5 portions of 1 liter. 1st portion was taken to the experimental setup in Figure 3.1. The intensity of solar radiation was determined by light radiometer. The experiment was run for 100 minutes and permeate was measured after every 25 minutes. Retentate samples were also collected for every 25 minutes for determination of bacterial count (by use of hemocytometer and microscope). The photocatalytic membrane was then backwashed for 5 minutes using deionized water, and pure water flux was measured and returned to the experimental setup for the 2nd portion. The experiment was then repeated for the rest of the portions.

CHAPTER FOUR: RESULTS AND DISCUSSION

4.1 Characterization of Photocatalyst and Membrane, TiO_2, N-TiO_2, PVDF and N-TiO_2-PVDF

4.1.1 Characterization of photocatalysts, TiO_2 and N-TiO_2

4.1.1.1 UV-Vis spectroscopy

The effect of doping titanium dioxide with nitrogen from urea precursor was investigated by UV/Vis spectrophotometer and the results presented in Figure 4.1.

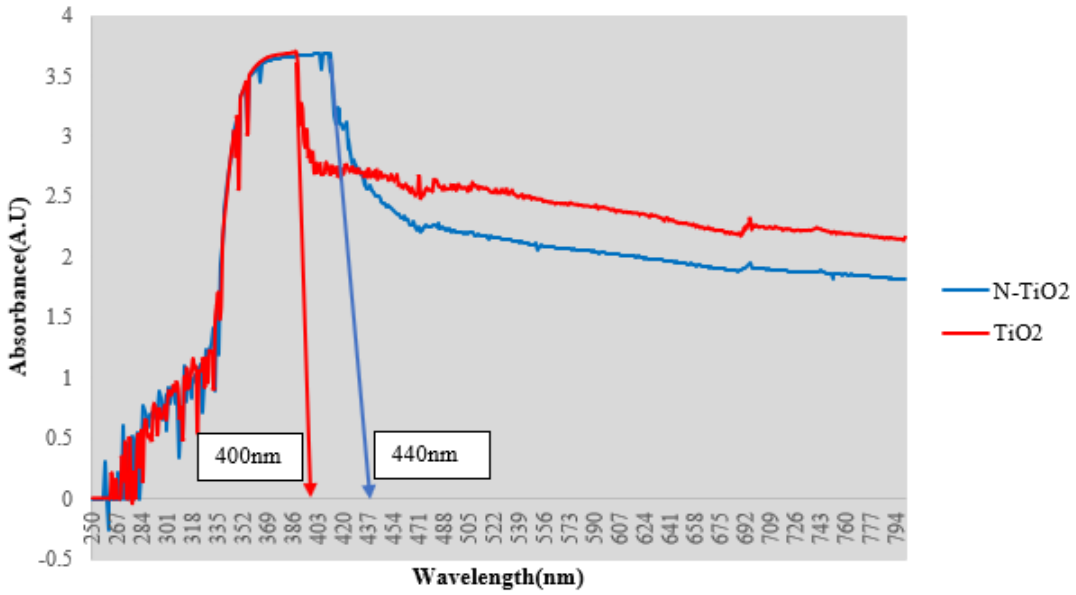

Figure 4.1: UV/Vis Absorbance full wavelength spectra for TiO_2 and N-TiO_2 with tangential arrows indicating absorbance wavelengths

The absorbance on nitrogen doped titanium dioxide (indicated as 440nm) improved toward the visible region of 400nm-700nm from its original titanium dioxide (indicated as 400nm) absorbance UV region of 200-400nm. The bandgap energy for TiO_2 was evaluated to be 3.10eg and N-TiO_2 to be 2.82eg (Ntozakhe, Taziwa, & HHMungondori, 2019); which is in line with finding from (Selvaraj, Parimiladevi, & Rajesh, 2013). The drawn tangential arrows in the Figure 4.1 showed red shifting attributed to interstitial nitrogen forming an intermediate bandgap (called N2P level of energy) above O2p and

below the titanium dioxide valence band (Tao, Mo, & Tong, 2019). This N2P intermediate band caused a bandgap that required light of long wavelengths and less energy (visible light) to activate electrons transfer from N2P to the conduction band of titanium dioxide. This made improvements in photocatalytic activity.

4.1.1.2 Photoluminesce spectra

The effectiveness of doping with nitrogen was conducted with photoluminesce (PL) spectra for TiO_2 and N-TiO_2 nanoparticles to study the efficiency of photo-separated electrons and holes, their trapping and capturing, and their recombinations. The results are shown in Figure 4.2.

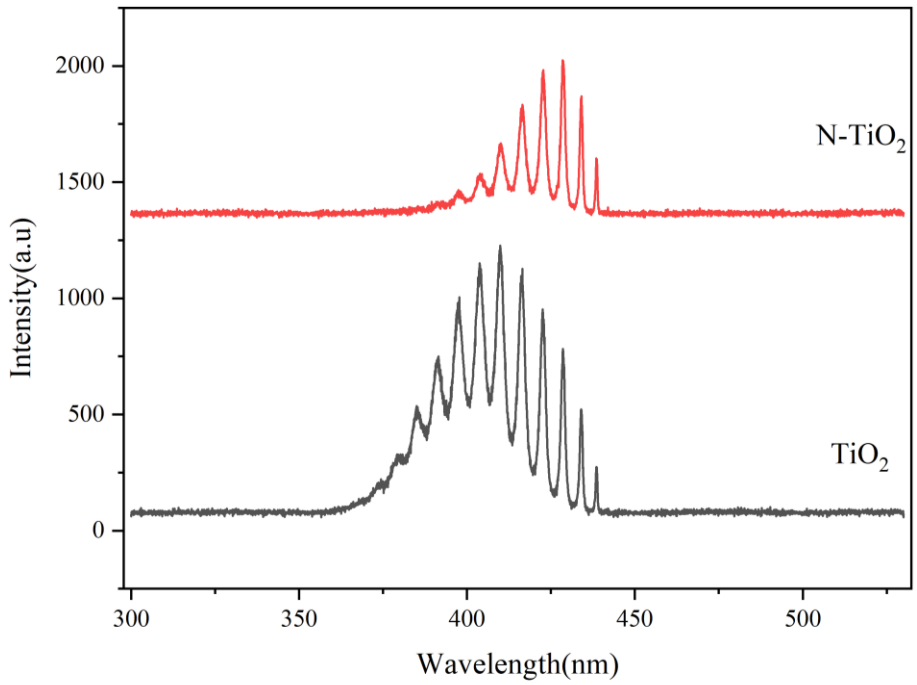

Figure 4.2: Difference in PL spectra intensity of TiO_2 and N-TiO_2 266nm laser scanning.

Recombinations of separated holes and electrons happen when electrons separated in CB enter oxygen vacancies and get attracted to holes. They then recombine with holes in VB, releasing photon energy through longer wavelength light luminescence (Wang, He, Zhao, Chenc, & Cao, 2011). The intensity of PL spectra emission is a result of

recombinations of electrons and holes (Selvam, Balachandran, Velmurugan, & Swaminathan, 2012). Higher PL spectra intensity indicated a higher rate of recombination of charges, an implication of poor performance in the generation of radicals for degradation and disinfection and vice versa. (Rasoulnezhad, Hosseinzadeh, Hosseinzadeh, & Ghasemian, 2018). Lower intensity was displayed by N-TiO_2 as compared to TiO_2 (in Figure 4.2); this indicated the effectiveness of nitrogen doping in enhancing better charge separation and suppression of its recombination (Mehrabad, Partovi, Rad, & Khalilnezhad, 2019). This improvement is attributed to better capturing of photogenerated holes by reduced Ti^{3+} ions (Khan, et al., 2021).

4.1.1.3 Fourier transform infrared spectra

TiO_2 and N-TiO_2 nanoparticles were characterized by FTIR as shown in Figure 4.3.

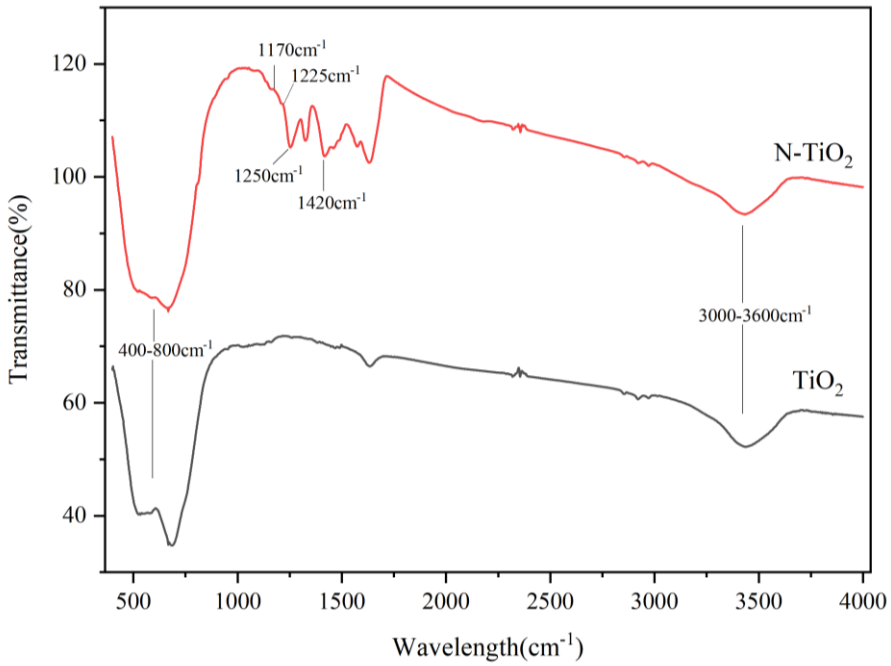

Figure 4.3: FTIR transmittances for TiO_2 and N-TiO_2 nanoparticles with notable peaks and vibrational stretches

The low-frequency broad band ranging from 400-800cm^{-1} is a typical stretching vibrations characteristic belonging to Ti-O, O-Ti-O, Ti-O-Ti bonding types and is

present in both nanoparticles as expected (Yu, et al., 2003), (Giannakopoulou, et al., 2017).

Both TiO_2 and N-TiO_2 displayed a distinctive peak at approximately 1630cm^{-1} and in the range of 3000-3600cm^{-1}. This is attributed to the hydroxyl groups and water in molecular form (Du, Bai, Xu, Yang, & Jin, 2020), (Wang, Zhu, Zhang, & Liu, 2007). The presence of hydroxyl groups is of great importance in that they sink the photogenerated holes and lead to the formation of hydroxyl radicals. Furthermore, they harbor oxygen molecules that also contribute to forming hydroxyl radicals (Cheng, Yu, Xing, & Yang, 2016).The characteristic peak at 1420cm^{-1} and 1170cm^{-1} can be attributed to the presence of interstitial nitrogen atoms that exist in the lattice network of N-TiO_2 (Kairigo, Ngumba, Sundberg, Gachanja, & Tuhkanen, 2020) whereas the bending vibrations at 1220cm^{-1} and 1250cm^{-1} was attributed to substitutional nitrogen that leads to formation of -TiN (Yang, Jiang, Shi, Xiao, & Yan, 2010), (huo, jin, zhu, & li, 2009). The presence of both interstitial and substitutional nitrogen indicates that doping was successful.

4.1.1.4 X-ray diffraction

TiO_2 and N-TiO_2 nanoparticles were investigated by XRD and the results shown in Figure 4.4.

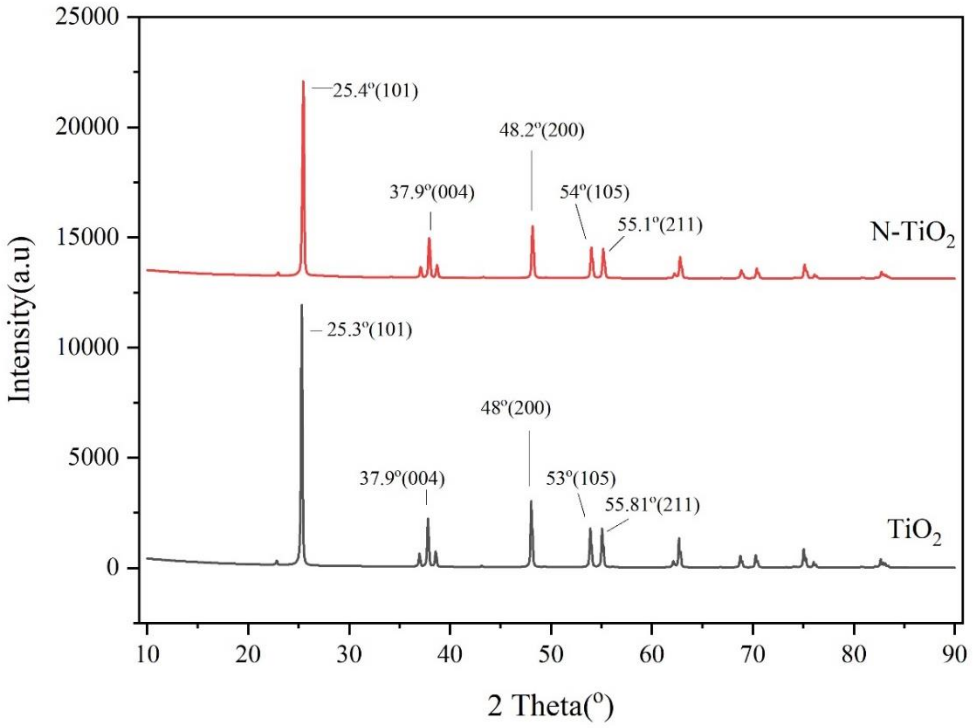

Figure 4.4: XRD spectrum crystallinity patterns for TiO_2 and N-TiO_2

TiO_2 displayed peaks at 25.3° (101 diffraction plane), 37.9° (004 diffraction plane), 48.0° (200 diffraction plane), 53.9° (105 diffraction plane) and 55.18° (211 diffraction plane). N-TiO_2 displayed peaks at 25.4° (101 diffraction plane),37.9° (004 diffraction plane),48.2° (200 diffraction plane),54.0° (105 diffraction plane),55.1° (211 diffraction plane). All the peaks were coinciding and comparable to JCPDS standard card no. 21-1272 for anatase of space group 141/amd (Khan, et al.2021). Rutile peaks defined by JCPDS standard card No. 89-4920 were not detected, indicating that the temperatures from the set furnace and exothermic disintegration of urea were not high to transform anatase phases to rutile for the dopant.

The diffraction peaks were at similar and close positions, with only significant changes detected at peak intensities. Nitrogen doping caused a decrease in XRD intensity. This was an indication of successful doping of nitrogen. The crystallite size was then calculated using Scherrer equation based on the 101 diffraction plane using values from Origin software. The origin software gave Xc(2θ) as 25.31178° for TiO_2 and Xc(2θ) as

25.45367^{o} for N-TiO_2. The full width at half maximum (FWHM) for TiO_2 was 0.00310756 radians. The FWHM for N-TiO_2 was 0.003489 radians. (Ntozakhe, Taziwa, & HHMungondori, 2019). The crystallite size for TiO_2 was 45.7281nm whereas for N-TiO_2 was 40.7331nm. This was another indication of successful doping into the lattice as the crystallite size decreased, similar to those found by (Wahyuni, Rahmaniati, Hafidzah, Suherman, & Suratman, 2021) and (Zhang, et al., 2014).

Nitrogen diffraction peaks could not be detected because nitrogen was dispersed evenly in titanium dioxide hindering any possibility to agglomeration to levels that could be detectable. This may possibly be attributed to the proper mixing of TiO_2 and urea by the twin blade mixer before temperature treatment of 500^{o}C in the furnace.

4.1.1.5 Scanning electron microscope/Energy dispersive X-ray

SEM characterization was undertaken under 2Kv on TiO_2 and N-TiO_2 nanoparticles to study its morphology and dispersion of the nanoparticles under x50 and x100 magnifications as shown in Figure 4.5 and 4.6.

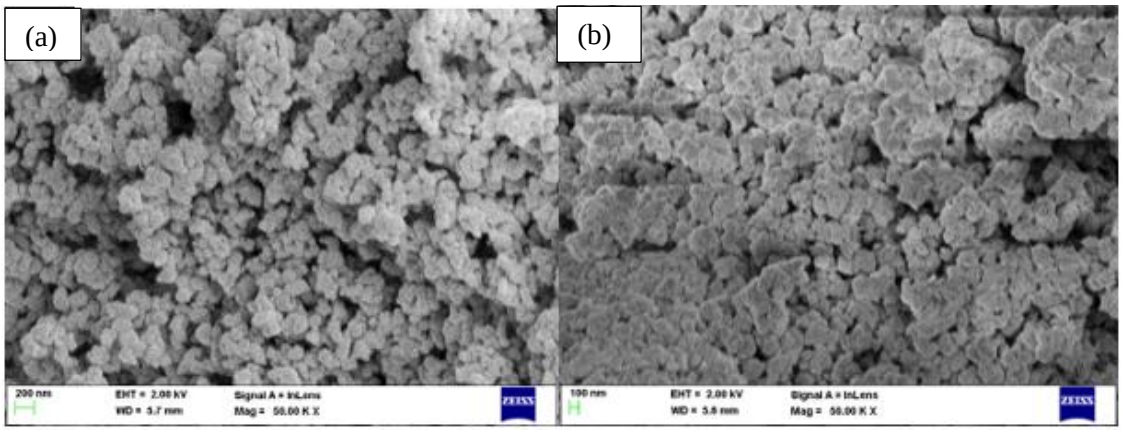

Figure 4.5: SEM images at X50 magnification for (a) TiO_2 and (b) N-TiO_2

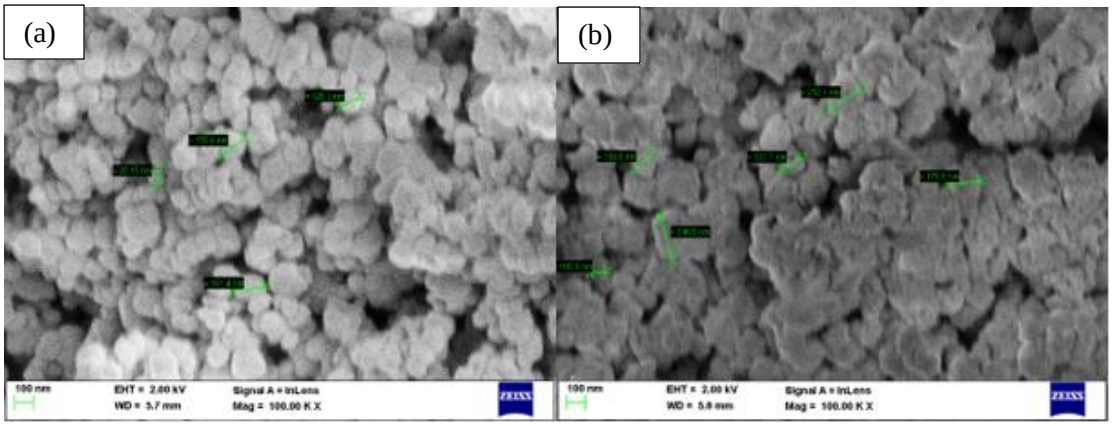

Figure 4.6: SEM images at x100 magnification for (a)TiO_2 and (b) N-TiO_2 with particle size randomly selected and determined

Both images under x50 and x100 showed both nanoparticles to exist in spherical nanoscale shapes. However, there were no obvious changes in the size of the nanoparticles after doping with both nanoparticles ranging from 92nm to 212nm (Lin, Weng, Srivastav, Lin, & Tzeng, 2014). This is attributed to the comparable size of oxygen atoms' radii and nitrogen atoms' radii of 140Å and 170Å, respectively (Natarajan, Mozhiarasi, & Tayade, 2021).

The introduction of nitrogen (and possible use of urea precursor) showed some aggregation of nanoparticles, with the image belonging to N-TiO_2 showing slightly more compaction. None of the urea particles could be distinguished from the images. This is an indication that furnace temperatures of 500^oC were able to disintegrate urea particles during doping fully.

EDX was used to identify chemical elemental compositions and purity of TiO_2 and N-TiO_2 nanoparticles as shown in Table 4.1.

Table 4.1: Elemental chemical composition for TiO_2 and N-TiO_2 by EDX.

Element	**TiO_2**		**N-TiO_2**	
	Weight%	Atomic%	Weight%	Atomic%
C	3.48	6.52	4.23	9.22
N	**0.00**	**0.00**	**1.26**	**2.36**
O	51.52	72.37	33.67	55.14
F	0.00	0.00	0.00	0.00
S	0.00	0.00	0.00	0.00
Ti	45	21.11	60.84	33.28
Fe	0.00	0.00	0.00	0.00
Zn	0.00	0.00	0.00	0.00
Totals	**100**	**100**	**100**	**100**

The characteristic peaks of the x-ray region were then related to the elemental energy levels (Irshad, et al., 2020). TiO_2 displayed major peaks of Titanium and Oxygen. Notably not detected was nitrogen. Traces of carbon was detected, which might be attributed to minor contamination in manufacturers' synthesis of Titanium dioxide. A detailed composition is indicated in Table 4.1. N-TiO_2 as well displayed major peaks belonging to Titanium and oxygen. A nitrogen peak was also detected. This suggested successful doping of nitrogen into titanium dioxide. In composition, the percentage of nitrogen was 1.26wt%. A minute existence in the TiO_2 lattice suggests an interstitial doping mechanism (Ocwelwang & Tichagwa, 2014). Notably is increased carbon content traces. This can be attributed to traces of urea still present.

4.1.2 Characterization of membranes, PVDF and N-TiO_2-PVDF

4.1.2.1 Fourier transform infrared spectra

PVDF and N-TiO_2-PVDF membrane was characterized by FTIR and the results shown in Figure 4.7.

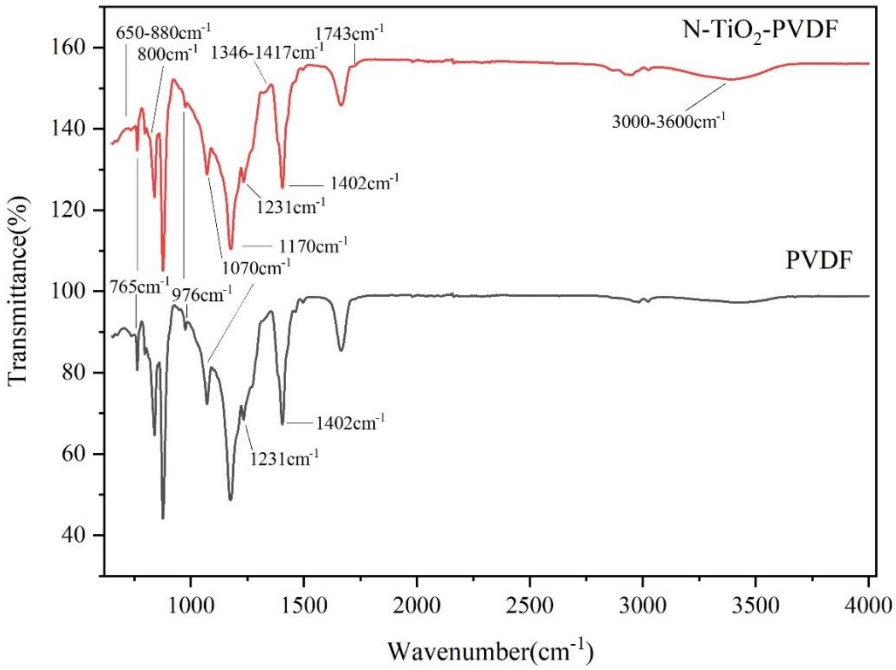

Figure 4.7: FTIR transmittances for PVDF and N-TiO_2-PVDF nanoparticles.

The suppressed transmittance at low-frequency band up to 880cm^{-1} by N-TiO_2-PVDF is a typical strong vibration stretch that describes the presence of Ti-O, Ti-O-Ti (Kamaludin, et al., 2020) for TiOp where p should be less than 6 (Cruz, Semblante, Senoro, You, & Lu, 2013). Specifically, the peak at 800cm^{-1} indicates the presence of anatase titania dioxide (Cruz, Semblante, Senoro, You, & Lu, 2013). Both membranes displayed strong vibration bands at 1070cm^{-1} and 1170cm^{-1} that were assigned stretching vibrations of -CF_2. This is a typical characteristic of any PVDF polymeric material. Furthermore, peaks at 765cm^{-1} and 976cm^{-1} are assigned to α-phase crystallinity of PVDF membranes (Kamaludin, et al., 2020), whereas peak at 1231cm^{-1} are for γ phase crystallinity of PVDF membrane (Wang & Ding, 2022). The vibration band at 1402cm^{-1} is additionally assigned to -CH_2 characteristic of a typical PVDF membrane.

N-TiO_2-PVDF uniquely indicated a peak at a region close to 1743cm^{-1}. This indicated the presence of carboxylic groups (Ondijo, Kengara, & K'Owino, 2022). This vibration was caused by glutaraldehyde used in the cross-linking (Sakarkar, Muthukumaran, &

Jegatheesan, 2020). Peaks ranging from 1346-1417cm^{-1} were assigned to the presence of dopant nitrogen that exists in titanium dioxide either substantially or interstitially (Kamaludin, et al., 2020). A vibrational stretch from 3000-3600cm^{-1} was assigned to -OH groups that indicated an increase in hydrophilicity. This was the majorly effect of hydrophilic PVA and partly N-TiO_2 incorporation onto PVDF membrane.

4.1.2.2 X-ray diffraction

PVDF and N-TiO_2-PVDF were analyzed by XRD and the results shown in Figure 4.8.

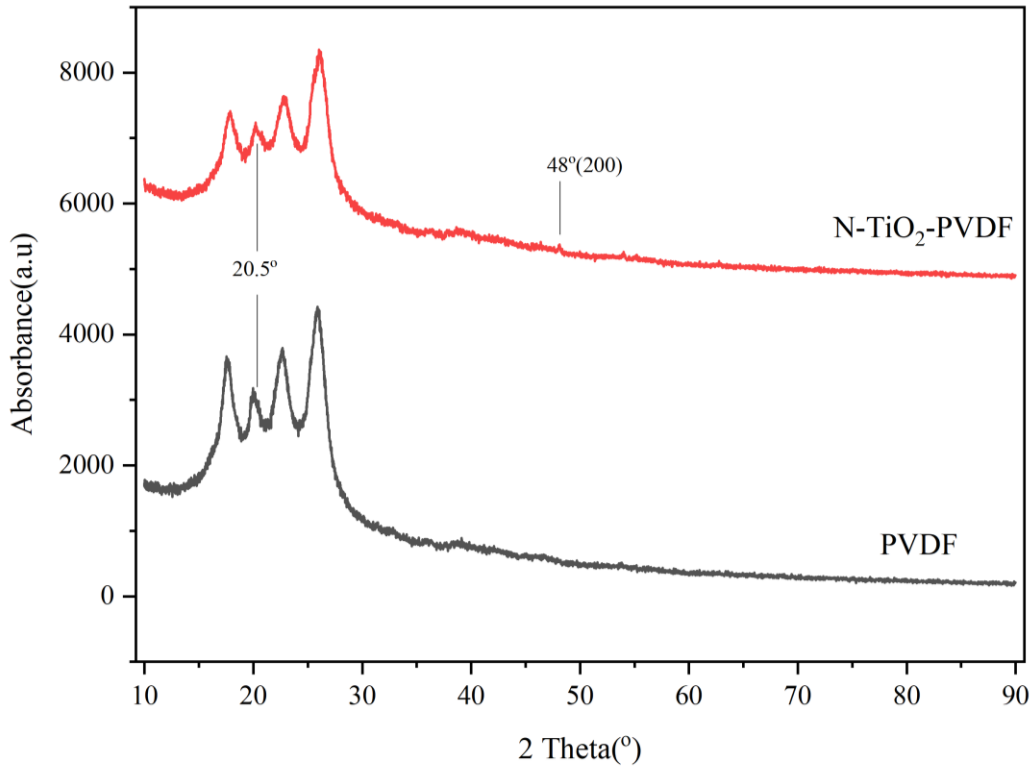

Figure 4.8: XRD spectrum crystallinity patterns for PVDF and N-TiO_2-PVDF

PVDF membrane showed a high-intensity peak region at 20.5° that indicated the presence of kinetically stable α phase crystallinity (Kamaludin, et al., 2020). N-TiO_2-PVDF had a similar peak at 20.5° that showed the presence of α phase and PVA semicrystaline peak coinciding at the same region (Sakarkar, Muthukumaran, & Jegatheesan, 2020). The coating and crosslinking of PVDF using PVA and Nitrogen-

doped titanium dioxide affects the chemical and mechanical characteristics through crystallinity. The intensity of the peak was suppressed due to the effect of titania doped nanoparticles presence that caused rearrangement and bonding to semicrystaline PVA via hydrogen bonds, eventually resulting to decrease in crystallinity and an increase in amorphousness (Khatua, et al., 2015). This indicated the presence of immobilized N-TiO_2. Additionally, TiO_2 has been shown to reduce crystallinity in PVA-coated membranes due to its agglomeration (Sakarkar, Muthukumaran, & Jegatheesan, 2020). The appearance of a peak near 48^o (plane 200) indicated anatase phase titania (Arif, Sethy, Kumari, Mishra, & Verma, 2019).

4.1.2.3 Scanning electron microscope with Energy dispersive X-ray

SEM characterization was undertaken under 2Kv on PVDF and N-TiO_2-PVDF membranes to study its morphology, dispersion of N-TiO_2 nanoparticles and PVA coating under x25, and x10 magnifications as shown in Figure 4.9.

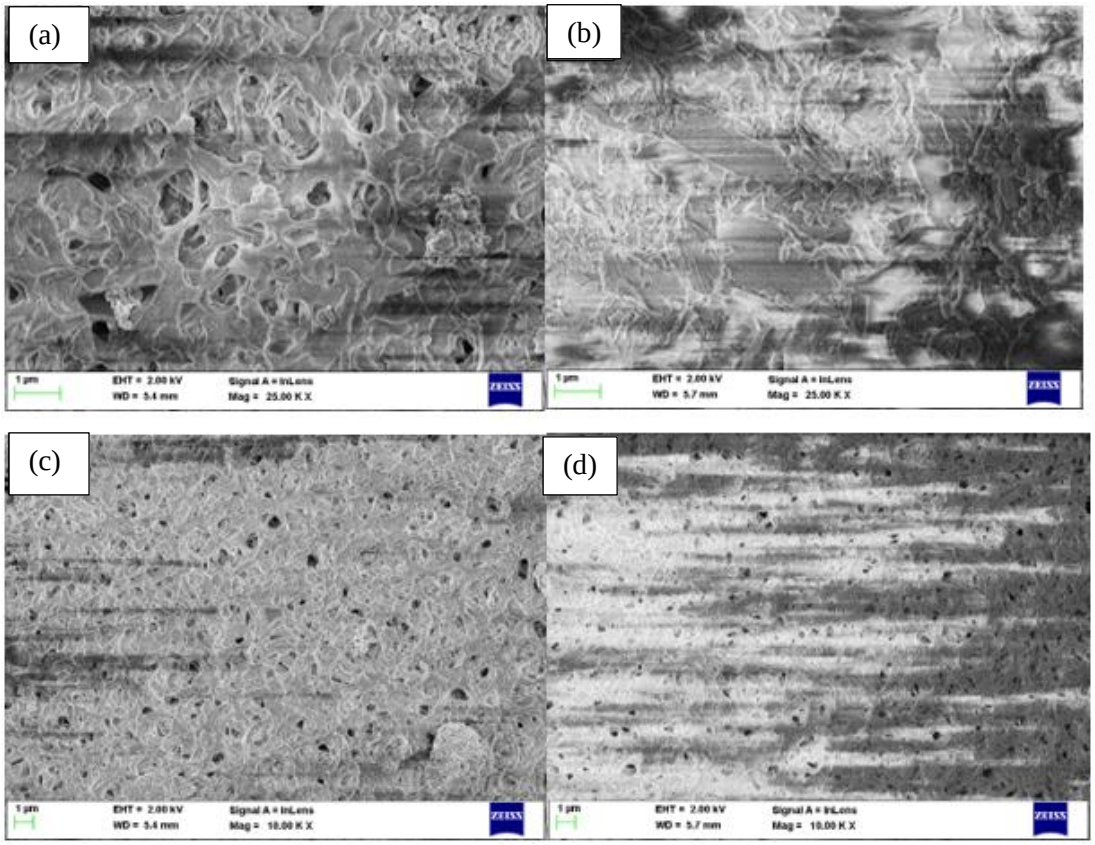

Figure 4.9: SEM magnification images for (a) N-TiO_2-PVDF at x25 magnification, (b) PVDF at x25magnification, (c) N-TiO_2-PVDF at x10 and (d) PVDF at x10 magnification.

PVDF surface images indicated a porous structure with holes. N-TiO_2-PVDF revealed a PVA-coated surface that is spongy with holes. Also, the presence of N-TiO_2 nanoparticles that were non-uniformly dispersed and immobilized was identified. This dispersion could be attributed to non-uniformity in nanoparticles sizes (Sakarkar, Muthukumaran, & Jegatheesan, 2021) as well as the hang drying during its synthesis. The presence of N-TiO_2 nanoparticles and PVA coating is crucial as it contributes to decreasing hydrophobicity by reducing the number of PVDF surface pores and hence reducing the effects of pore capillarity (Gu, et al., 2020). Individually, immobilized N-TiO_2 nanoparticles indicate the ability it imparts on the N-TiO_2-PVDF membranes by generating radicals for photocatalytic reactions whereas the spongy PVA coating

observed indicated its ability to carry out microporous filtration of water containing pollutants simultaneously and with synergy.

EDX test carried out on PVDF and N-TiO_2-PVDF identified its chemical compositions positively as shown in Table 4.2.

Table 4.2: Elemental chemical composition for PVDF and N-TiO_2-PVDF by EDX

Element	**PVDF**		**N-TiO_2-PVDF**	
	Weight%	Atomic%	Weight%	Atomic%
C	43.57	54.63	42.41	53.01
N	**0.00**	**0.00**	**0.01**	**0.01**
O	4.31	4.06	11.39	10.69
F	52.12	41.32	45.76	36.16
S	0.00	0.00	0.00	0.00
Ti	**0.00**	**0.00**	**0.42**	**0.13**
Fe	0.00	0.00	0.00	0.00
Zn	0.00	0.00	0.00	0.00
Totals	**100**	**100**	**100**	**100**

PVDF membrane had carbon and fluorine as the main components, which was expected as the basis of any pristine PVDF membrane. N-TiO_2-PVDF had carbon and fluorine because of the parent PVDF membrane used during synthesis. Of interest is the identification of titanium and nitrogen. This confirmed the presence of immobilized N-TiO_2 nanoparticles. A high increase in oxygen percentage was a clear indication of hydroxyl groups contained PVA polymer used in immobilization (Scorrano, et al., 2015), oxygen groups contained in glutaraldehyde cross-linking as well oxygen bound in immobilized N-TiO_2 nanoparticles.

4.1.2.4 Water contact angle

PVDF and N-TiO_2-PVDF were evaluated for hydrophilicity by investigating the water droplet spreading characteristic over membrane surfaces (Gu, et al., 2020) and the results shown in Figure 4.10.

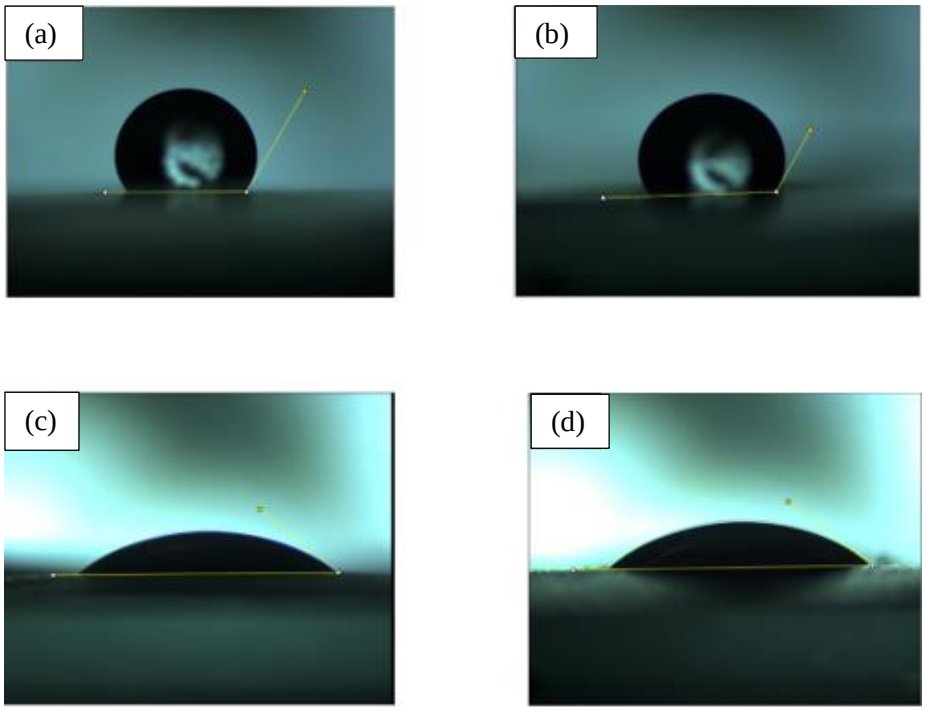

Figure 4.10: Water contact angle for (a)PVDF membrane Front side(120.29º), (b) PVDF membrane back side(119.98º), (c)N-TiO_2-PVDF membrane front side(39.24º) and (d) N-TiO_2-PVDF membrane back side(38.10º).

PVDF had a water contact angles for the front and backside of 120.29º and 119.98º, respectively. N-TiO_2-PVDF had water contact angles for the front and backside of 39.24º and 38.10º, respectively. This indicated N-TiO_2-PVDF had a better wetting ability than pristine PVDF membrane by forming a thicker hydrating layer over the surface (Liu, et al., 2022). This was attributed to the presence of PVA polymer and N-TiO_2 and is crucial in repulsing pollutants during photocatalytic membrane action. PVA had surface hydroxyl functional groups (Li, Chen, Hu, Zhang, & Hu, 2014) and created a coating on PVDF thereby reducing the effects of pore capillarity and hence reducing

the contact angle. N-TiO_2 nanoparticles formed hydrogen bonding with the water molecules increasing its attachment. Additionally, N-TiO_2 nanoparticles reduced the water contact angle by forming hydrophilic hydroxyl radicals with water molecules, further reducing the water contact angle (Liu, et al., 2022). Lower contact angles indicate the ability to repel pollutants and reduce membrane fouling. The pure water flux for PVDF membrane was 802ml/7cmD/hr and 708ml/7cmD/hr for N-TiO_2-PVDF.

4.2 Optimization of Disinfection and Degradation

4.2.1 1st set: Degradation, flux and TOC removal with sulphamethoxazole

4.2.1.1 Modelling and analysis of variance (ANOVA)

The central composite design based on (RSM) gave the information in Table 4.3 in coded and actual values to show the influence of the independent variables, namely; pH (indicated as A) and NaCl concentration (indicated as B) on the 1st,2nd and 3rd responses, namely; degradation in percentage removal of SMX (%), flux in milliliter per 7cm diameter membrane per minute(ml/7cmD/min) and TOC removal percentage of SMX (%) as shown in Table 4.3.

Table 4.3: Factors and all the responses for degradation, flux and TOC removal for 1st set.

Std		Factor1 A : pH (coded)	Factor2 B: NaCl conc g/l	Factor 1 A: pH (Actual)	Factor2 B: NaCl conc g/l	Response 1 Degradation %	Response 2 ml/7cmD/min	Response 3 TOC removal %
4	1	1.000	1.000	10	40	52.26	7.4	40.91
9	2	0.000	0.000	7	23.5	69.87	8.49	58.50
11	3	0.000	0.000	7	23.5	73.14	8.44	57.77
7	4	0.000	-1.414	7	0.165476	73.13	10.28	59.97
6	5	1.414	0.000	11.2426	23.5	53.33	8.66	32.26
13	6	0.000	0.000	7	23.5	73.14	8.51	58.50
8	7	0.000	1.414	7	46.8345	66.6	6.66	46.48
2	8	1.000	-1.000	10	7	56.8	9.9	43.84
5	9	-1.414	0.000	2.75736	23.5	73.14	8.58	25.95
10	10	0.000	0.000	7	23.5	73.12	8.47	49.12
3	11	-1.000	1.000	4	40	69.87	7.64	28.29
1	12	-1.000	-1.000	4	7	76.41	9.85	36.65
12	13	0.000	0.000	7	23.5	69.87	7.91	58.50

The relationship between the independent variables and responses was better fit the 2nd order quadratic polynomial equation for degradation and TOC removal and linear equation for flux as shown in Equations 4.1, 4.2 and 4.3. Where all the equations were not aliased, focusing on the maximization of adjusted and predicted coefficient of variance (adjusted R^2 and predicted R^2).

$$\text{Degradation}(\%) = \gamma_0 + \gamma_1 A + \gamma_2 B + \gamma_3 AB + \gamma_4 A^2 + \gamma_5 B^2 \quad \text{Equation 4.1}$$

$$\text{Flux}(\text{ml}/7\text{cmD}/\text{min}) = \beta_0 + \beta_1 A + \beta_2 B \quad \text{Equation 4.2}$$

$$\text{TOC removal}(\%) = \alpha_0 + \alpha_1 A + \alpha_2 B + \alpha_3 AB + \alpha_4 A^2 + \alpha_5 B^2 \quad \text{Equation 3}$$

Where γ_i, β_i and α_i are the coefficients for A and B independent variables with respective equations for each response.

The analysis of variance (ANOVA) was conducted to justify the model's significance and adequacy for the Degradation response, flux response and TOC removal response. It also justified the effects of the significance of independent variables. The coefficients for Equations 4.1, 4.2 and 4.3 can be obtained from Table 4.4 -4.6 below.

Table 4.4: Degradation coefficients for 1st set.

Factor	**Coefficient estimate**	**df**	**Standard error**	**95%CI low**	**95%CI high**	**VIF**
Intercept	71.83	1	1.07	69.31	74.35	
A-pH	-8.12	1	0.8425	-10.11	-6.13	1.0000
B-NaCl	-2.54	1	0.8425	-4.53	-0.5472	1.0000
AB	0.5000	1	1.19	-2.32	3.32	1.0000
A^2	-4.94	1	0.9035	-7.07	-2.80	1.02
B^2	-1.67	1	0.9035	-3.81	0.4636	1.02

Table 4.5: Flux coefficients for 1st set

Factor	Coefficient estimate	df	Standard error	95%CI low	95%CI high	VIF
Intercept	8.52	1	0.00673	8.37	8.67	
A-pH	-0.0084	1	0.0859	-0.1997	0.1829	1.0000
B-NaCl	-1.23	1	0.0859	-1.42	-1.04	1.0000

Table 4.6: TOC removal coefficients for 1st set

Factor	Coefficient estimate	df	Standard error	95%CI low	95%CI high	VIF
Intercept	56.48	1	1.84	52.13	60.83	
A-pH	3.59	1	1.45	0.1522	7.03	1.0000
B-NaCl	-3.80	1	1.45	-7.24	-0.3565	1.0000
AB	1.36	1	2.06	-3.51	6.22	1.0000
A^2	-14.62	1	1.56	-18.31	-10.93	1.02
B^2	-2.56	1	1.56	-6.25	1.13	1.02

Important to note is that the synergistic effects on the model by the terms are indicated with a positive sign, whereas the antagonistic effect on the model by the terms that are indicated with a negative sign (Rani & Karthikeyan, 2018), (Hasanpour, Motahari, Jing, & Hatami, 2021). The coefficient estimates represented the expected change in responses per unit change in factor value when all remaining factors were held constant. The intercepts in an orthogonal design were the overall average responses for all the runs. The coefficients were adjusted around that average based on the factor setting. When factors are orthogonal, the VIFs (Variance Inflation Factors) are 1. VIFs greater than 1 indicated multicollinearity, the higher the VIF the more severe the correlation of factors. VIFs less than 10 are tolerable.

All three models were significant with F values (Fisher variation ratio) of 26.67 for degradation, 102.62 for flux and 20.28 for TOC removal. Additionally, all the models had P values (probability value) of 0.0002 for degradation, <0.0001 for flux and 0.0005 for TOC removal. The results are shown in Table 4.7 - 4.9.

Table 4.7: showing F-values, p-values and its significance for response 1 degradation model for 1st set.

Source	**Sum of squares**	**df**	**Mean Square**	**F-value**	**p-value**	
Model	757.04	5	151.41	26.67	0.0002	significant
A-pH	527.36	1	527.36	92.88	<0.0001	
B-NaCl conc	51.59	1	51.59	9.09	0.0195	
AB	1.0000	1	1.0000	0.1761	0.6873	
A^2	169.61	1	169.61	29.87	0.0009	
B^2	19.46	1	19.46	3.43	0.1065	
Residual	39.75	7	5.68			
Lack of fit	26.97	3	8.99	2.81	0.1716	Not significant
Pure error	12.78	4	3.19			
Cor total	796.79	12				

Table 4.8: F-values, p-values and its significance for response 2 flux for 1st set.

Source	**Sum of squares**	**df**	**Mean Square**	**F-value**	**p-value**	
Model	12.10	2	6.05	102.62	<0.0001	significant
A-pH	0.0006	1	0.0006	0.0095	0.9244	
B-NaCl conc	12.10	1	12.10	205.23	<0.0001	
Residual	0.5897	10	0.0590			
Lack of fit	0.3293	6	0.0549	0.8434	0.5950	Not significant
Pure error	0.2603	4	0.0651			
Cor total	12.69	12				

Table 4.9: F-values, p-values and its significance for response 3 TOC removal for 1st set.

Source	Sum of squares	df	Mean Square	F-value	p-value	
Model	1716.23	5	343.25	20.28	0.0005	significant
A-pH	103.20	1	103.20	6.10	0.0429	
B-NaCl conc	115.27	1	115.27	6.81	0.0349	
AB	7.37	1	7.37	0.4355	0.5304	
A^2	1487.35	1	1487.35	87.87	<0.0001	
B^2	45.67	1	45.67	2.70	0.1445	
Residual	118.48	7	16.93			
Lack of fit	5041	3	16.80	0.9873	0.4833	Not significant
Pure error	68.07	4	17.02			
Cor total	1834.72	12				

This indicated that there were 0.02%,0.01% and 0.05% for chances that f-values this large could occur due to noise for Degradation, flux and TOC removal responses, respectively. From table 4.7-4.9, the lack of fit F value of 2.81 for degradation,0.84 for flux and 0.99 for TOC removal implied that the lack of fit was not significant relative to the pure error and that there was 17.23% ,59.5% and 48.33% chance that lack of fit of F value this large could occur due to noise, respectively. Non-significant lack of fit was good and the models fitted well. The predicted R^2 of 0.7343, 0.9290 and 0.7467 for degradation, flux and TOC removal was in reasonable agreement with the adjusted R^2 of 0.9145, 0.9442 and 0.8893 respectively, since the difference in predicted and adjusted R^2 did not exceed 0.2. This meant that variation in all the responses were adequately accounted for (Zarei & Behnajady, 2019). The C.V% (coefficient of variation) value for degradation was 3.52%, 2.85% for flux and 8.96% for TOC

removal. All the values were below the 10% threshold. This indicated the models' high reliability and accuracy (Zhang & Zhao, 2019). The adeq precision (adequacy precision) that measures signal-to-noise ratio was 16.003, 29.822 and 12.368 for degradation, flux and TOC removal respectively and were all above 4. This showed an adequate signal of the models and can hence be used to navigate the design space.

Furthermore, the normal plot of residual analysis (normal %probability vs externally studentized residuals) for degradation, flux and TOC removal respectively showed experimental data residual points close to the predicted straight line as shown in Figure 4.11 - 4.13.

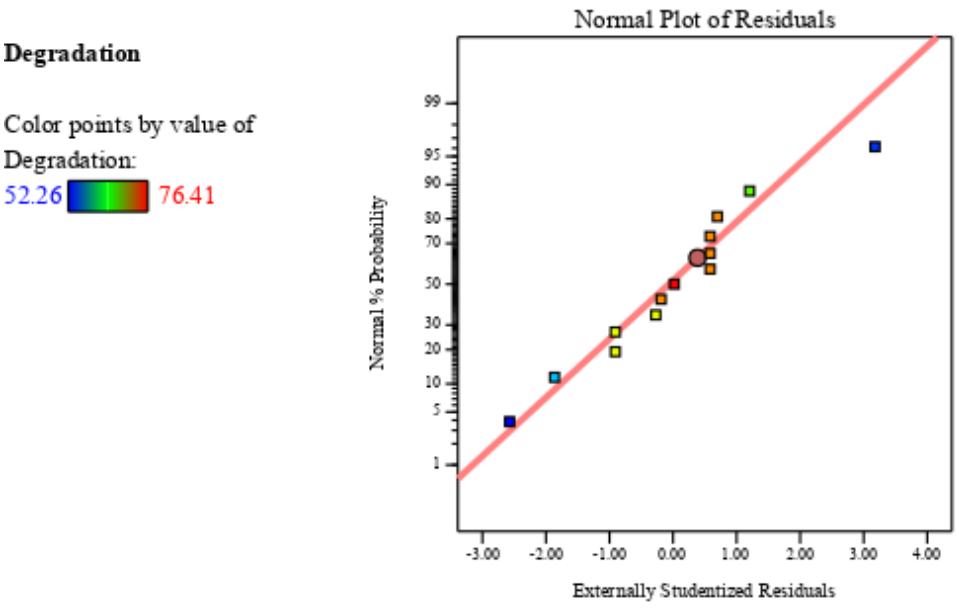

Figure 4.11: Normal plot of residual analysis (normal %probability vs externally studentized residuals) for degradation for 1st set.

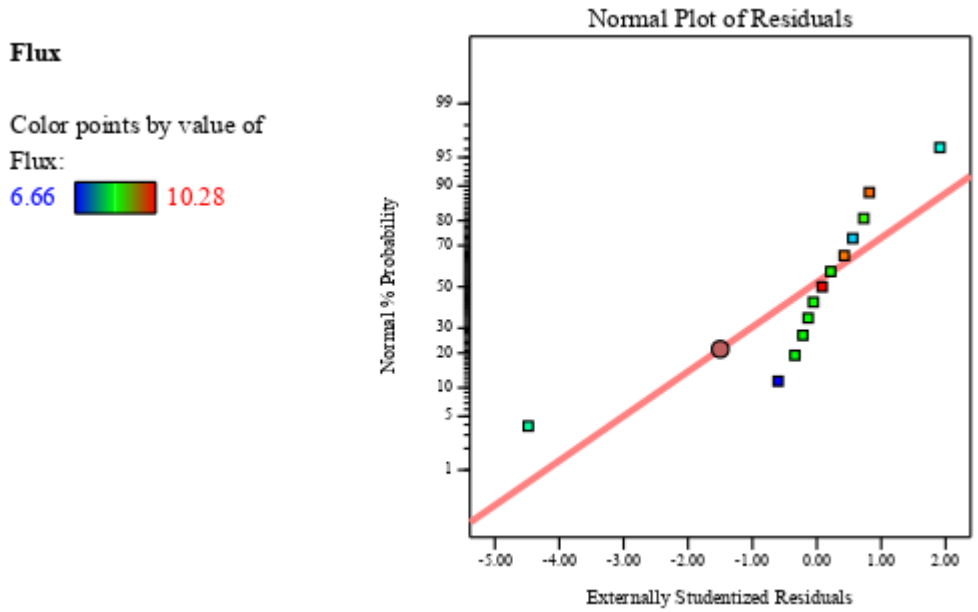

Figure 4.12: Normal plot of residual analysis (normal %probability vs externally studentized residuals) for flux for 1st set.

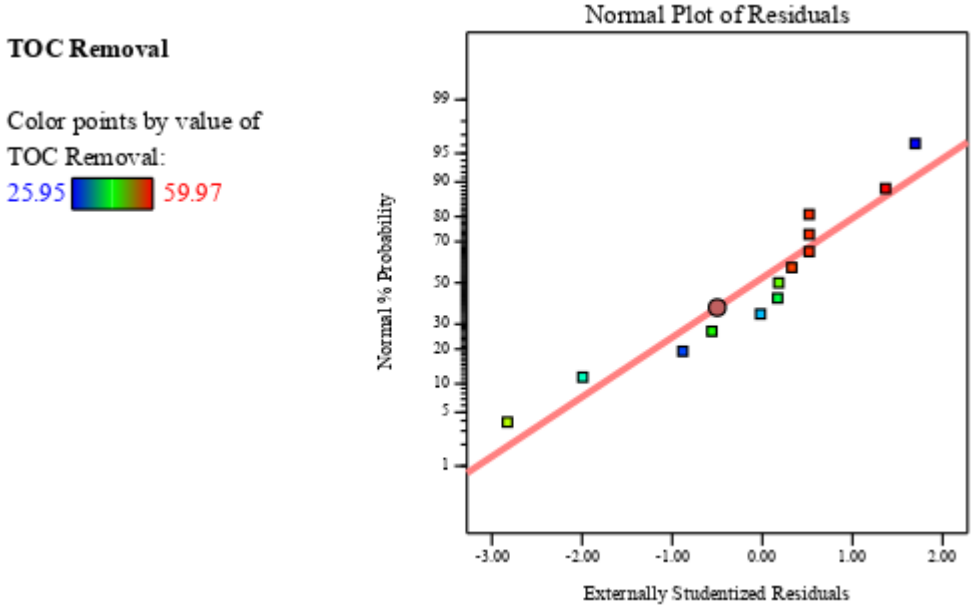

Figure 4.13: showing the normal plot of residual analysis (normal %probability vs externally studentized residuals) for TOC removal for 1st set.

This indicated low scattering and discrepancies for normal distribution and hence can be able to effectively study degradation, flux and TOC removal processes (Zarei & Behnajady, 2019). A plot of externally studentized residual vs predicted, residual vs run for degradation, flux and TOC removal showed scattering that was near zero and

was random with a change value of 4.56117 for degradation, 3.86016 for flux and 4.56117 for TOC removal as shown if figure 4.14, 4.15, 4.16 and 4.17.

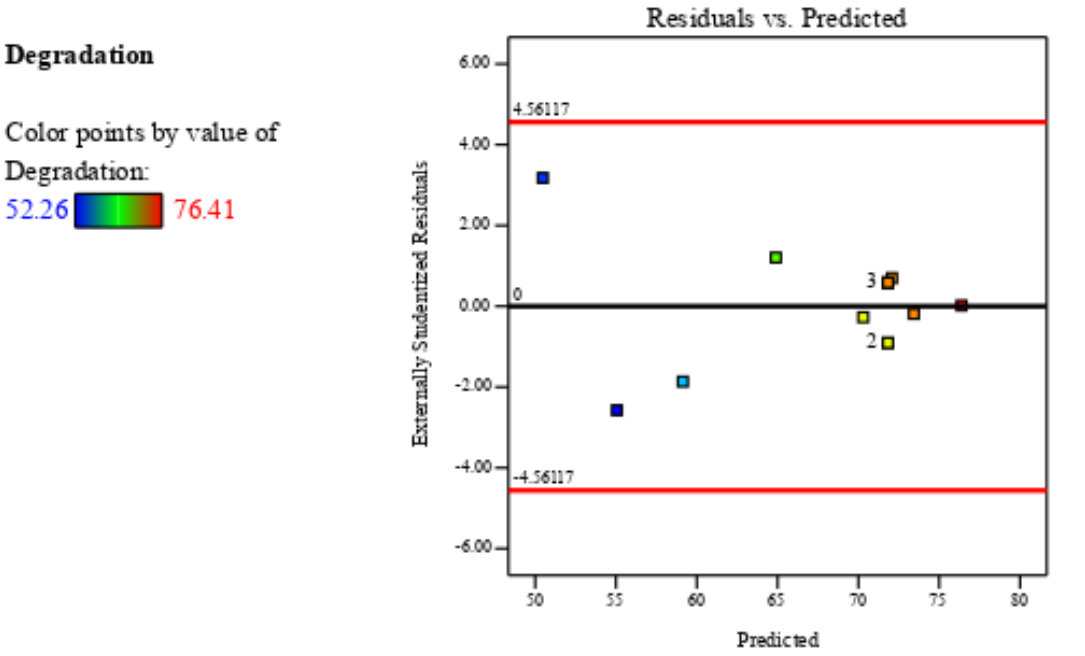

Figure 4.14: A plot of externally studentized residual vs predicted for degradation.

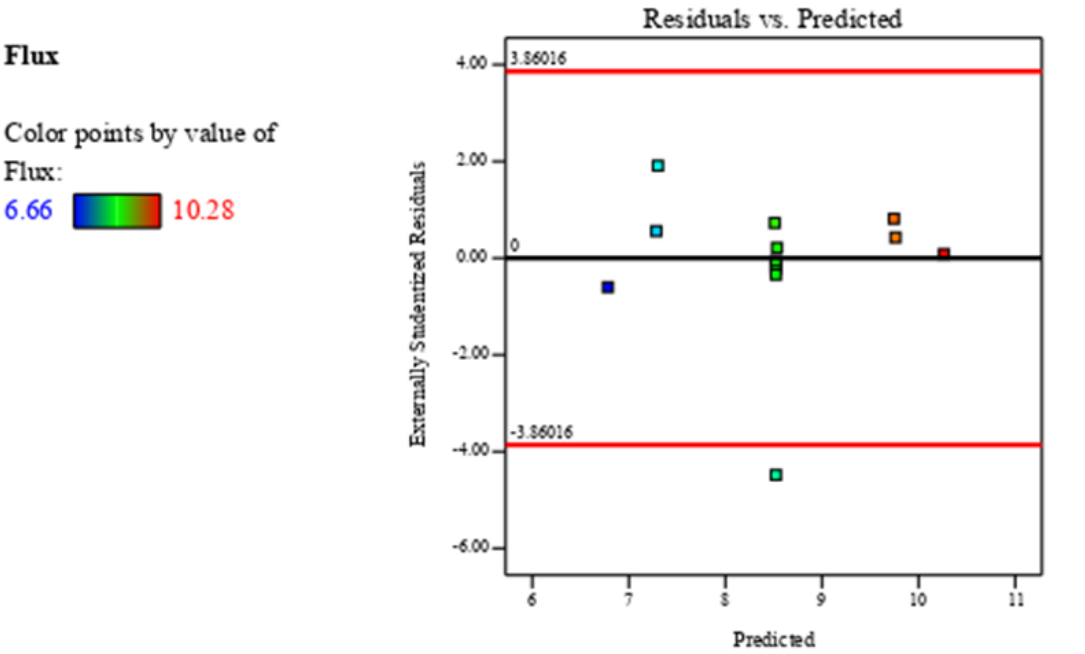

Figure 4.15: A plot of externally studentized residual vs predicted for flux.

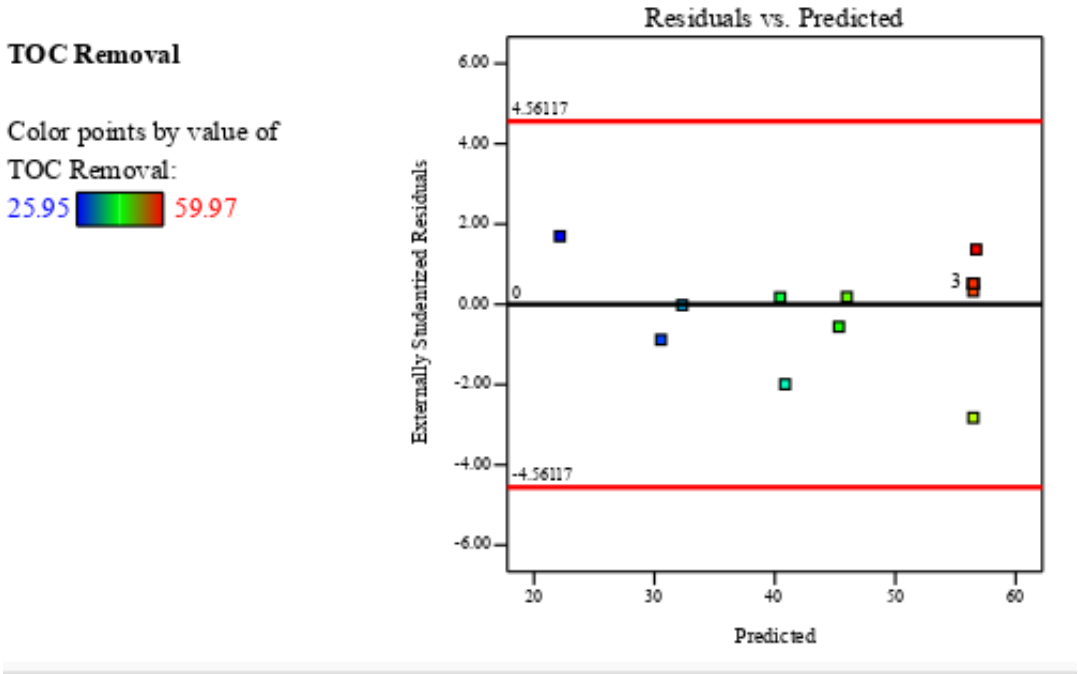

Figure 4.16: A plot of externally studentized residual vs predicted for TOC removal.

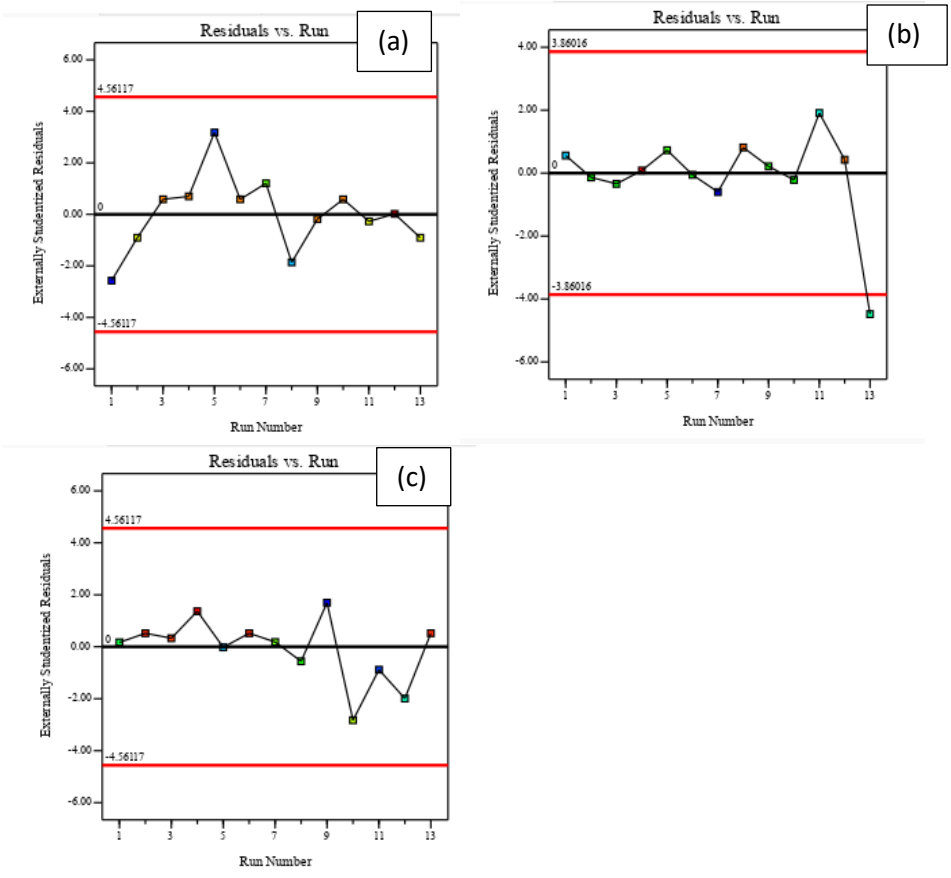

Figure 4.17: A plot of residual vs run for degradation for 1st set for (a)degradation, (b) flux and (c) TOC removal

This validated that the data was normally dispersed in model responses (Song, et al., 2020).

4.2.1.2 3D response surfaces

The magnified or suppressed effect due to interactions of independent variables of pH and NaCl concentrations on the responses of degradation, flux and TOC removal can visually be displayed by 3D response surface plot (Esfahani, Firouzi, Sayyad, & Kiasat, 2013).

The SMX degradation increased with decreased pH and NaCl concentration as shown in degradation 3D diagram Figure 4.18.

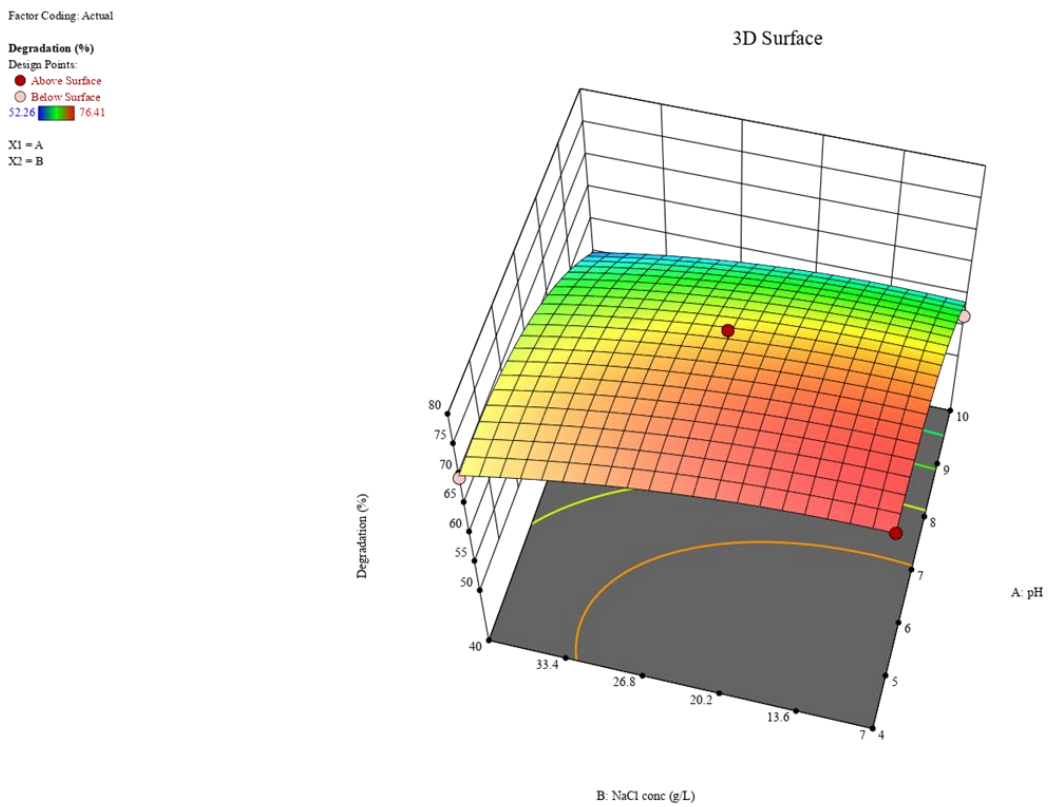

Figure 4.18: 3D diagram showing combined effect of pH and NaCl concentration on degradation for 1st set.

At acidic conditions and pH less than the Photocatalyst point of zero charge of 6.4 (Thuy, et al., 2020), the immobilized N-TiO_2 develops a positively charged surface,

whereas for SMX is still negatively charged. This then exerted an electrostatic force and created polar attraction and promoted subsequent adsorption of SMX onto N-TiO_2 charged surface. This resulted to higher interactions and hence increased degradation. Close to neutrality, i.e. pH 7, the N-TiO_2 is nearly neutral, but the SMX is still negatively charged. The absence of opposite charged particles lowers electrostatic force, lowers polar attraction and results in reduced degradation due to less interactions between N-TiO_2 and SMX. With increased alkalinity, the N-TiO_2 and SMX became negatively charged as well. This exerted repulsive forces between them, further hindering interactions and, hence decreasing degradation. The degradation of SMX was suppressed due to the increasing concentration of NaCl. This can be attributed to Cl- anion that inhibited the formation of $OH^{\cdot}$ radicals by displacing OH- anions through preferred adsorption on N-TiO_2 surface (Wu, Kuo, Dong, Chen, & Lin, 2019). This reduced the number of OH- readily available to photocatalyst to generate hydroxyl radicals, decreasing degradation. The presence of increasing chloride anions (due to membrane filtration) increases charges recombination and increased its reactions with photogenerated $OH^{\cdot}$ radicals, further consuming OH radicals that would have been utilized to degrade pollutants (Chong, Jin, Chow, & Saint, 2010). This further reduced degradation with increased NaCl concentration. This resulted in chloride radicals that are less reactive to OH radicals, reducing degradations. This is illustrated in Equations 4.4 and 4.5 (Liao, Kang, & Wu, 2001).

$HO^{\cdot} + Cl^{-} + HOCl^{\cdot}$ Equation 4.4

$HOCl + h^{+} \rightarrow Cl^{\cdot} + H_2O$ Equation 4.5

Additionally, Cl- anion scavenges photogenerated holes directly and results in chloride radicals that are not as active in photodegradation as $OH^{\cdot}$ radicals, as shown in equation

4.5 (Álvarez, Orellana-García, López-Ramón, Rivera-Utrilla, & Sánchez-Polo, 2018). This further reduced the degradation of SMX as shown in Equation 4.6.

$h^+ + Cl^- \rightarrow Cl\cdot$ Equation 4.6

The flux of N-TiO_2-PVDF membrane reduced with increasing presence of NaCl and pH due to SMX reducing degradations as shown in 3D diagram Figure 4.19.

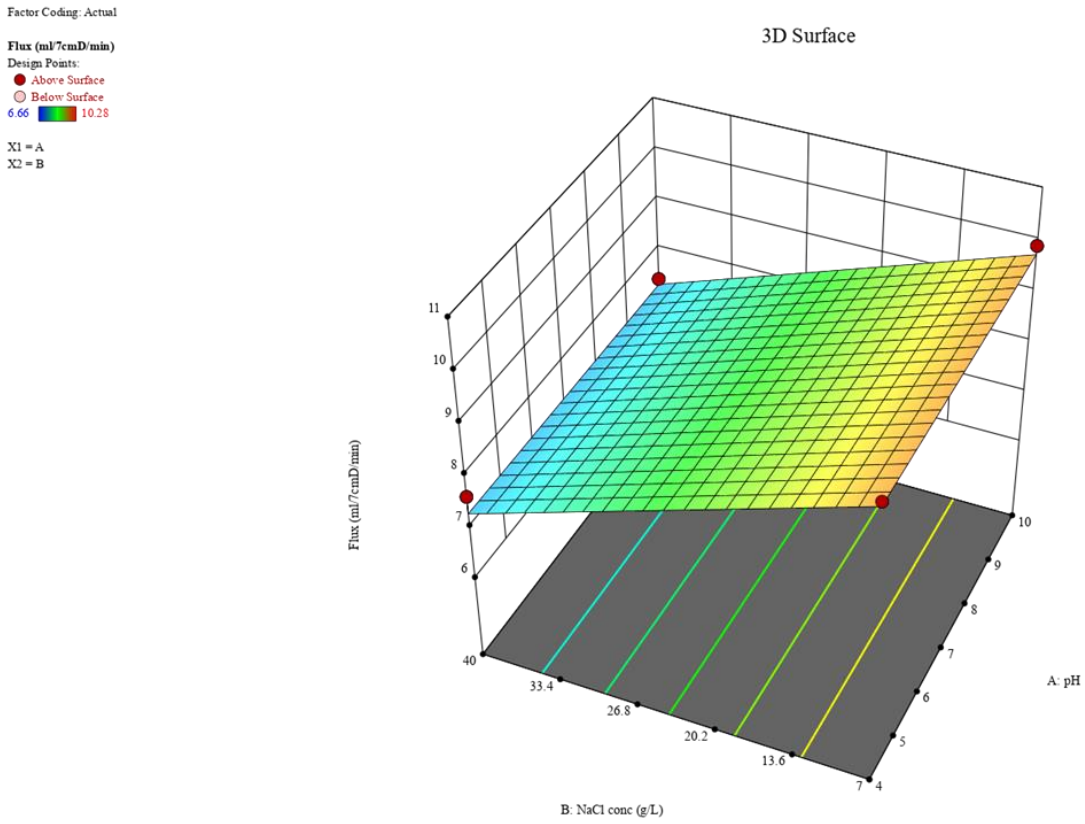

Figure 4.19: 3D diagram showing combined effect of pH and NaCl concentration on flux for 1st set.

Increasing NaCl concentrations increased concentration polarization and crystallization along N-TiO_2-PVDF surface and pores. This effect increased as well, as experimental run proceeded due to filtration increasing NaCl concentration continuously. This reduced the movement of water across the surface of N-TiO_2-PVDF membrane and hence reduced flux. Additionally, increasing NaCl concentration reduced SMX

degradation further increasing SMX foulants deposition on the membrane pores. This increased fouling of the membrane and reduced flux.

Increasing pH effect cannot be ignored as increasing the pH contributed to flux reduction through increased SMX foulants in N-TiO_2-PVDF pores. As pH increased it reduced SMX pollutant degradation and increased fouling. Among the two variables, NaCl highly affected flux more that pH due to smaller concentration of SMX as compared to NaCl concentration.

Radicals in photodegradation are usually unselective and hence the importance of TOC studies. SMX is degraded through different pathways that yield different intermediates, mainly such as 5-amino-3-methylisoxazole, nitrosobenzene, 4-aminobenzenesulfonic acid, 4-nitrosulfamethoxazole and nitrophenols etc. (Shang, et al., 2022), that also further consume radicals to undergo further degradation to inorganic acids, salts, carbon dioxide and water. The highest TOC removal was attained at a close pH of 7 as shown in 3D diagram Figure 4.20.

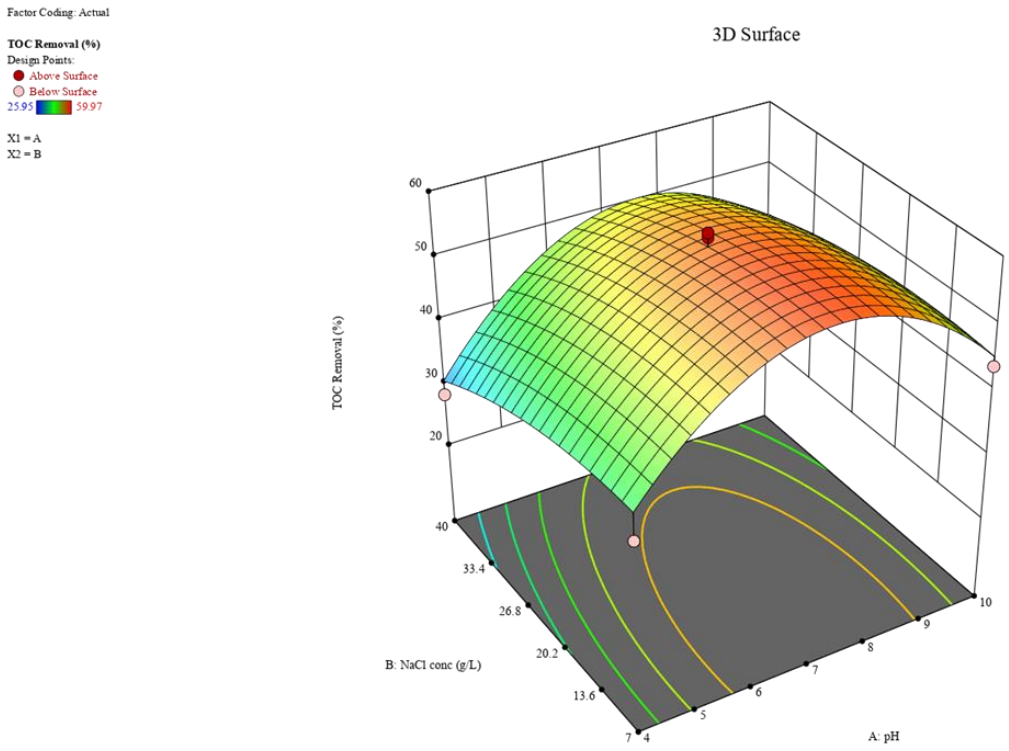

Figure 4.20: 3D diagram showing combined effect of pH and NaCl concentration on TOC removal for 1st set.

This was attributed to points of zero charge of N-TiO_2 and most of intermediates of SMX degradation that fall close to pH 7. This lack of charged surfaces between them allowed free interaction between them and resulted to increased TOC removal. At increased acidity or alkalinity, N-TiO_2 and most intermediates had similar surface charges. This resulted to electrostatic repulsions, suppressing free interaction between N-TiO_2 and SMX Intermediates and hence reduced TOC removal. Presence increasing of Cl^- (from NaCl) also played a role in suppressing formation of hydroxyl radical similarly to the discussed earlier mechanism for degradation. This limited the amount of hydroxyl radical for degradation of intermediates hence reducing TOC removal with increasing NaCl concentrations.

4.2.1.3 Numerical optimization functions

The numerical optimization function was used to determine the optimal values by maximizing degradation, flux and TOC removal responses and getting the corresponding independent variable values that give the maximum values of the responses. The goals of the responses were selected to be maximized at their desirability, whereas the independent variables of pH and NaCl concentration were set to be within the range. The weights and importance function increased or decreased the emphasis of limit and ranges to the responses (Vaez, Moghaddam, & Alijani, 2012). Importance of 5 ratings was selected for degradation and flux, whereas importance rating of 3 was chosen for TOC removal. From the numerical optimization function,(1)maximum degradation of 76.5% for SMX would be attained by a combination of 7.8 g/L of NaCl and a pH of 4.6, (2) maximum flux of 9.8 ml/7cmD/min when degrading SMX would be attained by a combination of 7 g/L of NaCl and a pH of 4, and (3)maximum TOC removal 58% for SMX would be attained by a combination of 11.7 g/L of NaCl and a pH of 7.3 as shown in Figure 4.21 - 4.23.

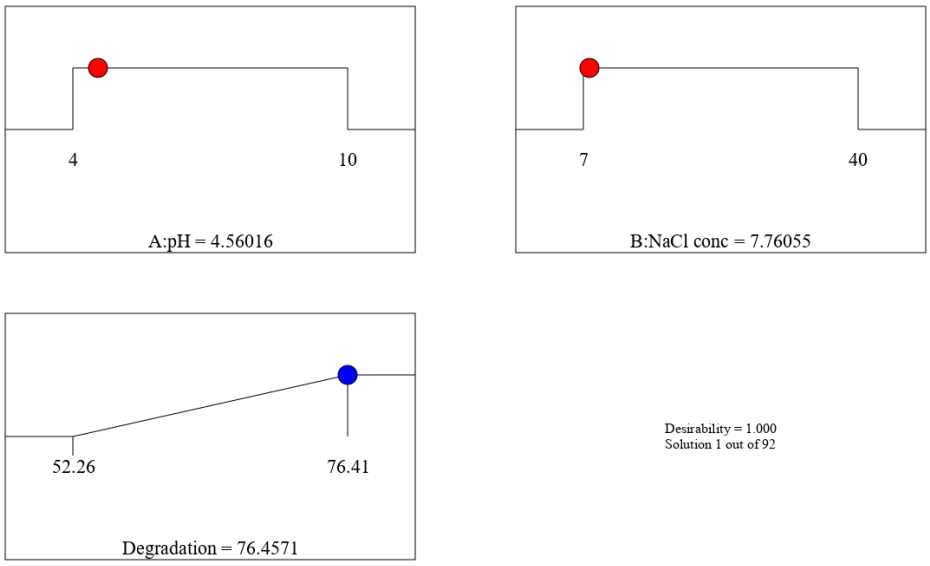

Figure 4.21: Optimum value for degradation and variables required for optimum degradation for 1st set.

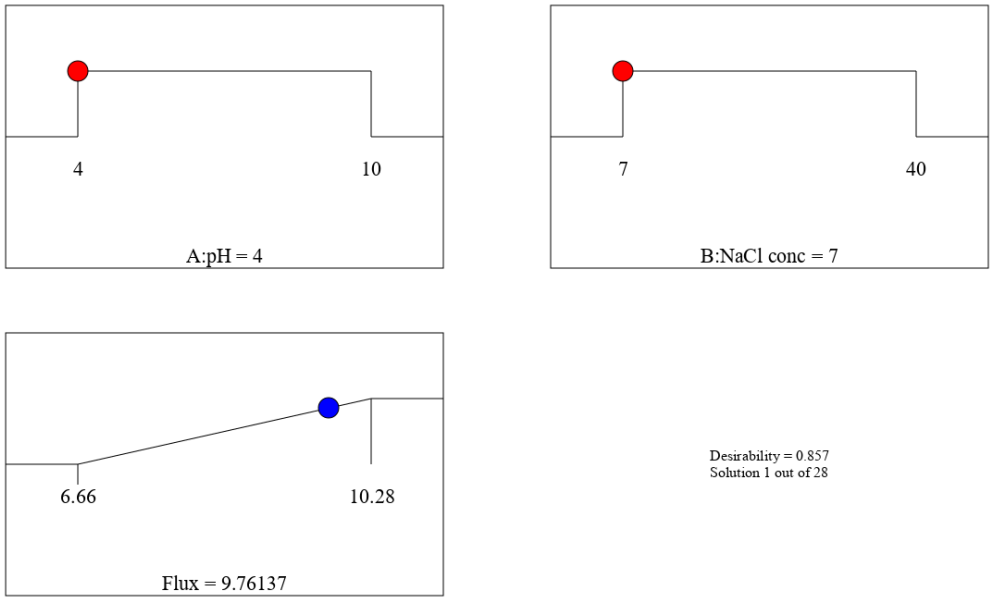

Figure 4.22: Optimum value for flux and variables required for optimum flux for 1st set

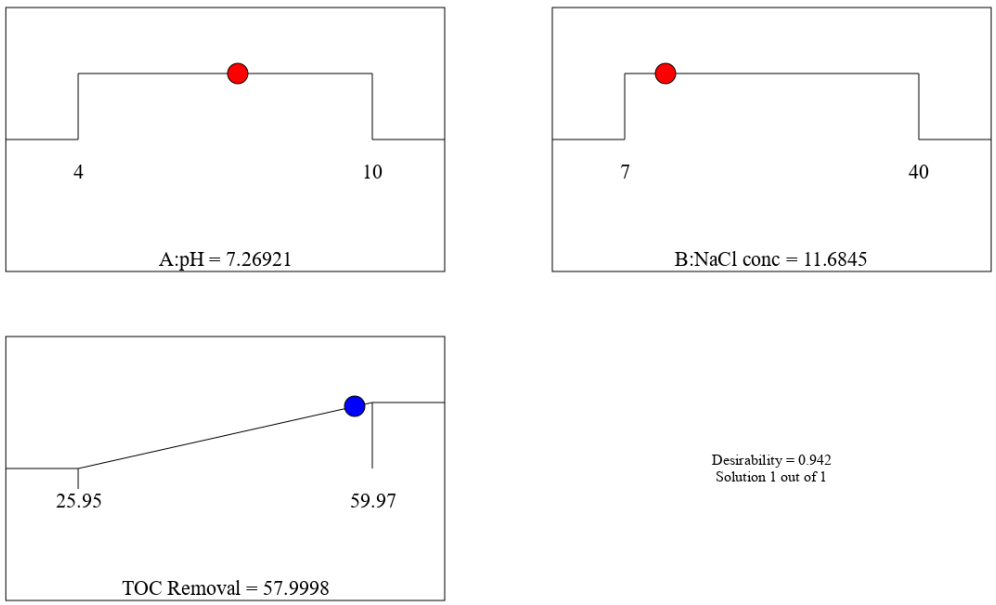

Figure 4.23: Optimum value for TOC removal and variables required for optimum TOC removal for 1st set.

The degradation response optimum value was selected out of 92 solutions to give 76.5% at a pH of 4.6 and NaCl concentration of 7.8 g/l at a desirable value of 100%. Flux response optimum values was selected out of 28 solutions to give 9.8 ml/7cmD/min at a pH of 4 and NaCl concentration of 7 g/l at a desirable value of 85.7%. TOC removal

response optimum value was selected out of 1 possible solution to a TOC removal of 58% at a pH of 7.3 and NaCl concentration of 11.7 g/l at a desirability of 94.2%.

4.2.3 2nd set: Disinfection and flux

4.2.3.1 Modelling and analysis of variance (ANOVA)

The central composite design based on (RSM) gave the information in Table 4.10 in coded and actual values to show the influence of the independent variables, namely; pH (indicated as A) and NaCl concentration (indicated as B) on the 1st and 2nd responses, namely; disinfection in percentage removal of *E.coli* (%) and flux in milliliter per 7cm diameter membrane per minute (ml/7cmD/min) as shown in Table 4.10.

Table 4.10: Factors and all the responses for disinfection and flux for 2nd set.

std	run	Factor 1 A:pH(coded)	Factor 2 B:NaCl conc(coded)	Factor 1 A:pH(Actual)	Factor 2 B:NaCl conc(Actual)	Response 1 Disinfection(%)	Response 2 Flux(ml/7cmD/min)
8	1	0.000	1.414	7	46.8345	100	3.8
12	2	0.000	0.000	7	23.5	100	4.61
1	3	-1.000	-1.000	4	7	100	5
2	4	1.000	-1.000	10	7	100	4.93
11	5	0.000	0.000	7	23.5	100	4.65
13	6	0.000	0.000	7	23.5	100	4.58
5	7	-1.414	0.000	2.75736	23.5	100	4.2
7	8	0.000	-1.414	7	0.165476	100	5.7
3	9	-1.000	1.000	4	40	100	3.67
6	10	1.414	0.000	11.2426	23.5	100	4
10	11	0.000	0.000	7	23.5	100	4.56
4	12	1.000	1.000	10	40	100	3.25
9	13	0.000	0.000	7	23.5	100	4.4

The relationship between the independent variables and responses could not fit any polynomial disinfection equation as *E.coli* was not detected in the permeate in any of the runs resulting in 100% *E.coli* elimination. The independent variables and flux response were fit to 2nd order quadratic polynomial equation 4.7. Where the equation was not aliased and by focusing on the maximization of the adjusted and predicted coefficient of variance (adjusted R^2 and predicted R^2).

$$\text{Flux}(\text{ml}/7\text{cmD}/\text{min}) = \theta_0 + \theta_1 A + \theta_2 B + \theta_3 AB + \theta_4 A^2 + \theta_5 B^2 \quad \text{Equation 4.7}$$

Where θ_i are coefficients for A and B independent variables with respective equations for flux response. The analysis of variance (ANOVA) was conducted to justify the model's significance and its adequacy for flux response. It justified also for the effects of the significance of independent variables. The coefficients for equation can be obtained from Table 4.11 below. The coefficients estimates represented the expected change in responses per unit change in factor value, when all remaining factors were held constant. The intercepts in an orthogonal design was the overall average response for all the runs. The coefficients were adjusted around that average based on the factor setting. When factors are orthogonal, the VIFs are 1. VIFs greater than 1 indicated multicollinearity, the higher the VIF the more severe the correlation of factors. VIFs less than 10 are tolerable. The results are shown in Table 4.11.

Table 4.11: Flux coefficient for 2nd set

Factor	**Coefficient estimate**	**df**	**Standard error**	**95%CI low**	**95%CI high**	**VIF**
Intercept	4.56	1	0.0644	4.41	4.71	
A-pH	-0.0966	1	0.0509	-0.2171	0.0239	1.0000
B-NaCl	-0.7121	1	0.0509	-0.8326	-0.5917	1.0000
AB	-0.0875	1	0.0720	-0.2578	0.0828	1.0000
A^2	-0.2831	1	0.0546	-0.4123	-0.1540	1.02
B^2	0.0419	1	0.0546	-0.0873	0.1710	1.02

The flux model was significant, with an F value of 45.90 for flux. Additionally, the model had p value of <0.0001. This indicated a 10.84% chance that f-values this large could occur due to noise. non-significant lack of fit was good and the model fitted well as shown in Table 4.12.

Table 4.12: F-values, p-values and its significance for response 2 flux for 2nd set

Source	Sum of squares	df	Mean Square	F-value	p-value	
Model	4.76	5	0.9528	45.90	<0.0001	Significant
A-pH	0.0747	1	0.0747	3.60	0.0997	
B-NaCl conc	4.06	1	4.06	195.43	<0.0001	
AB	0.0306	1	0.0306	1.48	0.2639	
A^2	0.5576	1	0.5576	26.86	0.0013	
B^2	0.0122	1	0.0122	0.5876	0.4684	
Residual	0.1453	7	0.0208			
Lack of fit	0.1087	3	0.0362	3.96	0.1084	Not significant
Pure error	0.0366	4	0.0091			
Cor total	4.91	12				

The predicted R^2 of 0.8309 was in reasonable agreement with the adjusted R^2 of 0.9493 since the difference in predicted and adjusted R^2 did not exceed 0.2. This meant that variation in all the responses were adequately accounted for (Zarei & Behnajady, 2019). The C.V% (coefficient of variation) value was 3.27%. The value was below 10% threshold. This indicated that the model had high reliability and accuracy (Zhang & Zhao, 2019).The adeq precision that measures signal to noise ratio was 22.7649 and was above 4. This shows an adequate signal of the model and can be used to navigate the design space. The normal plot of residual analysis (normal %probability vs

externally studentized residuals) showed experimental data residual points close to the predicted straight line as shown in Figure 4.24.

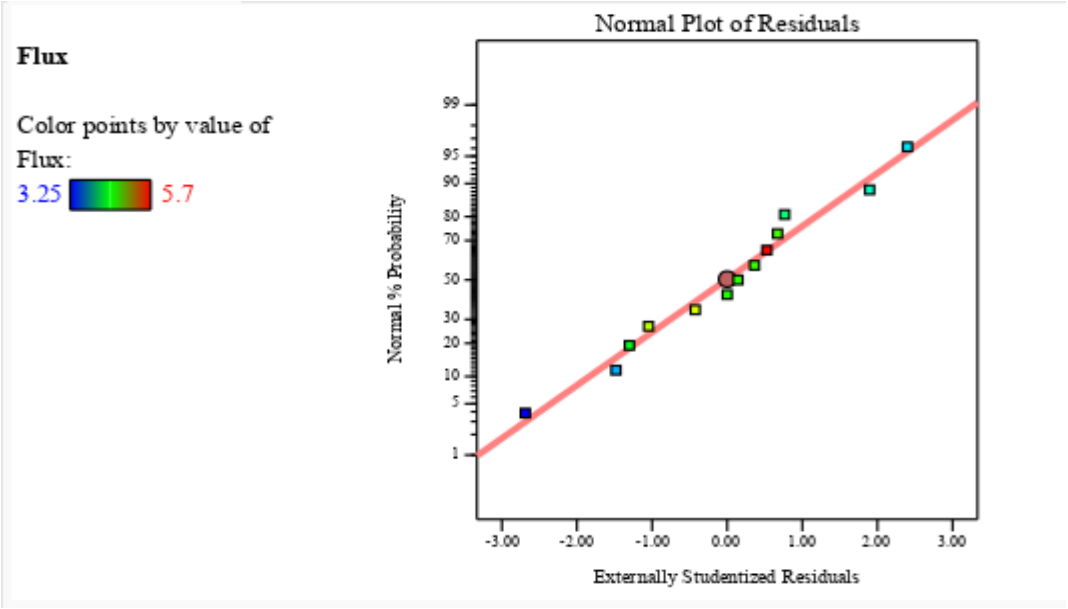

Figure 4.24: Normal plot of residual analysis (normal %probability vs externally studentized residuals) for flux.

This indicated low scattering and discrepancies for a normal distribution and hence can be able to effectively study flux process (Zarei & Behnajady, 2019).A plot of externally studentized residual vs predicted, residual vs run showed scattering near zero and was random with a change value of 4.56117 as shown in Figure 4.25 and 4.26.

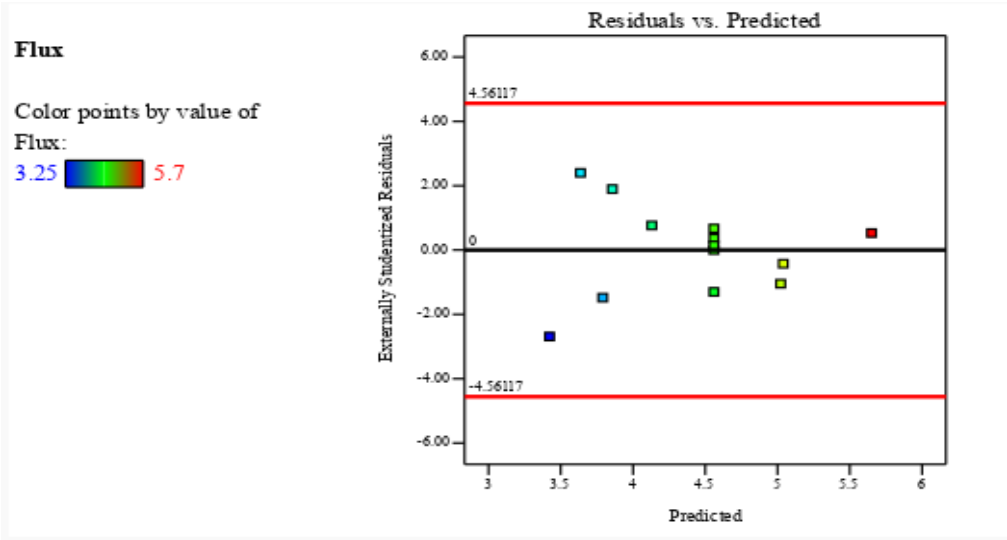

Figure 4.25: Plot of externally studentized residual vs predicted for flux.

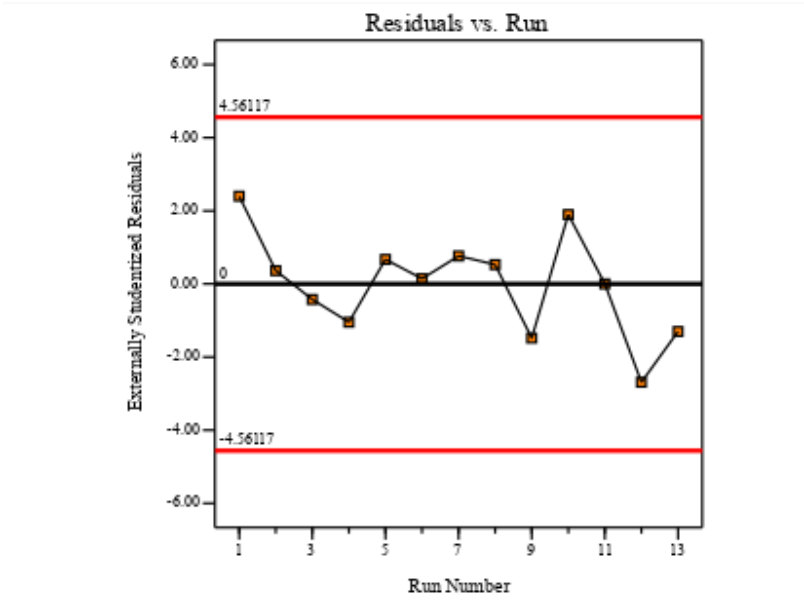

Figure 4.26: Plot of residual vs run for degradation for 2nd set for flux

This validated that the data was normally dispersed in model responses (Song, et al., 2020).

4.2.3.2 3D response surfaces

The disinfection of *E.coli* in the permeate did not vary as per pH and NaCl concentration as shown in Figure 4.27.

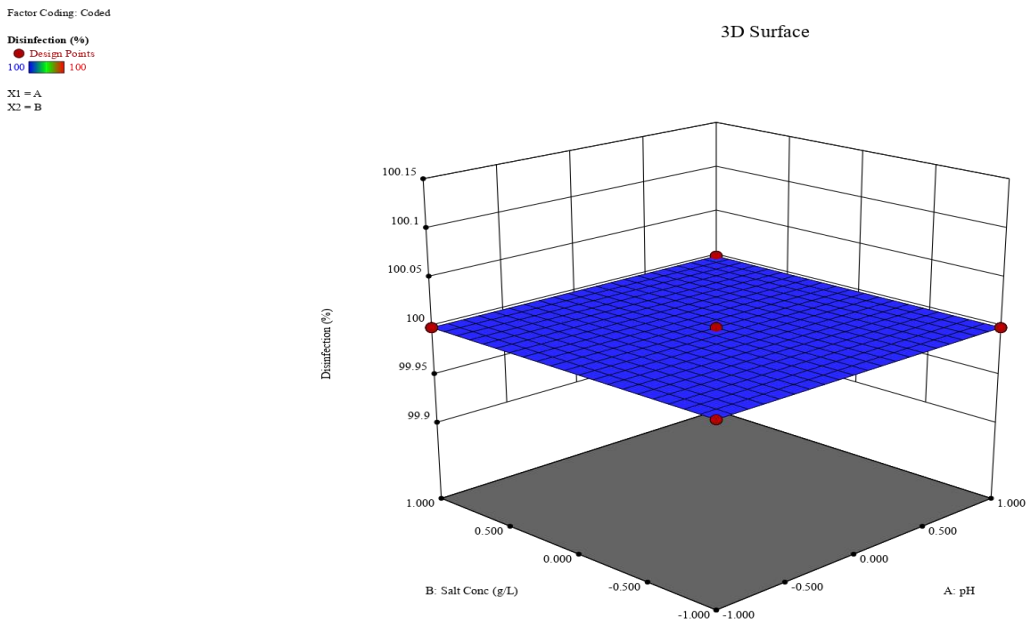

Figure 4.27: 3D diagram showing combined effect of pH and NaCl concentration on disinfection for 2nd set.

This was because the primary mechanism of *E.coli* elimination in the permeate was attributed to the size exclusion mechanism by the N-TiO_2-PVDF. This scenario can be explained further by *E.coli* being a bacterium that is rod-shaped having dimensions of 1.5µm length and 0.5µm wide whereas the PVDF membrane used to synthesize the N-TiO_2-PVDF membrane has a pore size rating of 0.22µm and hindered all the *E.coli* bacteria from crossing over the membrane to the permeate. *E.coli* regrowth test done on the control and permeate samples collected confirmed the negative presence of *E.coli* in the permeate after regrowth as shown by Figure 4.28.

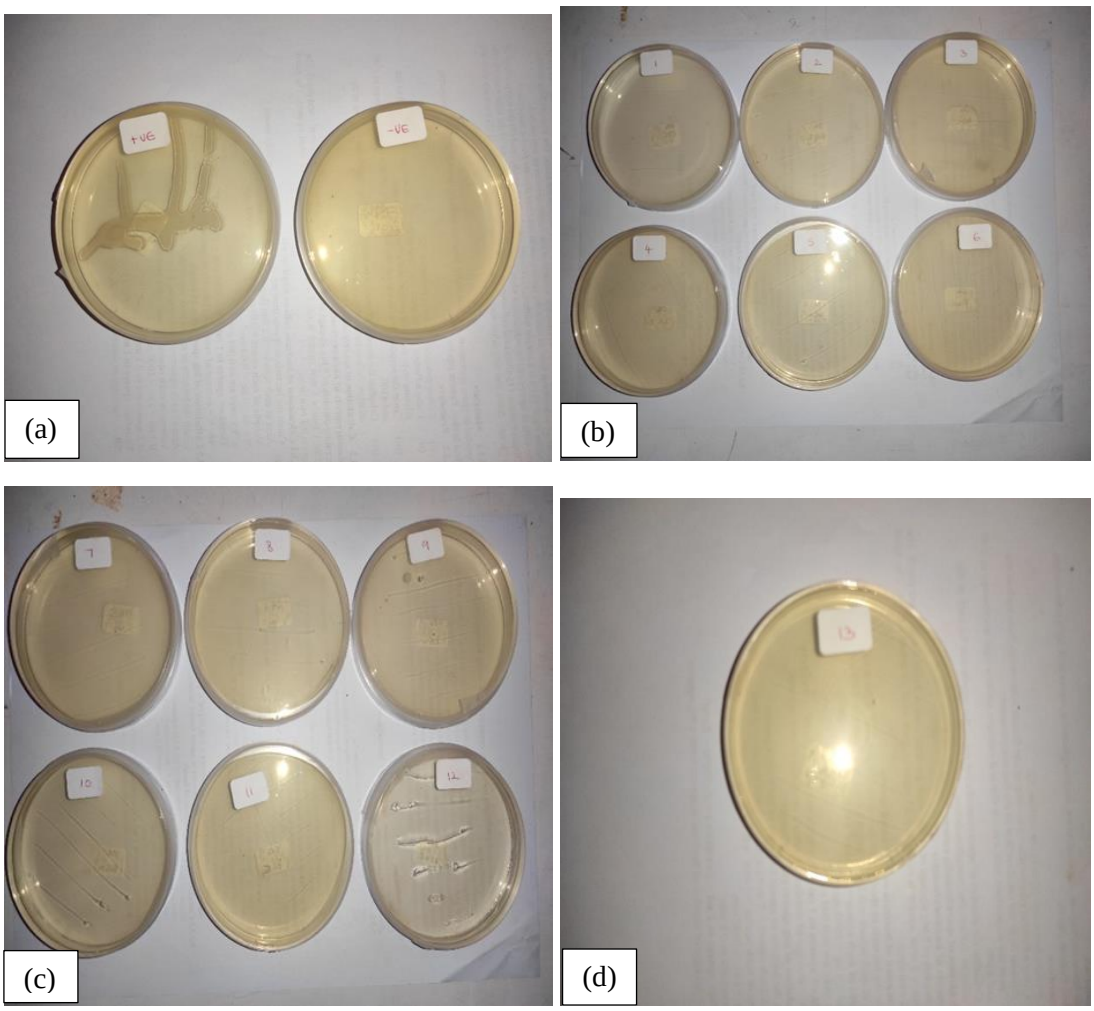

Figure 4.28: *E.coli* regrowth sfor: (a) positive control and negative control (b),(c) and (d) permeate for individual runs from 1-13 for 2nd set.

The flux of N-TiO_2-PVDF reduced with increasing NaCl concentration. Flux also increased from low pH until close to pH 7 after which the flux reduced with further increase as shown by 3D diagram in Figure 4.29

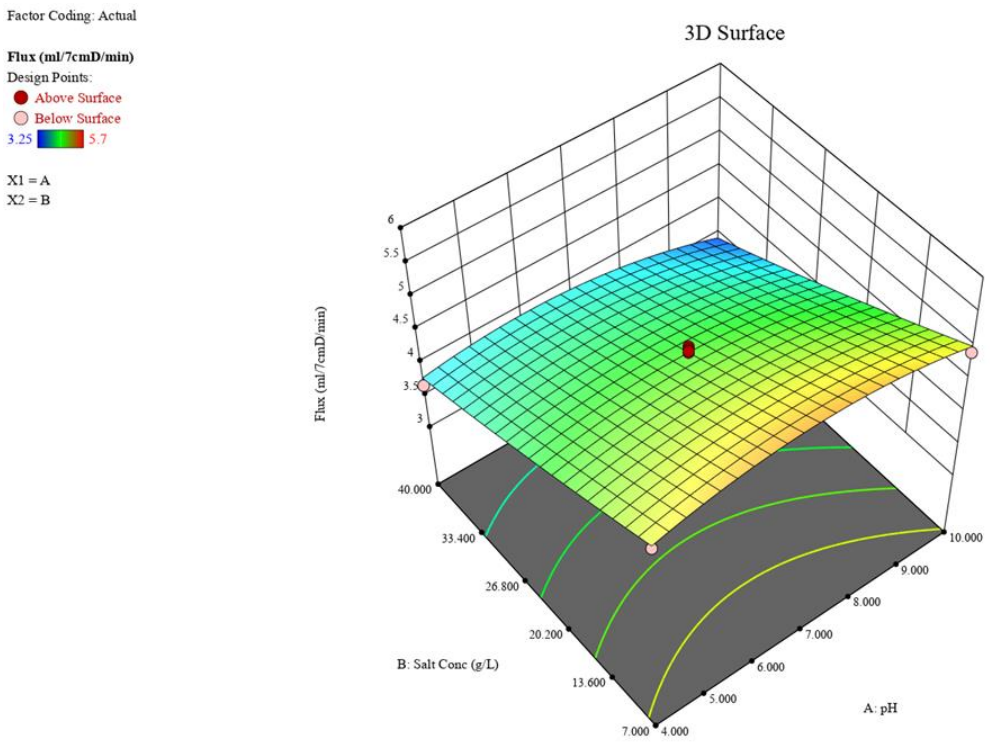

Figure 4.29: 3D diagram showing combined effect of pH and NaCl concentration on flux for 2nd set

Increasing NaCl concentrations increased concentration polarization and crystallization along N-TiO_2-PVDF surface and pores. This effect also increased as experimental run proceeded due to filtration increasing NaCl concentration continuously. This reduced the movement of water across the surface of N-TiO_2-PVDF membrane and hence reduced flux. Increasing Cl^- anion concentration (caused by increasing NaCl concentration) led increased inhibition of $OH^\cdot$ radical formation, increased charge recombination and led to the formation of weaker chloride radicals (Álvarez, Orellana-García, López-Ramón, Rivera-Utrilla, & Sánchez-Polo, 2018) this led to weaker disinfection of *E.coli* and hence increase of biofouling of membrane and reduced flux.

Increasing pH to close to point of zero charge of 6.5 led to an increase of flux as less repulsive forces acted on N-TiO_2 and *E.coli* cells (Sontakke, Modak, & Madras, 2011). This resulted to better disinfection and antifouling hence a higher flux. pH below and above the point of zero charge led to the repulsion of *E.coli* and N-TiO_2 reducing interaction and reducing disinfection, increased biofouling and less flux. Proper mixing might have reduced biofouling (Alrousan, Dunlop, McMurray, & Byrne, 2009) caused by pumps' flowrate of 0.95 L/min that ensured turbulent flow.

4.2.3.3 Numerical optimization functions

The numerical optimization function was used to determine the optimal values by maximizing flux response and getting the corresponding independent variable values that give the maximum values of the response. The goal of the response was selected to be maximized at its desirability, whereas the independent variables of pH and NaCl concentration were set to be within the range. The weights and importance function increased or decreased the emphasis of limit and ranges to the responses (Vaez, Moghaddam, & Alijani, 2012). An importance of 5 rating was selected. From the numerical optimization function, maximum flux of 5.3 ml/7cmD/min when disinfecting *E.coli* would be attained by a combination of 7g/L of NaCl and a pH of 7.0 as shown in Figure 4.30.

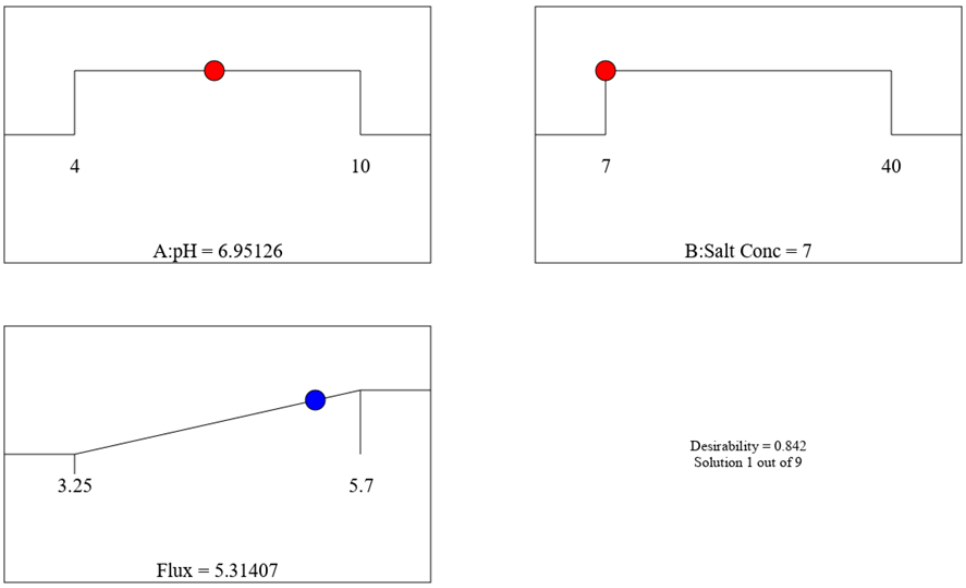

Figure 4.30: Optimum value for flux and variables required for optimum flux for 2nd set.

4.3 Performance, Durability and Reuse with N-TiO_2-PVDF

4.3.1 Performance, durability and reuse with sulphamethoxazole

4.3.1.1 Performance with pH changes

An increase of pH from 4 to 7 and 10 led to the decrease of degradation of 6mg/l of SMX from 81.3%, 69.9% and 58.1% with 1st order fitted k values of 0.0163/min, 0.012/min and 0.0088/min respectively as shown in Figure 4.31.

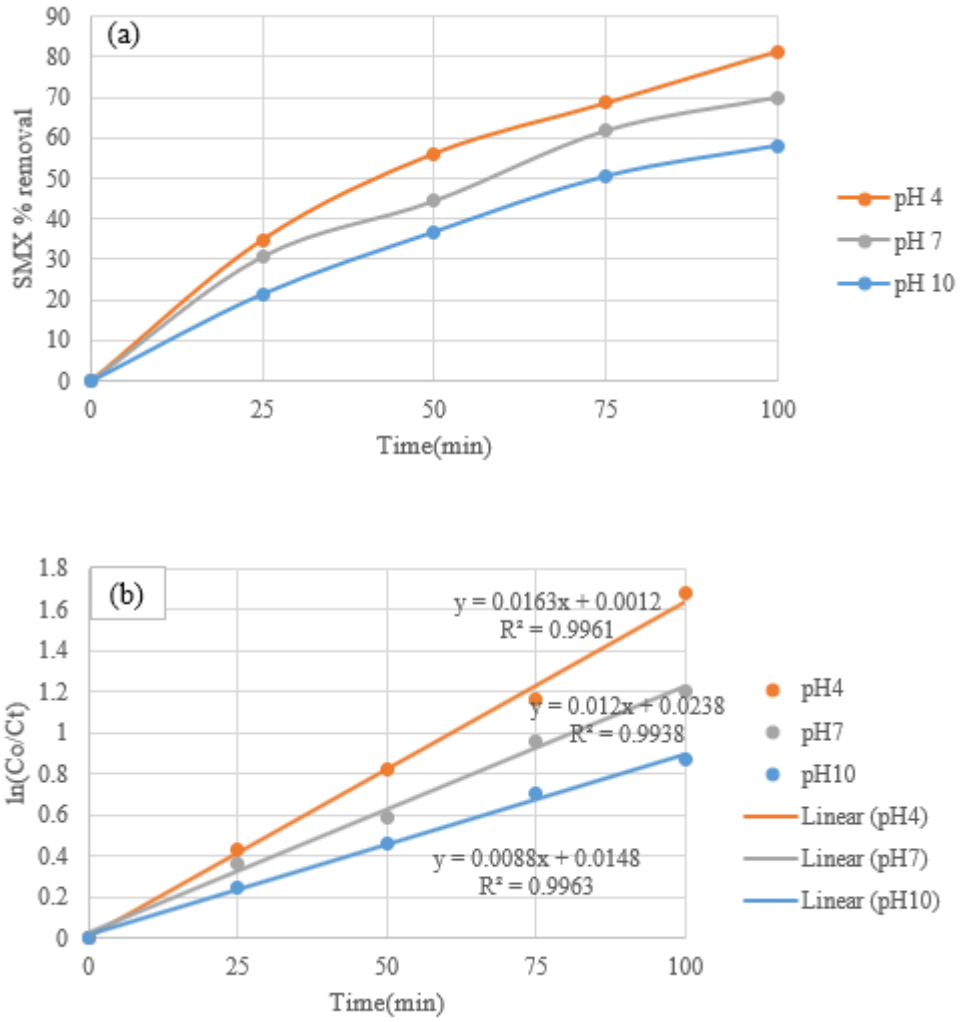

Figure 4.31: Performance of SMX degradation at pH 4, pH 7 and pH 10 in (a) SMX removal (%) and (b) fitted to 1st order kinetics.

pH was shown to affect the photodegradation, flux and TOC removal capability of SMX. This was by controlling the generation and distribution of photogenerated holes, electrons, hydroxyl and superoxide radicals (Kutuzova, Dontsova, & Kwapinski, 2021), (Wang, et al., 2020) and in turn, influence surface charges, SMX reactivity and interactions of SMX and its photodegraded intermediates with the immobilized N-TiO_2 photocatalyst on the membrane. SMX exists in diprotonic molecular form with Pka_1 of 1.97 and Pka_2 of 6.16, giving a point of zero charge of 4.06 (Serna-Carrizales, et al., 2023). At an acidic medium below the point of zero charge, SMX exists in cationic form, whereas above, it starts being anionic. On the other hand, N-TiO_2(immobilized

on membrane) has a point of zero charge of 6.4 (Thuy, et al., 2020). At pH 4, SMX possessed negative charges, whereas N-TiO_2 possessed a net positive surface charge. This oppositely charged surface and SMX molecules created electrostatic forces, increased its interactions through adsorption, and resulted in higher degradation rates. The effects of enhanced adsorption through charges reduced as pH increase led to acidic dissociation of SMX functional groups and increased negative charges (Ahmed, Pons, Lachheb, & Houas, 2014). At a higher pH of 10, both N-TiO_2 had strong negative charges, whereas SMX was strongly anionic. This caused repulsive electrostatic forces and hindered free interactions between N-TiO_2 and SMX. This decreased degradation by the absence of additional adsorption (Mourid, et al., 2020). Additionally, SMX contains a sulphuric group in its structure that carries a negative net charge (Balarak & Azarpira, 2016). This functional group additionally enhanced the attraction of SMX in acid pH of 4 and contributed to its repulsion from the negatively charged surface of N-TiO_2 at pH 10. Photocatalytic oxidation can be carried out by holes, electrons directly or through photogenerated radical such as hydroxyl, superoxide and contaminant radicals. At higher increasing pH, major anions are hydroxyl and combine readily with holes to give more hydroxyl radicals. However, SMX degradation decreased with increasing pH indicating that the major oxidative agent and mechanism is through direct hole oxidation (Wang, et al., 2020) ahead of hydroxyl radicals.

The flux of N-TiO_2-PVDF was affected by pH changes from 4, 7 and 10 and reduced relative flux of 0.77, 0.73 and 0.72 respectively by 100^{th} minute as shown by Figure 4.32.

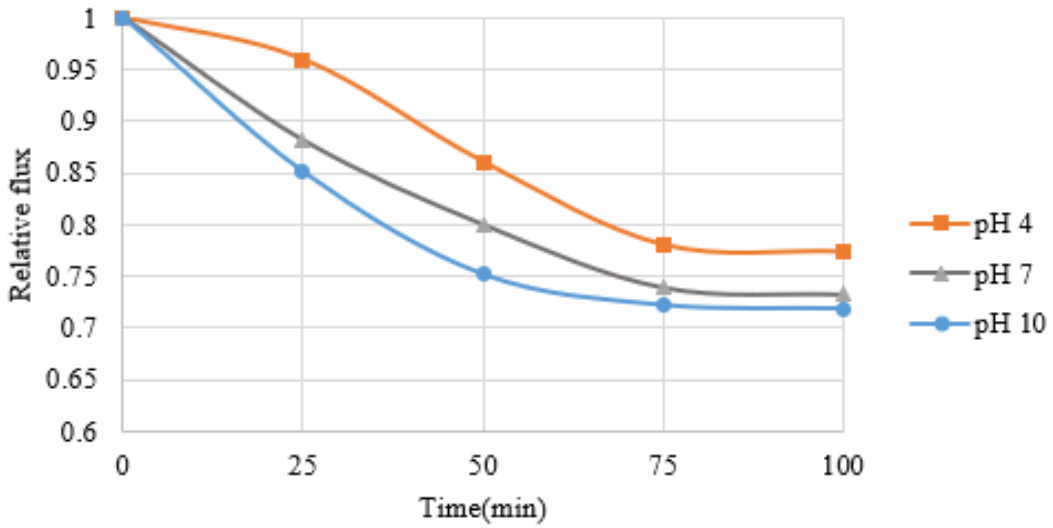

Figure 4.32: Effects of pH 4, pH 7 and pH 10 on flux performance associated with SMX removal

At acidic pH of 4, the surface charge of N-TiO_2-PVDF tends to be positively charged. This attracted the negatively charged SMX foulants leading to the deposition onto the membrane surface and pores. However, the presence of N-TiO_2 degraded the deposited SMX, effectively reducing fouling of the membrane through pore blockage and concentration polarization hence increasing flux. Coincidentally at this point, the degradation was highest. With increasing pH and increased hydroxyl anions, the number of holes reduced through consumption and generation of hydroxyl radical that would have degraded SMX as the chief oxidative agent. Consequently, this led to poor degradation rates and an increased amount of SMX that got deposited on the membrane pores and surfaces over time. This resulted in increased concentration polarization and pore blockage by SMX foulants, reducing relative flux with increasing pH.

TOC is a measure used to indicate the extent to which complete conversion of SMX to inorganic acids and water happened since degradation is stepwise and is usually degraded by holes, electrons and radicals indiscriminately. The TOC removal was

highest at Ph 7(at 65.0%), followed by pH 4(at 64.1%) and pH 10(at 56.6%) as shown in Figure 4.33.

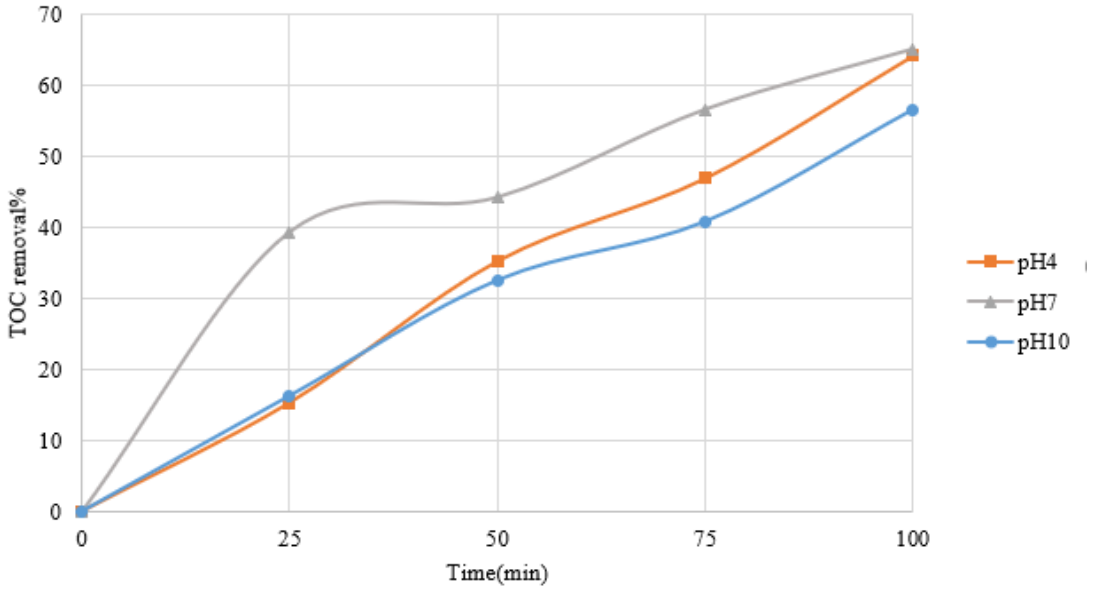

Figure 4.33: Effects of pH 4, pH 7 and pH 10 on TOC removal associated with SMX removal.

This could be attributed to most intermediates such as 5-amino-3-methylisoxazole, nitrosobenzene, 4-aminobenzenesulfonic acid, 4-nitrosulfamethoxazole and nitrophenols, N4-Acetylsulfamethoxazole, N4-Hydroxysulfamethoxazole, N-Acetyl-3-aminopyrazole,3-Aminopyrazole and N4-Sulfoxysulfamethoxazole etc. (Xie, Li, Zhang, Wang, & Huang, 2019), having points of zero charge of close to 7 and nearly coinciding with points of zero charge of immobilized N-TiO_2. The absence of like charges at neutral pH allowed free interactions and led to an increased TOC removal. At acidic or alkaline condition, intermediates had similar charges with the immobilized N-TiO_2 and caused electrostatic repulsion and hence hindered the free interactions. This lowered the TOC removal. By comparison, pH 11 appears far from Points of zero charge of 6.4 than 4.0 and might have led to PH 4 TOC removal being higher than pH 11 as stronger repulsion might have been experienced at pH 11 than at pH 4.

4.3.1.2 Performance under different concentrations of sulphamethoxazole pollutant

The concentration of SMX(an organic pollutant) is an important parameter more so to the immobilized photocatalytic membrane as it indicates the amount of organic pollutant load it can degrade, filter and mineralize as the amount of photocatalysts(in this case N-TiO_2) is already constant (Beheshti, Tehrani, & Khadir, 2019) and is essential for synthesis purposes for the amount of photocatalysts required. At 6mg/l concentration of SMX, 69.9% degradation was attained, 64.9% for 10mg/l and 58.0% for 14mg/L with 1^{st} order fitted k values of 0.012/min, 0.0102/min, 0.0085/min respectively, as shown in Figure 4.34.

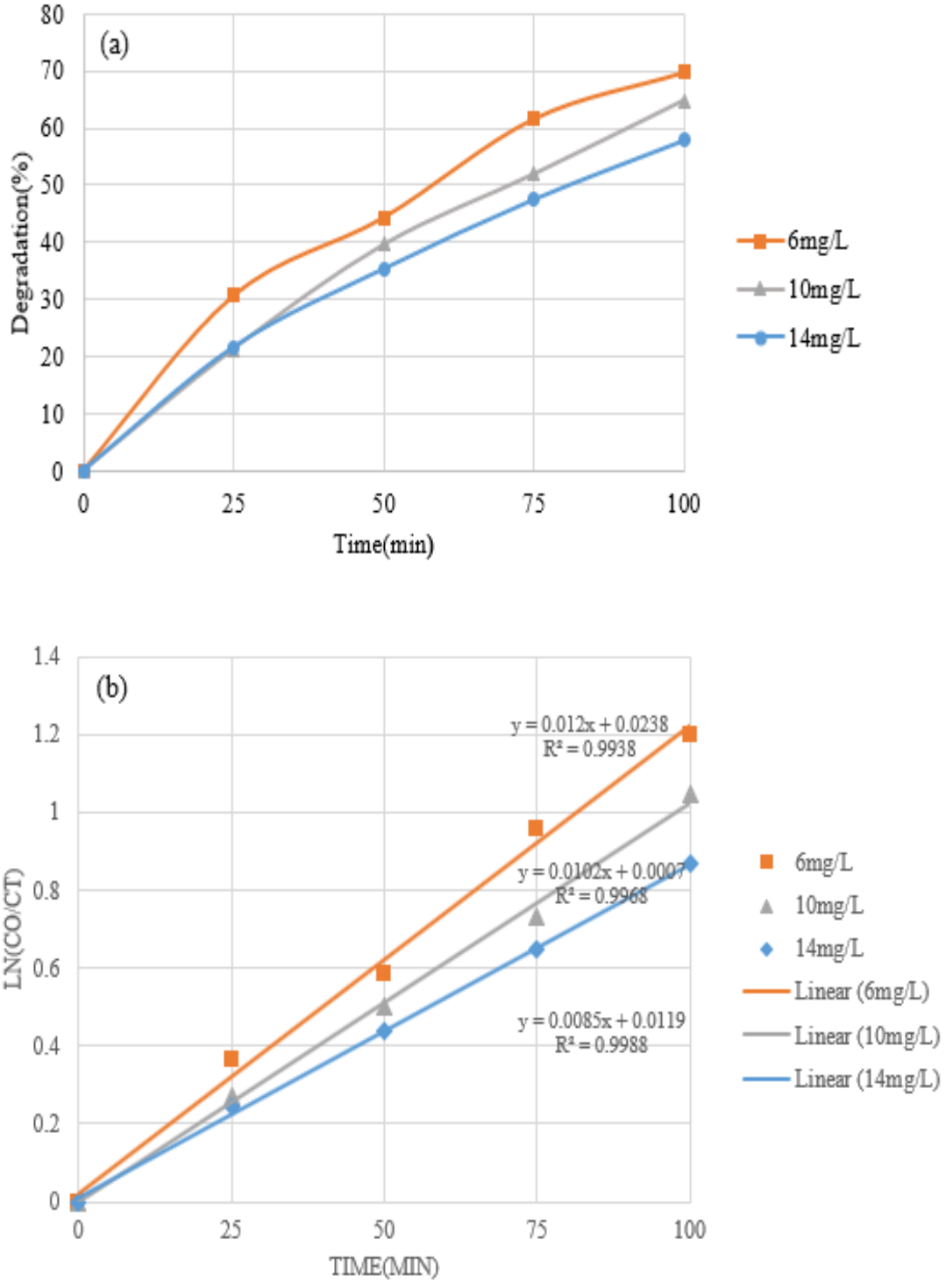

Figure 4.34: Performance of SMX degradation with 6mg/l, 10mg/l and 14mg/l SMX concentrations in (a) Degradation (%) and (b) fitted to 1st order kinetics.

With increasing concentration of SMX, more SMX molecules got attached through adsorption and saturated surfaces of immobilized N-TiO_2 photocatalyst (Cai & Hu, 2017), (Wu, et al., 2020); this reduced the amount of light reaching the immobilized N-

TiO_2 and reduced photo-separation of holes and electrons, generation of radicals and hence reduction of degradation with increasing SMX amount (Zhang, et al., 2018). Also, with increasing SMX amount getting adsorbed, direct contact interactions between holes, electrons and radicals are reduced due to the shielding effects of already adsorbed SMX, reducing degradations further (Karthikeyan, Narayanan, & Arumainathan, 2015). Increasing SMX in the solution reduced the transmittance of spiked water (Wu, et al., 2020). Lower solution transmittances implied that smaller amounts of photons reached the immobilized photocatalyst; this consequently reduced the photo-separation of charges, reduced radicals and hence reduced degradation with increasing SMX concentrations. SMX has been shown to absorb UV and visible light (Sarafraz, et al., 2020), (Balarak & Azarpira, 2016). This implied that increasing SMX concentration increased the number of light photons absorbed by SMX molecules. This effect is inevitable as light has to pass through the solution to reach the surfaces of the N-TiO_2-PVDF membrane. With this reduced amount of light reaching immobilized N-TiO_2, reduced separation of charges reduces holes, electrons and radicals happened. This reduced degradations with increasing concentrations. By increasing SMX concentrations, SMX degradation intermediates increased. These intermediates consume radicals, holes and electrons to undergo further degradation, thereby causing direct competition to the parent SMX pollutant. The intermediates are more mobile and access to the photocatalyst is faster (Musial, Mlynarczyk, & Stanisz, 2023).

Flux parameters were affected by the change of concentration of SMX pollutant. A relative flux of 0.73 was obtained for 6 mg/l SMX, 0.68 for 10mg/l and 0.6 for 14mg/L by the 100^{th} minute and last 25 minutes of sample collection as shown in Figure 4.35.

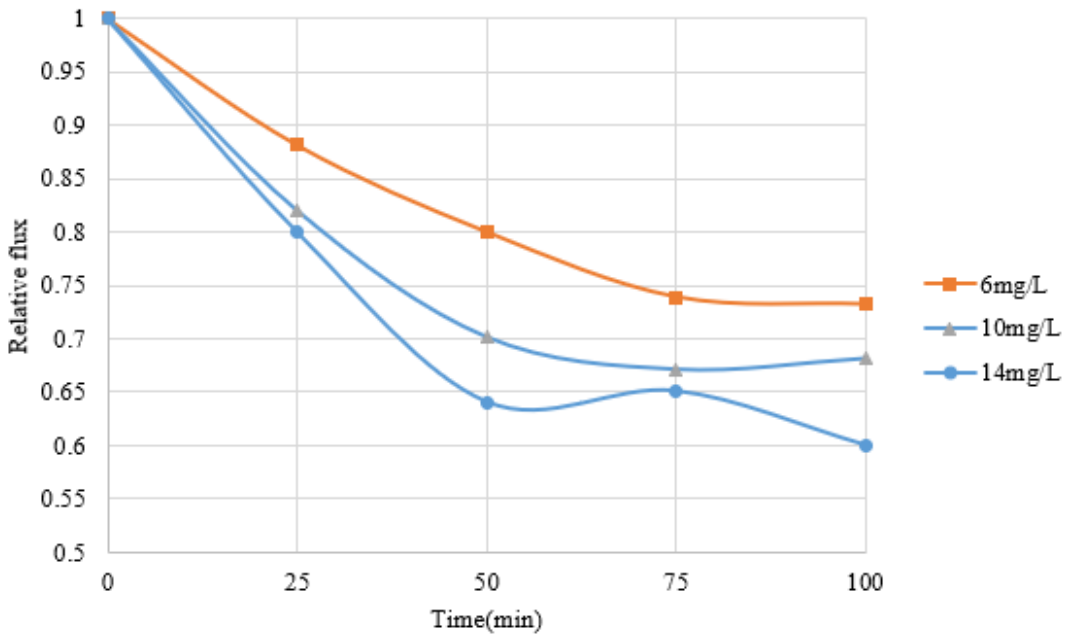

Figure 4.35: Effects of 6 mg/l, 10 mg/l and 14 mg/l SMX concentrations on flux performance associated with SMX removal.

Increasing SMX concentration increased the accumulation of SMX on the N-TiO_2-PVDF membrane pores and surfaces. This may have reduced pore size, increased hydraulic resistance, and reduced flux. Accumulation of SMX on the surface of the membrane created a concentration polarization effect and hindered the crossing over of water from feed SMX solution to the permeate and hence reduced flux. Also, by increasing SMX concentration, reduced degradation resulted and caused the rate of deposition of SMX on the surface and pores of the membrane to increase. This reduced the antifouling capability N-TiO_2 photocatalyst, further increasing resistance to water movement across the N-TiO_2-PVDF membrane and reduced the flux further. Additionally, increased SMX concentration hindered light from reaching the photocatalyst by reducing water transmittance, absorbing light and formation of adsorption coating of SMX on N-TiO_2 photocatalyst. This resulted in an increasing accumulation of SMX pollutants on the surface and pores and hence reduced permeate flux.

The TOC removal decreased with increased SMX concentration. The TOC removal was 70.0% for 6 mg/L, 29.1% and 15.9% for 10 mg/L and 14 mg/L of SMX concentration as shown in Figure 4.36.

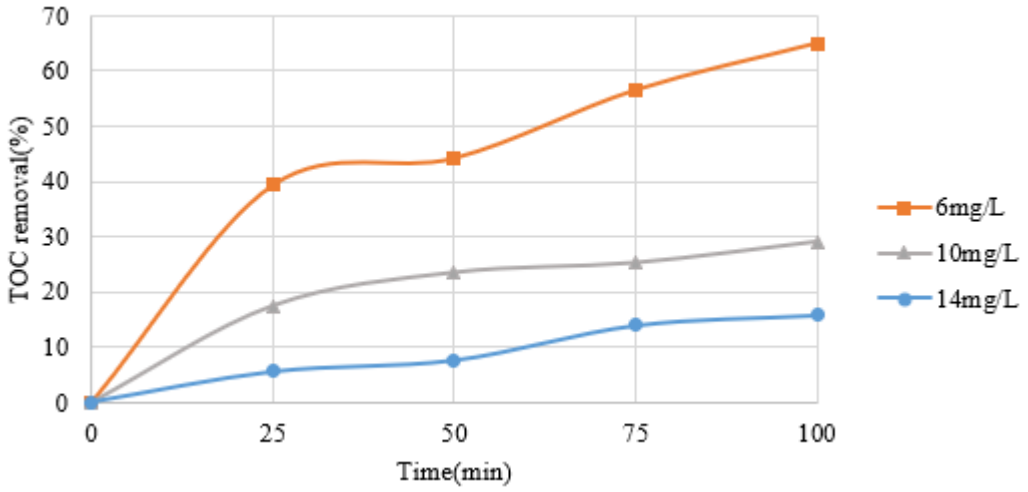

Figure 4.36: Effects of 6 mg/l,10 mg/l and 14 mg/l concentrations on TOC removal associated with SMX removal.

By increasing SMX concentration, its degradation intermediates increased. This increased the competition for radicals, holes and electrons as it is the limiting reagent due to a fixed amount of photocatalyst with a fixed number of sites. This decreased the overall TOC removal with increasing SMX concentrations.

4.3.1.3 Durability and reuse with sulphamethoxazole

The durability and reuse of N-TiO_2-PVDF membrane were carried out to ascertain its practical applicability and the possibility to carry out scaled-up operations in degradation, flux and TOC removal of SMX through 5 cycles each of 100 minutes totalling to 500 minutes operation with backwashing in between the cycles.

Degradation in the repeated use of N-TiO_2-PVDF declined with degradation removal of up to 71.5% for cycle 1, 68.9% for cycle 2, 67.6% for cycle 3, 63.7% for cycle 4 and

61.4% for cycle 5 with 1st order fitted k values of 0.0126/min, 0.0116/min, 0.011/min, 0.0102/min and 0.0096/min respectively as shown in Figure 4.37.

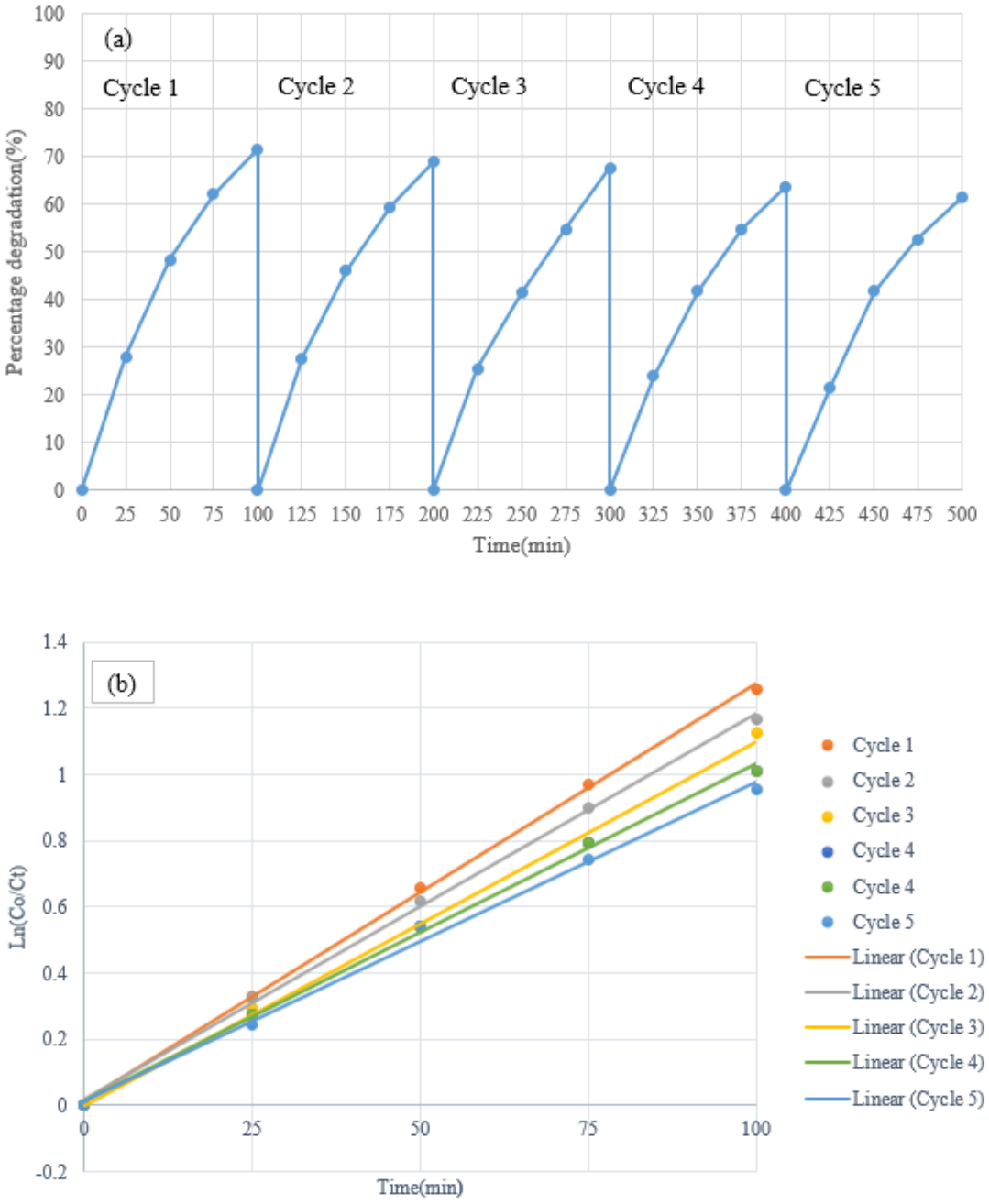

Figure 4.37 SMX degradation with repeated use for cycles 1-5 (a) in degradation (%) and (b) fitted to 1st order kinetics.

The decrease in degradation capability was 2.6% between cycles 1 and 2, 1.3% between cycles 2 and 3, 2.3% between cycles 4 and 5 and an overall of 10.1% between cycle 1 and cycle 5. There was a drop in k values of 0.001 between cycles 1 and 2, 0.0006

between cycles 2 and 3, 0.0006 between cycles 4 and 5 and an overall of 0.003 between cycles 1 and 5. The progressive decline in disinfection capability may be attributed to a minor loss of immobilized N-TiO_2 (Xie, Li, Zhang, Wang, & Huang, 2019) caused by detachment from Polyvinyl alcohol(PVA)-enhanced immobilization from the PVDF surface through experimental runs and backwashing. The remaining immobilized N-TiO_2 was a reduced quantity. It resulted in a declining generation of radicals due to reduced active sites to receive light and the generation of holes, electrons and radicals with subsequent cycles. Degradation might have also been reduced due to N-TiO_2 inactivation through SMX and its intermediates' continuous poisoning (Benjwal, De, & Kar, 2017). This lowered its capability to degrade SMX continuously with progressive runs of cycles. Additionally, exposure to concentrated light and exposure of radicals generated by $NTiO_2$ immobilized nanoparticles on the PVDF membrane resulted in decline in degradations through membrane deterioration (Lee, Ong, Lau, & Ng, 2015). UV light may have decomposed the membranes' PVDF polymer structure and PVA polymer coating, leading to its weakening mechanically and hence developing of crucks. Radicals are unselective and may end up having a negative effect of attacking the PVA and PVDF polymer structure. This may have further increased the membrane damage and degraded PVA and PVDF polymer structure, leading to its weakening mechanically and hence developing more crucks. This combination of concentrated UV and radical exposure may have led to reduced membrane selectivity and a decline in degradation capability.

Flux associated with SMX removal in the repeated use on N-TiO_2-PVDF declined by with relative flux of up to 0.979 for cycle 1, 0.970 for cycle 2, 0.967 for cycle 3, 0.960 for cycle 4, 0.685 for cycle 5 as shown in Figure 4.38.

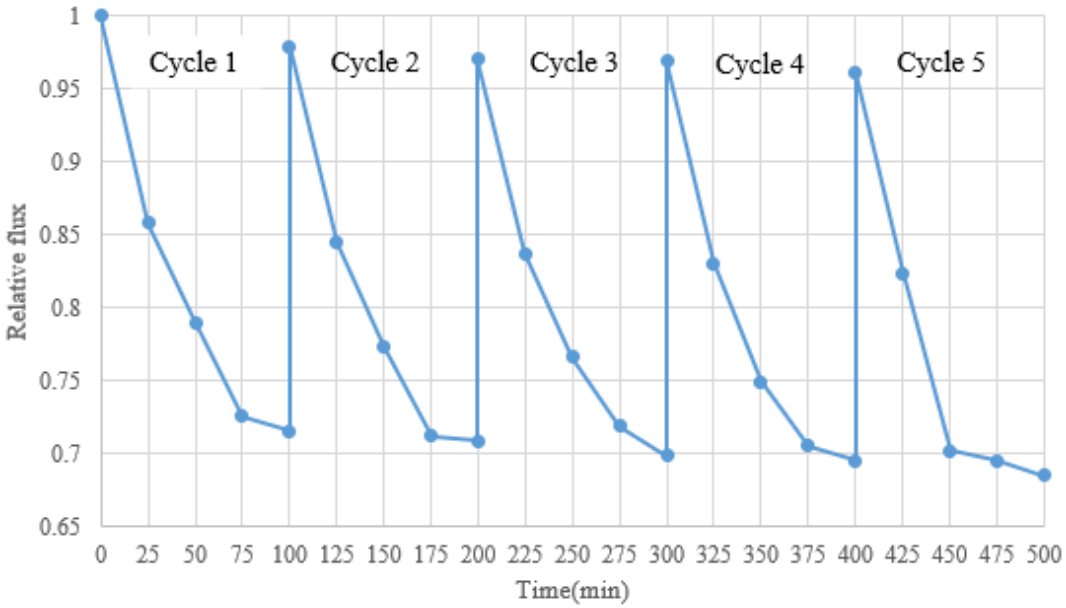

Figure 4.38: Flux performance with repeated use for cycles 1-5.

The drop in relative flux was 0.0085 between cycles 1 and 2, 0.0014 between cycles 2 and 3, 0.0084 between cycles 3 and 4, 0.2758 between cycles 4 and 5, and an overall of 0.2941 between cycles 1 and 5 by 100th minute of each cycle. The continuous drop in relative flux may be attributed to SMX and its intermediates causing minor and permanent membrane fouling since the periodic backwashing may have addressed mainly the major and temporary fouling and lesser of minor and permanent fouling. The loss of flux may be attributed to the N-TiO_2 inactivation (Aoudjita, Martins, Madjene, Petrovykhe, & Lanceros-Mendez, 2018) and detachment of immobilised N-TiO_2 from the PVA immobilisation. This reduced the antifouling capability of the N-TiO_2-PVDF through reduced amounts of N-TiO_2 nanoparticles to degrade SMX already deposited. This increased the amount of foulants deposited, leading to pore blockage and hence continuous reducing flux.

TOC removal in the repeated use of N-TiO_2-PVDF to remove SMX pollutant declined with TOC removal at 61.9% for cycle 1, 59.0% for cycle 2, 57.1% for cycle 3, 56.1% for cycle 4 and 48.3% for cycle 5 as shown in Figure 4.39.

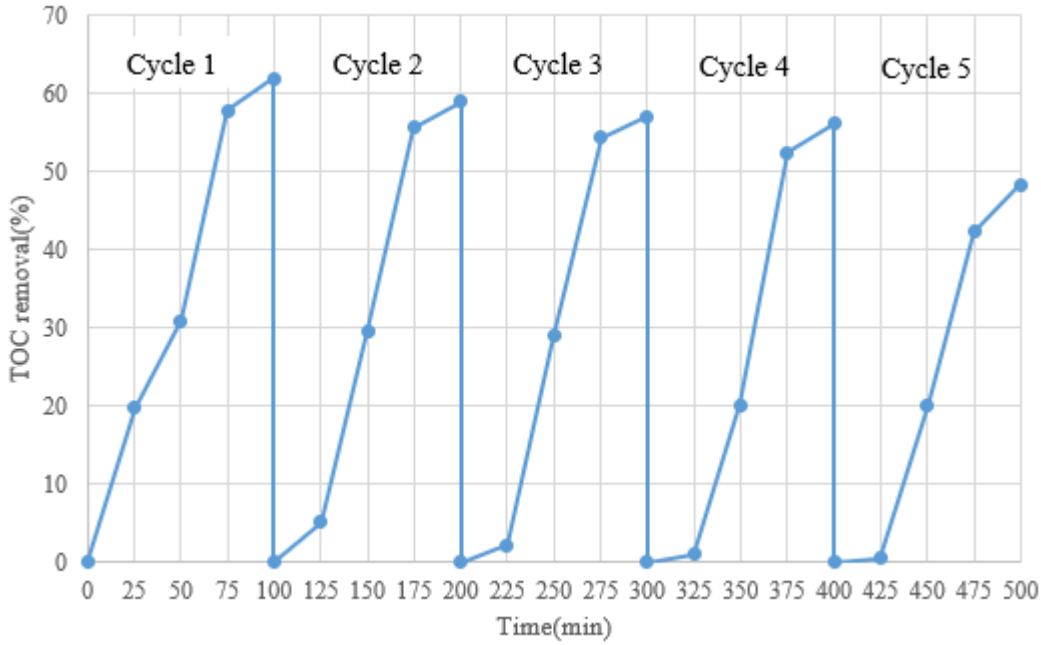

Figure 4.39: TOC removal with repeated use for cycles 1-5.

The drop in TOC removal% was 2.91% between cycles 1 and 2, 1.94% between cycles 2 and 3,0.97% between cycles 3 and 4, 7.77% between cycles 4 and 5, and 13.59% between cycles 1 and 5. This drop in TOC removal may be attributed to loss of immobilized N-TiO_2 through detachment during experimental runs and backwashing, resulting to a reduced ability to remove SMX and its intermediates (Teixeira, Martins, & Lanceros-Méndez, 2015). Additionally, loss reduction of TOC removal may be attributed to N-TiO_2 poisoning caused by SMX and its intermediates (Chiang & Doong, 2015), lowering its ability to generate hole, electrons and radicals. This resulted in lower TOC removal as cycles proceeded.

4.3.2 Performance, durability and reuse with *E.coli* pollutant

4.3.2.1 Performance under different pH *E.coli* pollutant

pH was studied for its effect on *E.coli* photocatalytic inactivation and flux performance. Varying pH gave different inactivation capabilities in deactivating *E.coli*, mainly in the 1st 25 minutes and 50 minutes of the experiment and minorly afterward. The *E.coli*

removal percentage was 89.42%, 98.07%, 99.99% and 99.99% for pH 4, 93.27%, 99.04%, 99.99% and 99.99% for pH 7, 88.46%, 98.08%, 99.99% and 99.99% for pH 10 for durations of 25 min, 50min, 75min and 100min respectively. The disinfection was expressed in terms of log reductions. The *E.coli* inactivation for the 1st 25 minutes and 50 minutes at pH 7 were 1.17 and 2.02, 0.976 and 1.72 for pH 4, and 0.94 and 1.72 for pH 10, and the results shown in Table 4.13.

Table 4.13: Periodic disinfection (%) and log reduction values of *E.coli* inactivation at pH 4, pH 7 and pH 10.

	Disinfection (%)				**Log Reduction Value (LRV)**			
pH/Time(min)	25 min	50 min	75 min	100 min	25 min	50 min	75 min	100 min
pH 4	89.42	98.07	99.99	99.99	0.98	1.72	8.42	8.42
pH 7	93.27	99.04	99.99	99.99	1.17	2.02	8.42	8.42
pH 10	88.46	98.08	99.99	99.99	0.94	1.72	8.42	8.42

pH 7 appeared to be highest in *E.coli* disinfection in the initial 50 minutes. *E.coli* is a gram-negative bacteria coated by a lipopolysaccharide layer (Chong, Jin, Zhu, & Saint, 2010) with a slight net negative charge. The nitrogen-doped nanoparticle immobilized had a point of zero charge of 6.4 (Thuy, et al., 2020). At pH 7 the interaction between *E.coli* and immobilized N-TiO_2 was less hindered due to weak repulsive forces. Also, holes and electrons are better produced at closer neutral pH and points of zero charge (Liu, et al., 2019). At pH 4, the immobilized N-TiO_2 had a net positive charge and would attract *E.coli* cells to move toward the photocatalyst leading to higher log *E.coli* inactivation. Despite this, the log inactivation fell lower in what can be attributed to *E.coli* cells developing more than 5 types of acid shock-resisting proteins (Feilizadeha, Mul, & Vossoughi, 2015) which lowered *E.coli* inactivation. At alkaline pH of 10, the strong negative surface charge of N-TiO_2 and negative charge of *E.coli* played a

significant part in causing repulsive forces between them, hindering interactions and lowering the inactivation capability. In general, the inactivation capability was minorly affected by the changes of pH in the whole 100 minutes of disinfection; this could be attributed to the continuous inactivation of immobilized N-TiO_2 (S.N., W.S., & K.G., 2015) and the provided pump flowrate of 0.95 l/min that was turbulent and ensured effective mixing. This minimized the difference in the inactivation of *E.coli* (Moradi, et al., 2022). This finding agrees with those found by (S.N., W.S., & K.G., 2015).

The flux of N-TiO_2-PVDF was affected by changes in pH value from 7 to 4 and 10 with relative fluxes of 0.302, 0.264 and 0.261 by 100th minute and last 25th minute and showed a minor effect of pH on flux as shown in Figure 4.40.

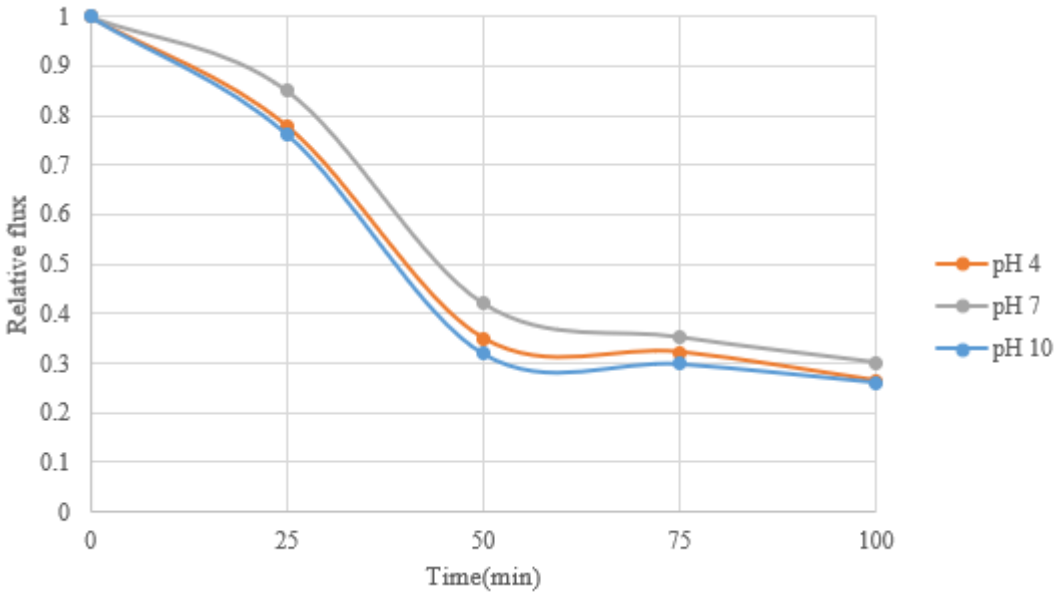

Figure 4.40: Effects of pH 4, pH 7 and pH 10 on flux associated with *E.coli* inactivation.

The study of flux is crucial as it indicates the level of pore blocking and biofouling. When *E.coli* cells are exposed to photogenerated holes, electrons and reactive radicals, they attack the cell wall and membranes leading to their dissolution to aliphatic acids (Rincón & Pulgarin, 2004) and leads to a discharge of endoplasmic contents with the

cells. The release of cell contents including DNA material cause biomolecular attachment, leading to increased fouling and flux reduction. During the 1st phase of 50 minutes, flux was observed to fall sharply and could be attributed to a majorly continuing and temporary fouling by the *E.coli* cells. *E.coli* is a bacterium of 0.45 µm, whereas the synthesized N-TiO_2-PVDF membranes had a pore size of 0.22 µm this size difference can lead to pore blockage and polarization, a major type of fouling of the membrane that is also temporary. During the next phase of 50 minutes, fouling could be attributed to both temporary and developing permanent fouling caused by biomolecules. The smaller biomolecules are responsible for firmer attachment to the membrane and its pores and may contribute more to more permanent fouling of the membrane. It could be postulated that at high disinfection rates of pH 7, major fouling caused by cell pore blockage could have been reduced through more rapturing of cells by better disinfection and led to reducing of the major and temporary type of fouling; hence a slightly higher relative flux.

4.3.2.2 Performance under different *E.coli* pollutant concentration

The effect of *E.coli* pollutant concentration was studied for *E.coli* inactivation and flux performance. By varying *E.coli* concentration, different deactivating capability was achieved. In $1.04x10^9$ CFU/l, the deactivation was 93.27% by the 25th minute, 99.04 by the 50th minute and 99.99% henceforth. In $5.2x10^8$ CFU/l, the deactivation was 94.23% by 25th minute and 99.99% henceforth. In $2.6x10^8$ CFU/l, the deactivation was 96.15% by 25th minute and 99.99% henceforth. The efficacy of *E.coli* inactivation was then expressed in log reduction values (LRV). In $1.04x10^9$ CFU/l, the log reduction was 1.17 by 25th minute, 2.02 by 50th minute and 8.42 henceforth. In $5.2x10^8$ CFU/l, the deactivation was 1.24 by 25th minute and 8.42 henceforth. In $2.6x10^8$ CFU/l, the

deactivation was 1.42 by 25th minute and 8.42 henceforth. The results are shown in Table 4.14.

Table 4.14: Periodic disinfection (%) and log reduction values of *E.coli* inactivation with 1.04x10^{9} CFU/l, 5.2x10^{8} CFU/l and 2.6x10^{8} CFU/l *E.coli* concentrations.

	Disinfection (%)				**Log Reduction Value (LRV)**			
E.coli concentration/Time(min)	25 min	50 min	75 min	100 min	25 min	50 min	75 min	100 min
1.04x10^{9} CFU/l	93.27	99.04	99.99	99.99	1.17	2.02	8.42	8.42
5.2x10^{8} CFU/l	94.23	99.99	99.99	99.99	1.24	8.42	8.42	8.42
2.6x10^{8} CFU/l	96.15	99.99	99.99	99.99	1.42	8.42	8.42	8.42

The efficacy of *E.coli* inactivation increased with reducing concentrations of *E.coli.* *E.coli* has been shown to produce opaque colonies. Therefore, with increasing *E.coli* concentrations, the opacity of *E.coli* spiked water used was increased. This resulted in the blocking and absorbing of light (Chong, Jin, & Saint, 2011). This reduced the amount of light that penetrated the solution and reached the immobilized photocatalyst on the membrane surface. This reduced the charge separation of electrons and holes, reducing *E.coli* inactivation capability. With increased concentrations, the log reductions are reduced and can be attributed to the further consumption of electrons, holes and radicals by already inactivated *E.coli* cells (Huang, et al., 2020) to cause cell wall and cell membranes to rapture into aliphatic acids. This released the cytoplasmic contents, further consumed holes, electrons and radicals to undergo degradation. This contributed to increasing the shielding of live *E.coli* cells from getting attacked by holes, electrons and radicals, reducing log reductions with increasing *E.coli* concentration. Additionally, the amount of N-TiO_2 immobilized was fixed. This implied that the number of active sites for *E.coli* inactivation was also constant and hence the amount of radicals that could be generated was a limiting factor (Chong, Jin,

& Saint, 2011). Therefore, with increased *E.coli* concentrations, the log reductions were bound to reduce with increasing *E.coli* concentrations.

Flux of N-TiO_2-PVDF membrane was adversely affected by changes in *E.coli* concentration with a relative flux of 0.302 by 100^{th} and the last 25 minutes for $1.04x10^9$ CFU/l, 0.373 for $5.2x10^8$ CFU/l and 0.424 for $2.6x10^8$ CFU/l as shown in Figure 4.41.

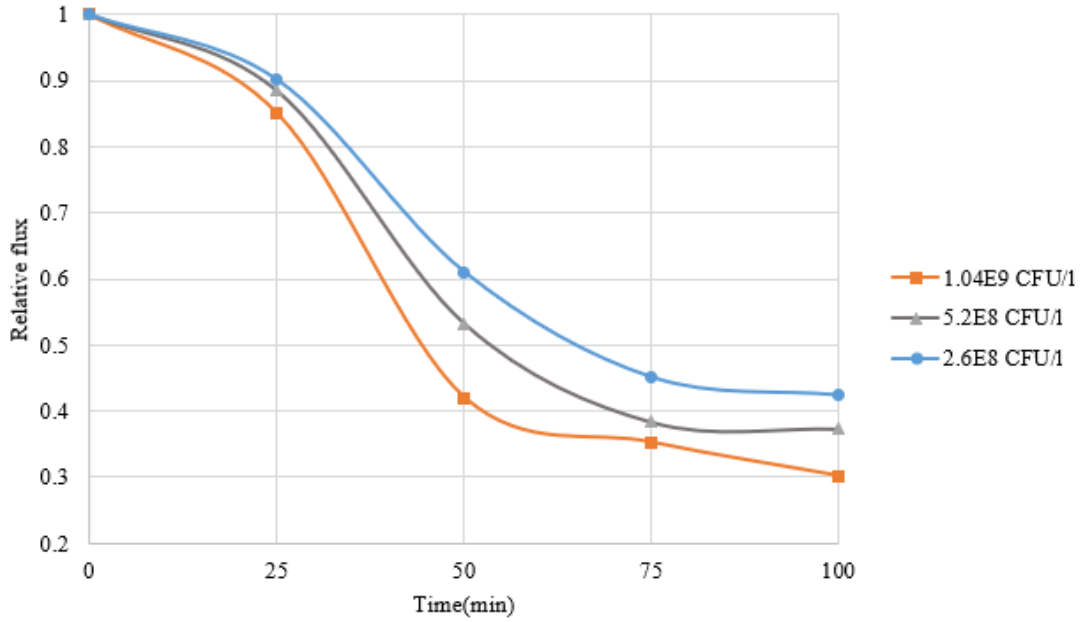

Figure 4.41: Effects of $1.04x10^9$ CFU/l, $5.2x10^8$ CFU/l and $2.6x10^8$ CFU/l *E.coli* concentrations on flux performance associated with *E.coli* inactivation.

The relative flux reduced with increasing *E.coli* concentration and could also be attributed to the increase of major and temporary fouling types compared to the minor and permanent types of fouling (Ezugbe & Rathilal, 2020). The cells that caused pore blockage and concentration polarization (Jadoun, Mreny, Saad, & Azaizeh, 2018) along the membrane surface increased with increased *E.coli* concentration. Additionally, with decreasing concentrations, the *E.coli* inactivation by immobilized N-TiO_2 increased, the major and temporary type of fouling reduced due to hole, electrons and radical attacks leading to rapturing of *E.coli* cells and hence better antifouling by the immobilized photocatalyst. This led to an increasing relative flux.

4.3.2.3 Durability and reuse with *E.coli*

The durability and reuse of N-TiO_2-PVDF membrane were carried out to ascertain its practical applicability and the possibility of carrying out scaled-up operations in disinfection and flux removal of *E.coli* through 5 cycles each of 100 minutes totalling 500 minutes operation with backwashing in between the cycles.

Disinfection in the repeated use of N-TiO_2-PVDF showed a minor difference in *E.coli* disinfection with *E.coli* inactivation of 99.04% for cycle 1, 99.04% for cycle 2, 98.08% for cycle 3, 97.12% for cycle 4, 97.12% for cycle 5 by 50^{th} minute and 99.99% by 100^{th} minute as shown in Figure 4.42.

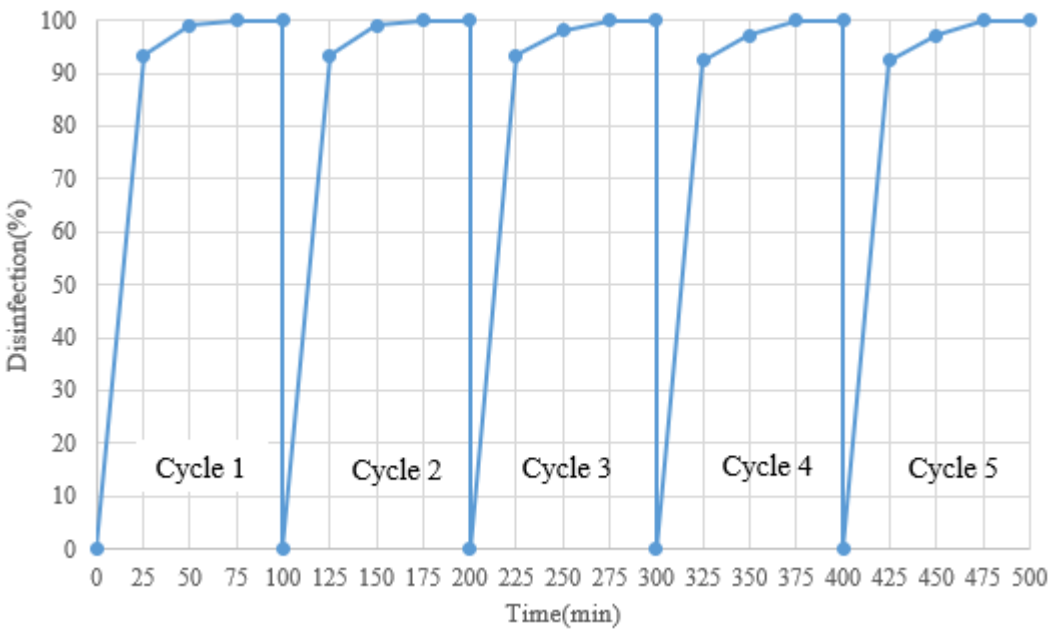

Figure 4.42: *E.coli* disinfection with repeated use for cycles 1-5.

There was no decrease in disinfection capability between cycle 1 and cycle 2 as well as cycle 4 and 5 by the 50^{th} minute. A 0.96 reduction of disinfection was observed between cycle 2 and cycle 3 and between cycle 3 and 4. An overall drop of disinfection of 1.92% was observed between the first and the last cycle by 50^{th} minute. The disinfection

capabilities of each cycle were expressed in terms of log reduction values after every 25 minutes of each cycle, and results shown in Table 4.15.

Table 4.15: Periodic log reduction values of *E.coli* inactivation for cycles 1-5.

	Log reduction Values (LRV)			
Cycle/Time(min)	25min	50min	75min	100min
Cycle 1	1.17	2.02	8.42	8.42
Cycle 2	1.17	2.02	8.42	8.42
Cycle 3	1.17	1.72	8.42	8.42
Cycle 4	1.11	1.54	8.42	8.42
Cycle 5	1.11	1.54	8.42	8.42

The log reduction values declined only within the 1st 50 minutes and were constant afterward. The slight decrease in log reductions could be attributed to competition for adsorption, holes, electrons and radicals generated from active sites by continuously increasing and permanent bio-organic foulants that were released from components of degradation of cell wall, cell membrane and the released cytoplasmic contents caused by raptured cell wall and lysis of *E.coli* cells (Hoek, Ghosh, Huang, Liong, & Zink, 2011). Continuous use caused an increase in permanent foulants that could not be backwashed effectively hence a decline in overall disinfection. Additionally, the presence of bio-organics and *E.coli* cells may have led also to the inactivation of immobilized N-TiO_2 by attaching permanently and shielding the nanoparticles from receiving photons thereby lowering its photocatalytic activity (Grieken, Marugán, Sordo, & Pablos, 2009). Inactivated and permanently attached *E.coli* cells could still consume more radicals, thereby causing a slight decline in disinfection as cycles proceeded.

Flux associated with *E.coli* disinfection in the repeated use on N-TiO_2-PVDF declined by with relative flux of up to 0.30 for cycle 1, 0.281 for cycle 2, 0.268 for cycle 3, 0.241 for cycle 4, 0.224 for cycle 5 as shown in Figure 4.43.

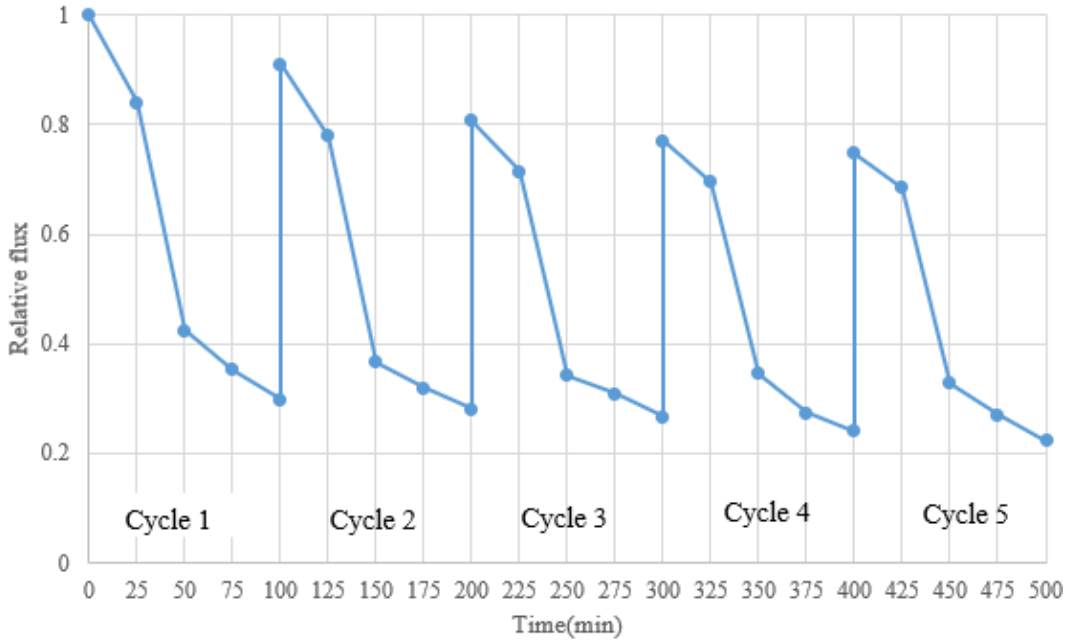

Figure 4.43: Flux performance with repeated use for cycles 1-5 associated with *E.coli* disinfection.

The drop in relative flux was 0.017 between cycle 1 and 2, 0.014 between cycle 2 and 3, 0.027 between cycle 3 and 4, 0.017 between cycle 4 and 5, and an overall of 0.075 between cycle 1 and 5 by 100th minute of each cycle. The continuous decline after backwashing regeneration may be attributed to bacterial DNA, cytoplasmic contents and polysaccharides attached to the membrane's internal pore structure, resulting in permanent fouling (Ren, Guo, Li, & Wang, 2023). This reduced flux. Additionally, the DNA, cytoplasmic contents and polysaccharides may have participated in immobilized N-TiO_2 photocatalyst inactivation by getting adsorbed permanently on its surface. This reduced the generation of holes, electrons and related photogenerated radicals, reducing bio-foulants removal ability. This led to continuous accumulation of bio-foulants, increasing the permanent foulants attachment. This reduced the relative flux drastically.

CHAPTER FIVE: CONCLUSIONS AND RECOMMENDATION

5.1 Conclusions

The study aimed at synthesizing and applying solar photocatalytic membranes for disinfection and degradation of organic pollutants in wastewater with sulphamethoxazole and *E.coli* as contaminants of focus. UV-Vis spectroscopy showed a red-shifting of light absorbance from 400nm (titanium dioxide) to 440nm (nitrogen-doped titanium dioxide), into the visible light region. The Pl spectra showed low-intensity photoluminescence intensity indicating that nitrogen-doped titanium dioxide had improved charge separation and suppression of charges recombination. The presence of incorporated nitrogen was confirmed by FTIR peaks and bending vibrations at 1420 cm^{-1}, 1170 cm^{-1},1220 cm^{-1} and 1250 cm^{-1} and EDX nitrogen elemental composition of 1.26wt%. The water contact angle reduced by 81.39%, indicating increased hydrophilicity. This desired characteristic indicated better antifouling of the synthesized membrane. SEM-EDX also confirmed the presence of immobilized N-TiO_2 on the surface with a composition of 0.42wt% for titanium and 0.01wt% for nitrogen.

The 1st and 2nd sets of experiments investigated the multivariate effect of pH and NaCl concentration on degradation%, TOC removal for sulphamethoxazole, *E.coli* elimination% (disinfection%) and flux for both. Both experiments were optimized using CCD based on RSM by creating equation models. In the 2nd set, *E.coli* removal relied exclusively on *E.coli* size exclusion through 0.22µm membrane pore size and could only be modeled through flux. In 1st set, degradation and flux increased with decreased pH and NaCl concentration. TOC removal increased with a decrease in NaCl concentration, with the highest percentage close to neutral pH. This was attributed to SMX point of zero charge of pH 4, most SMX intermediates points of zero charge falling close to pH 7, negative effects of chloride anion on Hydroxyl radicals and

concentration polarization of NaCl. In the 2nd set, the highest flux appeared at close to pH 7 and was controlled by NaCl concentration polarization and pH. The point of zero charge of immobilized N-TiO_2 closely coincided with the highest flux points, indicating the antifouling of membranes by N-TiO_2 photocatalytic disinfection of *E.coli*. Similarly, NaCl concentration had the same effects of reducing flux through reduced disinfection, through chloride ion negative effects on hydroxyl radicals and concentration polarization. Optimization was carried out on 1st set of experiments and gave the highest degradation of 76.5% (at pH 4.6 and 7.8 g/l NaCl), a flux of 9.8 ml/7cmD/min (at pH 4 and 7g/l NaCl) and TOC removal of 58% (at pH 7.3 and 11.7 g/l NaCl). Optimization on 2nd set had the highest flux of 5.3 ml/7cmD/min (at pH 7.0 and 7g/l NaCl).

The performance of N-TiO_2-PVDF was studied for its performance in different pH values and concentrations of SMX with 6 mg/L SMX contaminant. The highest degradation was at pH 4 with 81.3% and changes were attributed to SMX interactions with nanoparticles and availability of holes as the primary oxidant. Flux was highest with a relative flux of 0.78 at pH 4 and was attributed to its dependence on antifouling performance by N-TiO_2. The TOC removal was highest at 65.0% for pH 7 and changes could be attributed to most SMX intermediates having points of zero charge near neutral. In different concentrations of SMX, 6 mg/l had the highest degradation at 69.9% and changes mainly attributed to being caused by the increasing attachment of SMX molecules on N-TiO_2 surfaces. The related flux was highest with a relative flux of 0.74 for 6 mg/L and was attributed to the increasing amounts of foulants. The TOC removal was highest at 69.9% for 6 mg/L SMX and was attributed to increased competition for limited radicals by the increasing concentrations of SMX and its intermediates. With an *E.coli* concentration of $1.04x10^9$ CFU/l, pH was varied. At pH

7 the removal was highest at 93.27% at 25th minute and was attributed to weak repulsive forces. The related flux also varied with the highest relative flux being 0.307 for pH 7 and was attributed to the antifouling performance of N-TiO_2 on various types of fouling. The durability and reuse of N-TiO_2-PVDF was studied through repeated 5 cycles of 6 mg/l SMX pollutant and 1.04x10^9 CFU/l *E.coli* with periodic backwashing. The decrease in degradation was 10.1% between cycle 1 and 5 and the continuous reduction of SMX degradation was mainly attributed to continuous and minor detachment of immobilized N-TiO_2 from membranes surface. The decrease in related flux was 0.294 between cycle 1 and 5, and the decrease attributed to increasing of minor and permanent fouling type. The decrease in TOC removal was 13.6% between cycle 1 and 5, and its' decrease also attributed to continuous minor detachment of immobilized N-TiO_2. With varied concentrations of *E.coli,* the disinfection was highest at 96.15% for 2.6x10^8 CFU/l in the 1st 25 minutes. This was attributed to *E.coli* nature of increasing light obstruction and absorption with increasing *E.coli* concentration. The relative flux was highest at 0.424 for 2.6x10^8 CFU/l by 100th minute. It was attributed to the direct increase of fouling types and reduced antifouling by immobilized and limited N-TiO_2 photocatalyst as the concentration of *E.coli* was increased. With 1.04x10^9 CFU/l *E.coli* for durability and reuse, the disinfection performance decrease was by 1.92% for cycle 1 to 5 within the 1st 50 minutes. This initial minimal changes in cycles disinfection were attributed to further consumption of radicals by already inactivated *E.coli* and cytoplasmic contents. The decrease in related relative flux was 0.074 between cycle 1 to 5. The decline in relative flux was attributed to increasing permanent fouling types caused by bio-foulants. The performance test indicated the best conditions to be met for maximization of the N-TiO_2-PVDF membrane removal of contaminants. The

insignificant drop in performance with repeated use demonstrated N-TiO_2-PVDF had high durability and was attractive towards scaleup efforts.

5.2 Recommendations

This study demonstrated the application of nitrogen-doped titanium dioxide polyvinyl deflouride membrane in the removal of sulphamethoxazole antibiotic and *E.coli* water contaminants from water using the cooperation of membrane filtration and visible-light-driven nitrogen-doped titanium dioxide nanoparticles and showed enormous capability. To pave way for increased efficiency and attract large scale applications of the technology, further studies can be recommended in the following areas:

a. Further techniques and effort should be applied to increase visible light utilization by titanium dioxide nanoparticles through environmentally friendly dopants to increase their efficiency in harnessing the visible solar spectrum, increasing its decontamination capability.
b. Additional techniques, such as air spurging and air scouring, may also be incorporated to increase turbulence and reduce foulant attachment on nanoparticles and the membrane. This will enhance the cross-filtration mechanism already applied, and reduce pollutant poisoning on nanoparticles and membrane fouling.
c. Advanced cleaning techniques such as back pulsing washing and use of titanium dioxide and polyvinyl deflouride friendly acids and bases could be applied to reduce the minor and permanent type of fouling that lowered the productivity of the membrane with repeated use. Back pulsing may be used to enhance the cleaning agents.

REFERENCES

Ahmed, O., Pons, M.-N., Lachheb, H., & Houas, A. (2014). Degradation of sulfamethoxazole by photocatalysis using supported TiO2. *Sustainable Environment Research*, 381-387.

Ajiboye, T. O., Babalola, S. O., & Onwudiwe, D. C. (2021). Photocatalytic Inactivation as a Method of Elimination of E. coli from Drinking Water. *Appplied sciences*, 1313.

Al-Abri, M., Al-Ghafri, B., Bora, T., Dobretsov, S., Dutta, J., Castelletto, S., . . . Boretti, A. (2019). Chlorination disadvantages and alternative routes for biofouling control in reverse osmosis desalination. *clean water*.

Al-Mamuna, M., Kaderb, S., Islamb, M., & Khana, M. (2019). Photocatalytic activity improvement and application of UV-TiO2 photocatalysis in textile wastewater treatment: A review. *Journal of Environmental Chemical Engineering*.

Alrousan, D. M., Dunlop, P. S., McMurray, T. A., & Byrne, J. A. (2009). Photocatalytic inactivation of E. coli in surface water using immobilised nanoparticle TiO2 films. *water research*, 47–54.

Álvarez, M., Orellana-García, F., López-Ramón, M. V., Rivera-Utrilla, J., & Sánchez-Polo, M. (2018). Influence of operational parameters on photocatalytic amitrole degradation using nickel organic xerogel under UV irradiation. *Arabian Journal of Chemistry*, 564-572.

Ambulkar, A. (2021). *wastewater treatment*. Retrieved october 23, 2021, from Britannica: https://www.britannica.com/technology/wastewater-treatment/Sources- of-water-pollution#ref1098057

Aoudjita, L., Martins, P., Madjene, F., Petrovykhe, D., & Lanceros-Mendez, S. (2018). Photocatalytic reusable membranes for the effective degradation of tartrazine with a solar photoreactor. *Journal of Hazardous Materials*, 408-416.

Argurio, P., Fontananova, E., Molinari, R., & Drioli, E. (2018). Photocatalytic Membranes in Photocatalytic Membrane Reactors. *processes*.

Arif, Z., Sethy, N. K., Kumari, L., Mishra, P. K., & Verma, B. (2019). Antifouling behaviour of PVDF/TiO2 composite membrane: a quantitative and qualitative assessment. *Iranian Polymer Journal*, 301–312.

Balarak, D., & Azarpira, H. (2016). Photocatalytic degradation of Sulfamethoxazole in water: investigation of the effect of operational parameters. *International Journal of ChemTech Research*, 731-738.

bank, t. w. (2017, september 20). *Water Resources Management*. Retrieved october 23, 2021, from unnderstanding poverty: https://www.worldbank.org/en/topic/waterresourcesmanagement#1

Bar-Ilan, O., Louis, K. M., Yang, S. P., Pedersen, J. A., Hamers, R. J., Peterson, R. E., & Heideman, W. (2012). Titanium dioxide nanoparticles produce phototoxicity in the developing zebrafish. *Nanotoxicology*.

Beheshti, F., Tehrani, R. M., & Khadir, A. (2019). Sulfamethoxazole removal by photocatalytic degradation utilizing TiO2 and WO3 nanoparticles as catalysts: analysis of various operational parameters. *International Journal of Environmental Science and Technology*, 7987–7996.

Bell, M. (2021, January 28). *World Economic Forum*. Retrieved september 15, 2021, from www.weforum.org: https://www.weforum.org/agenda/2021/01/if-you-want-to-make-progress-on-all-the-major-global-challenges-start-with-water/

Benjwal, P., De, B., & Kar, K. K. (2017). 1-D and 2-D morphology of metal cation co-doped (Zn, Mn) TiO2 and investigation of their photocatalytic activity. *Applied Surface Science*, 262-272.

Cai, Q., & Hu, J. (2017). Decomposition of sulfamethoxazole and trimethoprim by continuous UVA/LED/TiO2 photocatalysis: Decomposition pathways, residual antibacterial activity and toxicity. *Journal of Hazardous Materials*, 527-536.

Chen, X., Hu, Y., Xie, Z., & Wang, H. (2018). Materials and Design of Photocatalytic Membranes. *Current Trends and Future Developments on (Bio-) Membranes*.

Chen, X., Hu, Y., Xie, Z., & Wang, H. (2018). Materials and Design of Photocatalytic Membranes. *Current Trends and Future Developments on (Bio-) Membranes*.

Cheng, X., Yu, X., Xing, Z., & Yang, L. (2016). Synthesis and characterization of N-doped TiO2 and its enhanced visible-light photocatalytic activity. *Arabian Journal of Chemistry*, S1706-S1711.

Chiang, L.-F., & Doong, R.-a. (2015). Enhanced photocatalytic degradation of sulfamethoxazole by visible-light-sensitive TiO2 with low Cu addition. *Separation and Purification Technology*.

Chong, M. N., Jin, B., Chow, C. W., & Saint, C. (2010). Recent developments in photocatalytic water treatment technology: a review. *Water Research*, 2997-3027.

Chong, M. N., Jin, B., Zhu, H., & Saint, C. (2010). Bacterial inactivation kinetics, regrowth and synergistic competition in a photocatalytic disinfection system using anatase titanate nanofiber catalyst. *Journal of Photochemistry and Photobiology A: Chemistry*, 1-9.

Crini, G., & Lichtfouse, E. (2019). Advantages and disadvantages of techniques used for wastewater treatment. *Environmental Chemistry Letters*.

Cruz, N. K., Semblante, G. U., Senoro, D. B., You, S.-J., & Lu, S.-C. (2013). Dye degradation and antifouling properties of polyvinylidene fluoride/titanium oxide membrane prepared by sol–gel method. *Journal of the Taiwan Institute of Chemical Engineers*.

Dong, H., Zeng, G., Tang, L., Fan, C., Zhang, C., He, X., & He, Y. (2015). An overview on limitations of TiO2-based particles for photocatalytic degradation of organic pollutants and the corresponding countermeasures. *ScienceDirect*.

Du, J., Xu, S., Zhou, Q., Li, H., Fu, L., Tang, J.-H., & Jin, M.-Q. (2019). The ecotoxicology of titanium dioxide nanoparticles, an important engineering nanomaterial. *Toxicological & Environmental Chemistry*.

Du, J., Xu, S., Zhou, Q., Li, H., Fu, L., Tang, J.-H., & Jin, M.-Q. (2019). The ecotoxicology of titanium dioxide nanoparticles, an important engineering nanomaterial. *Toxicological & Environmental Chemistry*.

Du, X., Bai, X., Xu, L., Yang, L., & Jin, P. (2020). Visible-light activation of persulfate by TiO2/g-C3N4 photocatalyst toward efficient degradation of micropollutants. *Chemical Engineering Journal*, 123245.

Esfahani, A. R., Firouzi, A. F., Sayyad, G., & Kiasat, A. (2013). Pb(II) removal from aqueous solution by polyacrylic acid stabilized zero-valent iron nanoparticles: Process optimization using response surface methodology. *Research on Chemical Intermediates*, 431–445.

Ezugbe, E. O., & Rathilal, S. (2020). Membrane Technologies in Wastewater Treatment: A Review. *Membranes*.

Ezugbe, E. O., & Rathilal, S. (2020). Membrane Technologies in Wastewater Treatment: A Review. *Membranes*, Membrane Technologies in Wastewater Treatment: A Review.

Feilizadeha, M., Mul, G., & Vossoughi, M. (2015). E. coli inactivation by visible light irradiation using a Fe–Cd/TiO2 photocatalyst : Statistical analysis and optimization of operatingparameters. *Applied Catalysis B: Environmental*, 441–447.

Ghernaout, D. (2017). Water Treatment Chlorination: An Updated Mechanistic Insight Review. *Chemistry Research Journal*.

Giannakopoulou, T., Papailias, I., Todorova, N., Boukos, N., Liu, Y., Yu, J., & Trapalis, C. (2017). Tailoring the energy band gap and edges' potentials of g-C3N4/TiO2 composite photocatalysts for NOx removal. *Chemical Engineering Journal*, 571-580.

Gomes, J., Lincho, J., Domingues, E., Quinta-Ferreira, R. M., & Martins, R. C. (2019). N–TiO2 Photocatalysts: A Review of Their Characteristics and Capacity for Emerging Contaminants Removal. *water*, 373.

GRID-Arendal. (2021). *GRID ARENDAL*. Retrieved november 10, 2021, from https://www.grida.no/resources/5625

Grieken, R. v., Marugán, J., Sordo, C., & Pablos, C. (2009). Comparison of the photocatalytic disinfection of E. coli suspensions in slurry, wall and fixed-bed reactors. *Catalysis Today*, 48-54.

Gu, Y., Zhang, B., Fu, Z., Li, J., Yu, M., Li, L., & Li, J. (2020). Poly (vinyl alcohol) modification of poly(vinylidene fluoride) microfiltration membranes for oil/water emulsion separation via an unconventional radiation method. *Journal of Membrane Science*, 118792.

Hansson, H., Kaczala, F., Marques, M., & Hogland, W. (2012). Photo-Fenton and Fenton Oxidation of Recalcitrant IndustrialWastewater Using Nanoscale Zero-Valent Iron. *International Journal of Photoenergy*.

Hasanpour, M., Motahari, S., Jing, D., & Hatami, M. (2021). Statistical analysis and optimization of photodegradation efficiency of methyl orange from aqueous solution using cellulose/zinc oxide hybrid aerogel by response surface methodology (RSM). *Arabian Journal of Chemistry*, 103401.

Hatat-Fraile, M., Liang, R., Arlos, M. J., He, R. X., Peng, P., Servos, M. R., & Zhou, Y. N. (2017). Concurrent photocatalytic and filtration processes using doped TiO2 coated quartz fiber membranes in a photocatalytic membrane reactor. *Chemical Engineering*.

Hoek, E. M., Ghosh, A. K., Huang, X., Liong, M., & Zink, J. I. (2011). Physical–chemical properties, separation performance, and fouling resistance of mixed-matrix ultrafiltration membranes. *Desalination*, 89-99.

Huang, F., Yan, A., & Zhao, H. (2016). Influences of Doping on Photocatalytic Properties of TiO2 Photocatalyst.

Huang, S.-M., Weng, C.-H., Tzeng, J.-H., Huang, Y.-Z., Anotai, J., Yen, L.-T., . . . Lin, Y.-T. (2020). Photocatalytic inactivation of Klebsiella pneumoniae by visible-light-responsive N/C-doped and N-tourmaline/palladium-C-codoped TiO2. *Chemical Engineering Journal*, 122345.

Huiru, Z., U., M. A., Yang, X., Zijing, X., F., B. E., Jianquan, L., . . . B., D. S. (2020). Visible-Light-Activated Photocatalytic Films toward Self-Cleaning Membranes.

huo, Y., jin, Y., zhu, J., & li, H. (2009). *Applied Catalysis B: Environmental*, 543–550.

Irshad, M. A., Nawaz, R., Rehman, M. Z., Imran, M., Ahmad, M. J., Ahmad, S., . . . Ali, S. (2020). Synthesis and characterization of titanium dioxide nanoparticles by chemical and green methods and their antifungal activities against wheat rust. *Chemosphere*, 127352.

Jadoun, J., Mreny, R., Saad, O., & Azaizeh, H. (2018). Fate of bacterial indicators and Salmonella in biofilm developed on ultrafiltration membranes treating secondary effluents of domestic wastewater. *scientific reports*, 18066.

Jingli, F., Xiuju, W., Zhun, M., Hao, W., Jianye, L., Zhongpeng, W., & Liguo, W. (2018). Photocatalytic ultrafiltration membranes based on visible light responsive photocatalyst: a review. *Desalination and Water Treatment*.

João, G., João, L., Eva, D., M., Q.-F. R., & C., M. R. (2019). N–TiO2 Photocatalysts: A Review of Their Characteristics and Capacity for Emerging Contaminants Removal. *water 2019*.

Julián, B.-G., Pilar, F.-I., & Sixto, M.-R. (2007). Solar Photocatalytic Detoxification and Disinfectionof Water: Recent Overview.

Kairigo, P., Ngumba, E., Sundberg, L.-R., Gachanja, A., & Tuhkanen, T. (2020). Occurrence of antibiotics and risk of antibiotic resistance evolution in selected Kenyan wastewaters, surface waters and sediments. *Science of the Total Environment*.

Kairigo, P., Ngumbac, E., Sundberg, L.-R., Gachanja, A., & Tuhkanena, T. (2020). Occurrence of antibiotics and risk of antibiotic resistance evolution in selected Kenyan wastewaters, surface waters and sediments.

Kamaludin, R., Rasdi, Z., Othman, M. H., Kadir, S. H., Nor, N. S., Khan, J., . . . Jaafar, J. (2020). Visible-Light Active Photocatalytic Dual Layer Hollow Fiber (DLHF)Membrane and Its Potential inMitigating the Detrimental Effects of Bisphenol A inWater. *membranes*, 10020032.

Karthikeyan, N., Narayanan, V., & Arumainathan, S. (2015). Degradation of Textile Effluent using Nanocomposite TiO2/SnO2 Semiconductor Photocatalysts. *International Journal of ChemTech Research*, 443 - 449.

Kenneth, O. K., Faith, J. K., Leendert, V., Akinyi, A. M., Van, L. H., Maurice, O., & Kristof, D. (2018). Occurrence, fate and removal of pharmaceuticals, personal care products and pesticides in wastewater stabilization ponds and receiving rivers in the Nzoia Basin, Kenya.

Khan, T. T., Bari, G. A., Kang, H.-J., Lee, T.-G., Park, J.-W., Hwang, H. J., . . . Jun, Y.-S. (2021). Synthesis of N-Doped TiO2 for Efficient Photocatalytic Degradation of Atmospheric NOx. *Catalysts*.

Khan, T. T., Bari, G. A., Kang, H.-J., Lee, T.-G., Park, J.-W., Hwang, H. J., . . . Jun, Y.-S. (2021). Synthesis of N-Doped TiO2 for Efficient Photocatalytic Degradation of Atmospheric NOx. *Catalysts*.

Khatua, C., Chinya, I., Saha, D., Das, S., Sena, R., & Dhar, A. (2015). MODIFIED CLAD OPTICAL FIBRE COATED WITH PVA/TIO2 NANO COMPOSITE FOR HUMIDITY SENSING APPLICATION. *International Journal on Smart Sensing and Intelligent Systems*, 813.

K'oreje, K., Vergeynst, L., Ombaka, D., Wispelaere, P. D., & c, M. O. (2016). Occurrence patterns of pharmaceutical residues inwastewater, surface water and groundwater of Nairobi and Kisumu city, Kenya. *Chemosphere*, 238.

K'oreje, K., Vergeynst, L., Ombaka, D., Wispelaere, P. D., Okoth, M., Langenhove, H. V., & Demeestere, K. (2016). Occurrence patterns of pharmaceutical residues inwastewater, surface water and groundwater of Nairobi and Kisumu city, Kenya. *Chemosphere*.

Kowalska, K., Maniakova, G., Carotenuto, M., Sacco, O., Vaiano, V., Lofrano, G., & Rizzo, L. (2019). Removal of carbamazepine, diclofenac and trimethoprim by solar driven advanced oxidation processes in a compound triangular collector based reactor A comparison between homogeneous and heterogeneo. *Chemosphere 238*.

Kutuzova, A., Dontsova, T., & Kwapinski, W. (2021). Application of TiO2-Based Photocatalysts to Antibiotics Degradation: Cases of Sulfamethoxazole, Trimethoprim and Ciprofloxacin. *catalysts*.

Kutuzova, A., Dontsova, T., & Kwapinski, W. (2021). Application of TiO2-Based Photocatalysts to Antibiotics Degradation: Cases of Sulfamethoxazole, Trimethoprim and Ciprofloxacin. *catalysts*, 728.

Lee, M. J., Ong, C. S., Lau, W., & Ng, B. C. (2015). Degradation of PVDF-based composite membrane and its impacts on membrane intrinsic and separation properties. *Journal of Polymer Engineering*, 261–268.

Li, X., Chen, Y., Hu, X., Zhang, Y., & Hu, L. (2014). Desalination of dye solution utilizing PVA/PVDF hollow fiber composite membrane modified with TiO2 nanoparticles. *Journal of Membrane Science*, 118-129.

Liao, C. H., Kang, S. F., & Wu, F. A. (2001). Hydroxyl radical scavenging role of chloride and bicarbonate ions in the H2O2/UV process. *Chemosphere*.

Lin, L., Jiang, W., Chen, L., Xu, P., & Wang, H. (2020). Treatment of Produced Water with Photocatalysis:Recent Advances, A Research Prospects. *catalysts*.

Lin, Y.-H., Weng, C.-H., Srivastav, A. L., Lin, Y.-T., & Tzeng, J.-H. (2014). Facile Synthesis and Characterization of N-Doped TiO2 Photocatalyst and Its Visible-Light Activity for Photo-Oxidation of Ethylene. *Journal of Nanomaterials*, 807394.

Liu, N., Zhu, Q., Zhang, N., Zhang, C., Kawazoe, N., Chen, G., . . . Yang, Y. (2019). Superior disinfection effect of Escherichia coli by hydrothermal synthesized TiO2-based composite photocatalyst under LED irradiation: Influence of environmental factors and disinfection mechanism. *Environmental Pollution*, 847-856.

Liu, R., Li, X., Huang, J., Pang, H., Wan, Q., Luo, K., . . . Wang, L. (2022). Synthesis and Characterization of g-C3N4/Ag3PO4/TiO2/PVDF Membrane with Remarkable Self-Cleaning Properties for Rhodamine B Removal. *International Journal of Environmental Research and Public Health*, 192315551.

Loeb, S. K., Alvarez, P. J., Brame, J. A., Cates, E. L., Choi, W., Crittenden, J., . . . Kim, J.-H. (2021). The Technology Horizon for Photocatalytic Water Treatment:Sunrise or Sunset?

M.S., A., W.I., N., H., J. A., M.A.M., I., & K., I. (2017). N-doped TiO2 Synthesised via Microwave Induced Photocatalytic on RR4 Dye Removal under LED Light Irradiation.

Mecha, A. C., Onyango, M. S., Ochieng, A., & Momba, M. N. (2019). Modelling inactivation kinetics of waterborne pathogens in municipal wastewater using ozone. *Environmental Engineering Research 2020*.

MedChemExpress. (2023, 08 20). *Master of Bioactive Molecules*. Retrieved from MCE MedChemExpress: https://www.medchemexpress.com/Sulfamethoxazole.html

Mehrabad, J. T., Partovi, M., Rad, F. A., & Khalilnezhad, R. (2019). Nitrogen doped TiO2 for efficient visible light photocatalytic dye degradation . *IRANIAN JOURNAL OF CATALYSIS*, 233-239.

Mohammed, N., Palaniandy, P., & Shaik, F. (2021). Pollutants removal from saline water by solar photocatalysis: a review of experimental and theoretical approaches. *International Journal of Environmental Analytical Chemistry*.

Molinari, R., Lavorato, C., & Argurio, P. (2021). The Evolution of Photocatalytic Membrane Reactors over the Last 20 Years: A State of the Art Perspective. *catalysts*.

Moradi, M., Naderi, A., Bahari, N., Harati, M., Rodríguez-Chueca, J., & Kalantary, R. R. (2022). Visible-light-driven photocatalytic inactivation of Escherichia coli by titanium dioxide anchored on natural pyrite. *Inorganic Chemistry Communications*, 109913.

Mourid, E. H., Mouchtari, E. M., Mersly, L. E., Benaziz, L., Rafqah, S., & Lakraimi, M. (2020). Development of a new recyclable nanocomoposite LDH-TiO2 for the degradation of antibiotic sulfamethoxazole under UVA radiation: An approach towards sunlight. *Journal of Photochemistry and Photobiology A: Chemistry*, 112530.

Mozia, S. (2010). Photocatalytic membrane reactors (PMRs) in water and wastewater treatment.A review. *Separation and Purification Technology*.

Musial, J., Mlynarczyk, D. T., & Stanisz, B. J. (2023). Photocatalytic degradation of sulfamethoxazole using TiO2-based materials – Perspectives for the development of a sustainable water treatment technology. *Science of The Total Environment*, 159122.

Musyoki, A. M., Suleiman, M. A., Mbithi, J. N., & Maingi, J. M. (2013). Water-Borne Bacterial Pathogens In Surface Waters Of Nairobi River And Health Implication To Communities Downstream Athi River. *International journal of life science & pharma research*.

Nascimbén, S. É., Zsuzsanna, L., Cecilia, H., Gangasalam, A., & Gábor, V. (2020). Photocatalytic membrane filtration and its advantages over conventional approaches in the treatment of oily wastewater: A review. *asia-pacific journal of chemical engineering*.

Natarajan, T. S., Mozhiarasi, V., & Tayade, R. J. (2021). Nitrogen Doped Titanium Dioxide (N-TiO2): Synopsis of Synthesis Methodologies, Doping Mechanisms, Property Evaluation and Visible Light Photocatalytic Applications. *photochem*.

Natarajan, T. S., Mozhiarasi, V., & Tayade, R. J. (2021). Nitrogen Doped Titanium Dioxide (N-TiO2): Synopsis of Synthesis Methodologies, Doping Mechanisms, Property Evaluation and Visible Light Photocatalytic Applications. *Photochem 2021*, 371-410.

Nazanin, R., A., P. R., & MacA., G. E. (2016). Review of functional titanium oxides. I: TiO2 and its modifications. *Progress in Solid State Chemistry*.

Ndunda, E. N., Madadi, V. O., & Wandiga, S. O. (2018). Organochlorine pesticide residues in sediment and water from Nairobi River, Kenya: levels, distribution, and ecological risk assessment.

Ngumba, E., Gachanja, A., & Tuhkanena, T. (2015). Occurrence of selected antibiotics and antiretroviral drugs in Nairobi River Basin, Kenya.

Ntozakhe, L., Taziwa, R., & HHMungondori. (2019). Influence of nitrogen doping on TiO2 nanoparticles synthesized by pneumatic spray pyrolysis method. *materials research express 6*.

OBE, L. B., Davenport, G., Mole, A., & Wyatt, M. (2020). *airora*. Retrieved september 18, 2021, from The chemistry behind Airora;Bacteria, Viruses and Vegetative Spores (Mould): https://www.airora.com/chemistry.html

Ocwelwang, A. R., & Tichagwa, L. (2014). Synthesis and Characterisation of Ag and Nitrogen Doped Tio2 Nanoparticles Supported on A Chitosan-Pvae Nanofibre Support. *International Journal of Advanced Research in Chemical Science (IJARCS)*, 28-37.

Ondijo, C., Kengara, F., & K'Owino, I. (2022). Synthesis, Characterization, and Evaluation of the Remediation Activity of Cissus quadrangularis Zinc Oxide Nanoparticle-Activated Carbon Composite on Dieldrin in Aqueous Solution. *Journal of Nanotechnology*, 2055024.

Orina, L. (2021). *water sanitatin and hygiene*. Retrieved september 24, 2020, from unicef kenya: https://www.unicef.org/kenya/water-sanitation-and-hygiene

Otieno, K. K., Jebiwot, K. F., Leendert, V., Akinyi, A. M., Van, L. H., Maurice, O., & Kristof, D. (2018). Occurrence, fate and removal of pharmaceuticals, personal care products and pesticides in wastewater stabilization ponds and receiving rivers in the Nzoia Basin, Kenya. *Science of the Total Environment*.

Pangestuti, A. D., & Gunlazuardi, J. (2018). Preparation and characterization of nitrogen-doped highly ordered titanium dioxide nanotubes (N-doped-HOTN): How far it will improve toward the visible light response and why? *AIP Conference Proceedings 2023, 020109*.

Raffaele, M., Cristina, L., & Pietro, A. (2021). The Evolution of Photocatalytic Membrane Reactors over the Last 20 Years: A State of the Art Perspective. *catalysts*.

Rahimi, N., Pax, R. A., & Gray, E. M. (2016). Review of functional titanium oxides. I: TiO2 and its modifications. *Progress in Solid State Chemistry*.

Rani, C. N., & Karthikeyan, S. (2018). Photocatalytic degradation of aqueous phenanthrene in a slurry photocatalytic reactor. *Current Science*, 1732-1740.

Rasoulnezhad, H., Hosseinzadeh, G., Hosseinzadeh, R., & Ghasemian, N. (2018). Preparation of transparent nanostructured N-doped TiO2 thin films by combination of sonochemical and CVD methods with visible light photocatalytic activity. *Journal of Advanced Ceramics*, 185-196.

Regmi, C., Joshi, B., Ray, S. K., Gyawali, G., & Pandey, R. P. (2018). Understanding Mechanism of Photocatalytic Microbial Decontamination of Environmental Wastewater. *frontiers in chemistry*.

Reijnders, L. (2009). The release of TiO2 and SiO2 nanoparticles from nanocomposites. *Polymer Degradation and Stability*.

Ren, S., Guo, N., Li, J., & Wang, Y. (2023). Integration of antibacterial and photocatalysis onto polyethersulfone membrane for fouling mitigation and contaminant degradation. *Journal of Environmental Chemical Engineering*, 110401.

Ribao, P., Rivero, M. J., & Ortiz, I. (2017). TiO2 structures doped with noble metals and/or graphene oxide to improve the photocatalytic degradation of dichloroacetic acid. *Environmental Photocatalysis And Photochemistry For A Sustainable World: A Big Challenge*.

Rincón, A.-G., & Pulgarin, C. (2004). Effect of pH, inorganic ions, organic matter and H2O2 on E. coli K12 photocatalytic inactivation by TiO2 Implications in solar water disinfection. *Applied Catalysis B: Environmental*, 283–302.

Rivero, M. J., Ribao, P., Gomez-Ruiz, B., Urtiaga, A., & Ortiz, I. (2020). Comparative performance of TiO2-rGO photocatalyst in the degradation of dichloroacetic and perfluorooctanoic acids. *Separation and Purification Technology*.

S.N., M., W.S., O., & K.G., N. (2015). Photo Catalytic Inactivation of Escherichia coli Using Titanium (IV) Oxide- Tungsten (VI) Oxide Nanoparticles Composite. *International Journal of Photocatalysis*, 204-211.

Sakarkar, S., Muthukumaran, S., & Jegatheesan, V. (2020). Evaluation of polyvinyl alcohol (PVA) loading in the PVA/titanium dioxide (TiO2) thin film coating on polyvinylidene fluoride (PVDF) membrane for the removal of textile dyes. *Chemosphere*.

Sakarkar, S., Muthukumaran, S., & Jegatheesan, V. (2020). Evaluation of polyvinyl alcohol (PVA) loading in the PVA/titanium dioxide (TiO2) thin film coating on polyvinylidene fluoride (PVDF) membrane for the removal of textile dyes. *Chemosphere*, 127144.

Sakarkar, S., Muthukumaran, S., & Jegatheesan, V. (2021). Tailoring the Effects of Titanium Dioxide (TiO2) and Polyvinyl Alcohol (PVA) in the Separation and Antifouling Performance of Thin-Film Composite Polyvinylidene Fluoride (PVDF) Membrane. *membranes*.

Sarafraz, M., Sadeghi, M., Yazdanbakhsh, A., Amini, M. M., Sadani, M., & Eslami, A. (2020). Enhanced photocatalytic degradation of ciprofloxacin by black Ti3+/N-TiO2 under visible LED light irradiation: Kinetic, energy consumption, degradation pathway, and toxicity assessment. *Process Safety and Environmental Protection*, 261-272.

Scorrano, S., Mergola, L., Bello, M. P., Lazzoi, M. R., Vasapollo, G., & Sole, R. D. (2015). Molecularly Imprinted Composite Membranes for Selective Detection of 2-Deoxyadenosine in Urine Samples. *International Journal of Molecular Sciences*, 13746-13759.

Selvam, K., Balachandran, S., Velmurugan, R., & Swaminathan, M. (2012). Mesoporous nitrogen doped nano titania—A green photocatalyst for the effective reductive cleavage of azoxybenzenes to amines or 2-phenyl indazoles in methanol. *Applied Catalysis A: General*, 213– 222.

Selvaraj, A., Parimiladevi, R., & Rajesh, K. B. (2013). Synthesis of Nitrogen Doped Titanium Dioxide (TiO2) and its Photocatalytic Performance for the Degradation of Indigo Carmine Dye. *Journal of enviromental and nanotechnology*, 35-41.

Serna-Carrizales, J. C., Zárate-Guzmán, A. I., Aguilar-Aguilar, A., Forgionny, A., Bailón-García, E., Flórez, E., . . . Ocampo-Pérez, R. (2023). Optimization of Binary Adsorption of Metronidazole and Sulfamethoxazole in Aqueous Solution Supported with DFT Calculations. *Processes*, 1009.

Shang, K., Morent, R., Wang, N., Wang, Y., Peng, B., Jiang, N., . . . Li, J. (2022). Degradation of sulfamethoxazole (SMX) by water falling film DBD Plasma/Persulfate: Reactive species identification and their role in SMX degradation. *Chemical Engineering Journal*, 133916.

Shon, H., Phuntsho, S., & Vigneswaran, S. (2007). Effect of Photocatalysis on the Membrane Hybrid System for Wastewater Treatment.

Song, W., Li, J., Wang, Z., Fu, C., Zhang, X., Feng, J., . . . Song, Q. (2020). Degradation of bisphenol A by persulfate coupled with dithionite: Optimization using response surface methodology and pathway. *Science of The Total Environment*, 134258.

Sontakke, S., Modak, J., & Madras, G. (2011). Effect of inorganic ions, H2O2 and pH on the photocatalytic inactivation of Escherichia coli with silver impregnated combustion synthesized TiO2 catalyst. *Applied Catalysis B: Environmental*, 453– 459.

Subramaniam, M. N., Goh, P. S., Kanakaraju, D., Lim, J. W., Lau, W. J., & Ismail, A. F. (2021). Photocatalytic membranes: a new perspective for persistent organic pollutants removal. *Water Environment And Recent Advances In Pollution Control Technologies*.

Subramaniam, M. N., Goh, P.-S., Lau, W.-J., Ng, B.-C., & Ismail, A. F. (2019). Development of nanomaterial-based photocatalytic membrane for organic pollutants removal. *Advanced Nanomaterials for Membrane Synthesis and Its Applications*.

Survey, U. G. (2019, october 25). *usgs*. Retrieved november 15, 2021, from https://www.usgs.gov/media/images/distribution-water-and-above-earth

Tamirat, A. G., Rick, J., Dubale, A. A., Su, W.-N., & Hwang, B.-J. (2016). Using hematite for photoelectrochemical water splitting: a review of current progress and challenges. *nanoscale horizons*.

Tao, X., Mo, W., & Tong, W. (2019). Effects of N Doping on the Microstructures and Optical Properties of TiO2. *Journal of Wuhan University of Technology-Mater*, 55-63.

Teixeira, S., Martins, P., & Lanceros-Méndez, S. (2015). Reusability of photocatalytic TiO2 and ZnO nanoparticles immobilized in poly(vinylidene difluoride)-co-trifluoroethylene. *Applied Surface Science*, 497-504.

Thuy, L. N., Hanh, N. T., Pham, T.-D., Tran, D.-T., Chu, H. T., Dang, H. T., . . . Bruggen, B. V. (2020). UV–Visible Light Driven Photocatalytic Degradation of Ciprofloxacin by N,S Co-doped TiO2: The Effect of Operational Parameters. *Topics in Catalysis*, 985–995.

Tung, T., Ananpattarachai, J., & Kajitvichyanukul, P. (2018). Photocatalytic membrane reactors for water and wastewater treatment applications: process factors and operating conditions review. *International Association of Lowland Technology*.

Vaez, M., Moghaddam, A. Z., & Alijani, S. (2012). Optimization and Modeling of Photocatalytic Degradation of Azo Dye Using a Response Surface Methodology (RSM) Based on the Central Composite Design with Immobilized Titania Nanoparticles. *Industrial & Engineering Chemistry Research*, 4199–4207.

Wahyuni, E. T., Rahmaniati, T., Hafidzah, A. R., Suherman, S., & Suratman, A. (2021). Photocatalysis over N-doped TiO2 driven by visible light as a new method for Pb(II) removal. *catalysts*.

Wang, C., Liu, H., & Qu, Y. (2013). TiO2-Based Photocatalytic Process for Purification of Polluted Water: Bridging Fundamentals to Applications. *Journal of Nanomaterials*.

Wang, E., He, T., Zhao, L., Chenc, Y., & Cao, Y. (2011). Improved visible light photocatalytic activity of titania doped with tin and nitrogen. *Journal of Materials Chemistry*, 144-150.

Wang, H., & Ding, K. (2022). Effect of Self-Made TiO2 Nanoparticle Size on the Performance of the PVDF Composite Membrane in MBR for Landfill Leachate Treatment. *membranes*, 12020216.

Wang, J., Zhu, W., Zhang, Y., & Liu, S. (2007). An Efficient Two-Step Technique for Nitrogen-Doped Titanium Dioxide Synthesizing: Visible-Light-Induced Photodecomposition of Methylene Blue. *The Journal of Physical Chemistry*, 1010-1014.

Wang, N., Li, X., Yang, Y., Zhou, Z., Shang, Y., & Zhuang, X. (2020). Photocatalytic degradation of sulfonamides by Bi2O3-TiO2/PAC ternary composite: Mechanism, degradation pathway. *Journal of Water Process Engineering*, 101335.

Wanichaya, M., & Wisanu, P. (2011). Synthesis and characterization of nitrogen-doped TiO2 and its photocatalytic activity enhancement under visible light. *Energy Procedia 9*.

Warmadewanthi, & Bachtiar, Y. F. (2019). Study of struvite crystallization from fertilizer industry wastewater by using fluidized bed reactor. *MATEC Web of Conferences.*

Wu, C. H., Kuo, C. Y., Dong, C. D., Chen, C. W., & Lin, Y. L. (2019). Removal of sulfonamides from wastewater in the UV/TiO2 system: effects of pH and salinity on photodegradation and mineralization. *Water Science & Technology*, 349-355.

Wu, Z., Liang, Y., Yuan, X., Zou, D., Fang, J., Jiang, L., . . . Xiao, Z. (2020). MXene Ti3C2 derived Z–scheme photocatalyst of graphene layers anchored TiO2/g–C3N4 for visible light photocatalytic degradation of refractory organic pollutants. *Chemical Engineering Journal*, 124921.

Xie, X., Li, S., Zhang, H., Wang, Z., & Huang, H. (2019). Promoting charge separation of biochar-based Zn-TiO2/pBC in the presence of ZnO for efficient sulfamethoxazole photodegradation under visible light irradiation. *Science of The Total Environment*, 529-539.

Yang, G., Jiang, Z., Shi, H., Xiao, T., & Yan, Z. (2010). Preparation of highly visible-light active N-doped TiO2 photocatalyst. *Journal of Materials Chemistry*, 5301-5309.

Yu, J.-G., Yu, H.-G., Cheng, B., Zhao, X.-J., Yu, J. C., & Ho, W.-K. (2003). The Effect of Calcination Temperature on the Surface Microstructure and Photocatalytic Activity of TiO2 Thin Films Prepared by Liquid Phase Deposition. *The Journal of Physical Chemistry*, 13871-13879.

Zarei, N., & Behnajady, M. A. (2019). Optimization Of Photocatalytic Activity Of Mg/Zno Nanoparticles In The Removal Of A Model Contaminant using response surface methodology. *Environmental Engineering and Management Journal*, 385-395.

Zhang, B., Xu, X., & Zhu, L. (2018). Activated sludge bacterial communities of typical wastewater treatment plants: distinct genera identification and metabolic potential differential analysis.

Zhang, S., Gao, H., Huang, Y., Wang, X., Hayat, T., Li, J., . . . Wang, X. (2018). Ultrathin g-C3N4 nanosheets coupled with amorphous Cu-doped FeOOH nanoclusters as 2D/0D heterogeneous catalysts for water remediation. *Environmental Science: Nano*, 1179-1190.

Zhang, X., & Zhao, Y. (2019). Optimization of photocatalytic degradation of dye wastewater by CuFe2O4/AgBr composite using response surface methodology. *Materials Research Express*, 036109.

Zhang, Y., Du, F., Yan, X., Jin, Y., Zhu, K., Wang, X., . . . Wei, Y. (2014). Improvements in the Electrochemical Kinetic Properties and Rate Capability of Anatase Titanium Dioxide Nanoparticles by Nitrogen Doping. *applied materials and interfaces*, 4458−4465.

APPENDICES

Appendix I: Control Experiments

Table A1: TiO_2-PVDF degradation, TOC and flux

pH (SMX 6mg/L)	Time duration	Absorbance	Quantity remaining	% SMX removed	TOC remaining	%TOC removed	Flux/7cmD/Hr	Relative flux
4	25	0.0252	4.2	30	3.65	11.4	652.8	0.9079
	50	0.02	3.1803	47	2.82	31.55	604.8	0.8411
	75	0.155	2.298	61.7	2.12	48.54	559.2	0.7777
	100	0.0122	1.651	72.48	1.57	61.89	537.6	0.7477
7	25	0.0261	4.3765	27.06	3.38	17.96	609.6	0.8478
	50	0.0209	3.3569	44.05	2.44	40.78	518.4	0.721
	75	0.0163	2.4549	59.09	2.03	50.73	516	0.7176
	100	0.0134	1.8863	68.56	1.47	64.32	501.6	0.6976
10	25	0.0293	5.0039	16.6	4.06	1.45	595.2	0.8278
	50	0.0243	4.0235	32.94	3.81	7.52	540	0.751
	75	0.0207	3.3176	44.71	3.61	12.38	501.6	0.6968
	100	0.0177	2.7294	54.51	2.18	47.08	499.2	0.6942

SMX conc. (pH 7)	Time duration	Absorbance	Quantity remaining	% SMX removed	TOC remaining	%TOC removed	Flux/7cmD/Hr	Relative flux
6mg/L	25	0.0261	4.3765	27.06	3.38	17.96	609.6	0.8478
	50	0.0209	3.3569	44.05	2.44	40.78	518.4	0.721
	75	0.0163	2.4549	59.09	2.03	50.73	516	0.7176
	100	0.0134	1.8863	68.56	1.47	64.32	501.6	0.6976
10mg/L	25	0.0448	8.0431	19.57	4.65	4.12	576	0.8011
	50	0.0432	7.7294	22.71	4.54	6.39	489.6	0.6809
	75	0.0316	6.3373	36.63	4.21	13.19	465.6	0.6475
	100	0.0252	4.2	58	4.12	15.05	432	0.6008
14mg/L	25	0.0651	12.0235	14.11	6.24	14.87	504	0.7009
	50	0.0537	9.7882	30.08	5.68	22.5	468	0.6509
	75	0.0452	8.1216	41.99	5.41	26.19	432	0.6008
	100	0.0379	6.6902	52.21	5.35	27.01	417.6	0.5808

Table A2: TiO_2-PVDF disinfection and flux

pH($10.4x10^8$CFU/l))	Time duration	Remaining cells	CFU/Liter remaining	% *E.coli* removed	Flux/7cmD/Hr	Relative flux
4	25	12	$1.2x10^8$	88.46	556.8	0.7744
	50	3	$3x10^7$	97.11	223.2	0.3104

	75	0	0	100	187.2	0.2604
	100	0	0	100	177.6	0.247
7	25	9	$9x10^7$	91.34	583.2	0.8111
	50	2	$2x10^7$	98.08	266.4	0.3705
	75	0	0	0	216	0.3004
	100	0	0	0	218.4	0.3038
10	25	14	$1.4x10^8$	86.54	535.2	0.7444
	50	3	$3x10^7$	97.12	208.8	0.2904
	75	0	0	0	182.4	0.2537
	100	0	0	0	175.2	0.2437
***E.coli* conc.(pH 7)**	**Time duration**	**Quantity remaining**	**CFU/Liter remaining**	**%*E.coli* Removed**	**Flux/7cmD/Hr**	**Relative flux**
$10.4x10^8$ CFU/l	25	9	$9x10^7$	91.34	583.2	0.8111
	50	2	$2x10^7$	98.08	266.4	0.3705
	75	0	0	0	216	0.3004
	100	0	0	0	218.4	0.3038
$5.2x10^8$ CFU/l	25	4	$4x10^7$	92.31	595.2	0.8278
	50	1	$1x10^7$	98.08	314.4	0.4373
	75	0	0	100	259.2	0.3605
	100	0	0	100	230.4	0.3204

$2.6x10^8$ CFU/l	25	2	$2x10^7$	96.15	633.6	0.8812
	50	0	0	100	388.8	0.5408
	75	0	0	100	304.8	0.4239
	100	0	0	100	295.2	0.4106

Table A3: PVDF degradation and flux

pH (SMX 6mg/L)	**Time duration**	**Absorbance**	**Quantity remaining**	**% SMX removed**	**TOC remaining**	**%TOC removed**	**Flux/7cmD/Hr**	**Relative flux**
4	25	0.0303	5.2	13.33	3.81	7.52	648	0.808
	50	0.0282	4.7882	20.2	3.45	16.26	576	0.7182
	75	0.028	4.749	20.85	3.1	24.75	544.8	0.6793
	100	0.0222	3.6118	39.8	3.07	25.48	544.8	0.6793
7	25	0.0317	5.4745	8.76	3.75	8.98	652.8	0.814
	50	0.0276	4.6706	22.16	3.61	12.37	585.6	0.7301
	75	0.0248	4.1216	31.31	3.27	20.63	547.2	0.6823
	100	0.0225	3.6706	38.82	3.02	26.69	540	0.6733
10	25	0.0312	5.3765	10.39	3.79	8.01	655.2	0.817
	50	0.0278	4.7098	21.5	3.44	16.5	590.4	0.7362
	75	0.027	4.5529	24.12	2.99	27.43	547.2	0.6823

	100	0.023	3.7686	37.19	3.38	17.96	542.4	0.6763
SMX conc. (pH 7)	**Time duration**	**Absorbance**	**Quantity remaining**	**% SMX removed**	**TOC remaining**	**%TOC removed**	**Flux/7cmD/Hr**	**Relative flux**
6mg/L	25	0.0317	5.4745	8.76	3.75	8.98	652.8	0.814
	50	0.0276	4.6706	22.16	3.61	12.37	585.6	0.7301
	75	0.0248	4.1216	31.31	3.27	20.63	547.2	0.6823
	100	0.0225	3.6706	38.82	3.02	26.69	540	0.6733
10mg/L	25	0.0514	9.3373	6.63	4.81	0.82	585.6	0.7301
	50	0.0478	8.6314	13.69	4.81	0.82	504	0.6284
	75	0.0458	8.2392	17.61	4.64	4.32	480	0.5985
	100	0.0445	7.9843	20.16	4.43	8.66	439.2	0.5476
14mg/L	25	0.0701	13.0039	7.115	7.16	2.32	556.8	0.6943
	50	0.0681	12.6118	9.92	6.14	16.23	424.8	0.5268
	75	0.0654	12.0824	13.7	5.96	18.69	465.6	0.5805
	100	0.0634	11.6902	16.5	5.93	19.1	391.2	0.4878

Table A4: PVDF disinfection and flux

pH(10.4x10^8 CFU/l)	**Time duration**	**Remaining cells**	**CFU/Liter remaining**	**% *E.coli* removed**	**Flux/7cmD/Hr**	**Relative flux**
4	25	79	7.9x10^8	24.04	458.4	0.5716

	50	70	$7x10^8$	32.69	206.4	0.25
	75	54	$5.4x10^8$	48.08	175.2	0.2185
	100	30	$3x10^8$	71.15	177.6	0.2214
7	25	80	$8x10^8$	23.08	482.4	0.6015
	50	67	$6.7x10^8$	35.58	218.4	0.2723
	75	60	$6x10^8$	42.31	177.6	0.2214
	100	31	$3.1x10^8$	70.19	170.4	0.2125
10	25	81	$8.1x10^8$	22.11	465.6	0.5678
	50	71	$7.1x10^8$	31.73	201.6	0.2514
	75	62	$6.2x10^8$	40.38	184.8	0.2304
	100	34	$3.4x10^8$	67.31	160.8	0.2005
***E.coli* conc.(pH 7)**	**Time duration**	**Remaining cells**	**CFU/Liter remaining**	**%*E.coli* Removed**	**Flux/7cmD/Hr**	**Relative flux**
$10.4x10^8$ CFU/l	25	80	$8x10^8$	23.08	482.4	0.6015
	50	67	$6.7x10^8$	35.58	218.4	0.2723
	75	60	$6x10^8$	42.31	177.6	0.2214
	100	31	$3.1x10^8$	70.19	170.4	0.2125
$5.2x10^8$ CFU/l	25	36	$3.6x10^8$	30.77	506.4	0.6314
	50	25	$2.5x10^8$	51.92	280.8	0.3501
	75	19	$1.9x10^8$	63.46	213.6	0.2656

	100	11	$1.1x10^8$	78.85	220.8	0.2753
$2.6x10^8$ CFU/l	25	13	$1.3x10^8$	50	571.8	0.713
	50	9	$9x10^7$	65.38	338.4	0.4219
	75	5	$5x10^7$	80.77	312	0.389
	100	3	$3x10^7$	88.46	242.4	0.3022

Appendix II: Experimental Photos

Figure A1: Cross filtration setup top view

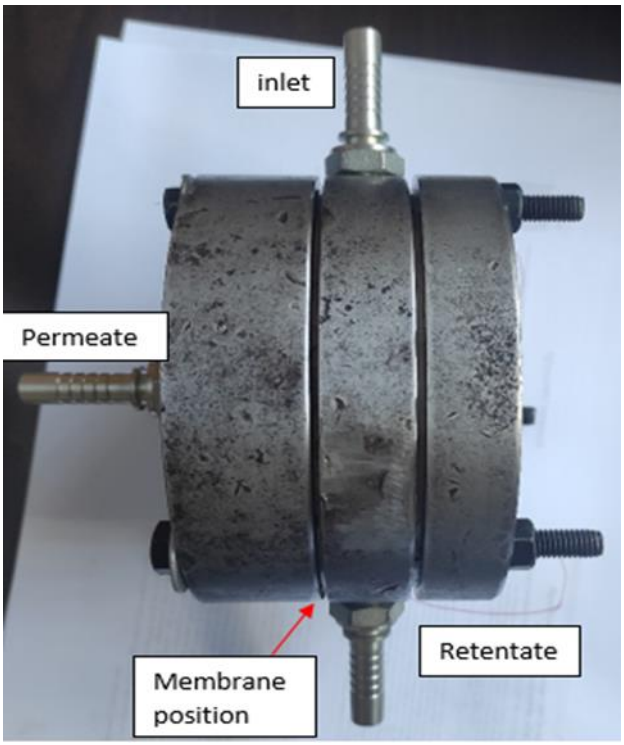

Figure A2: Cross filtration set-up side view.

Figure A3: Manual solar tracking with parabolic dish concentrator and cross filtration set-up.

Figure A4: Experiment in progress

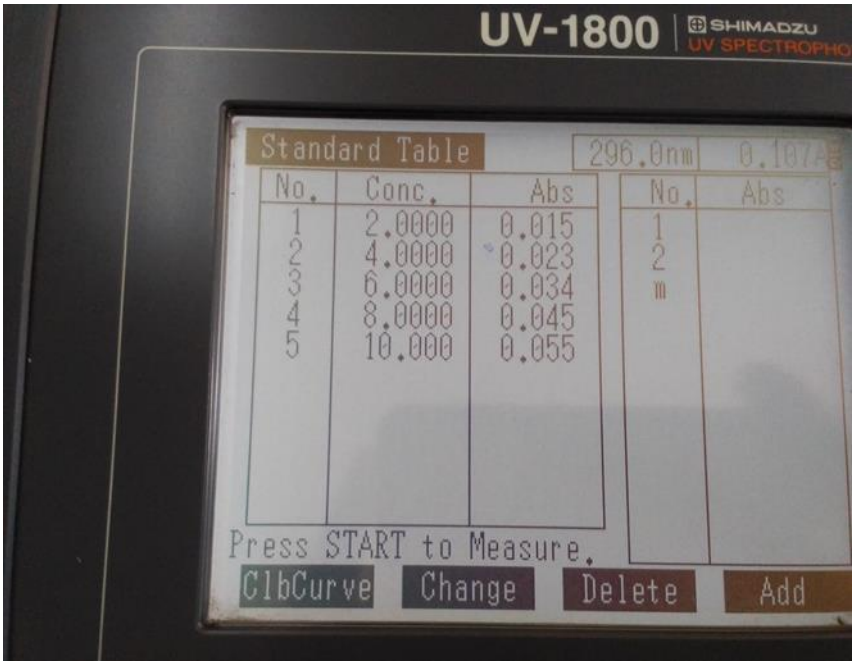

Figure A5: SMX standard absorbance curve data.

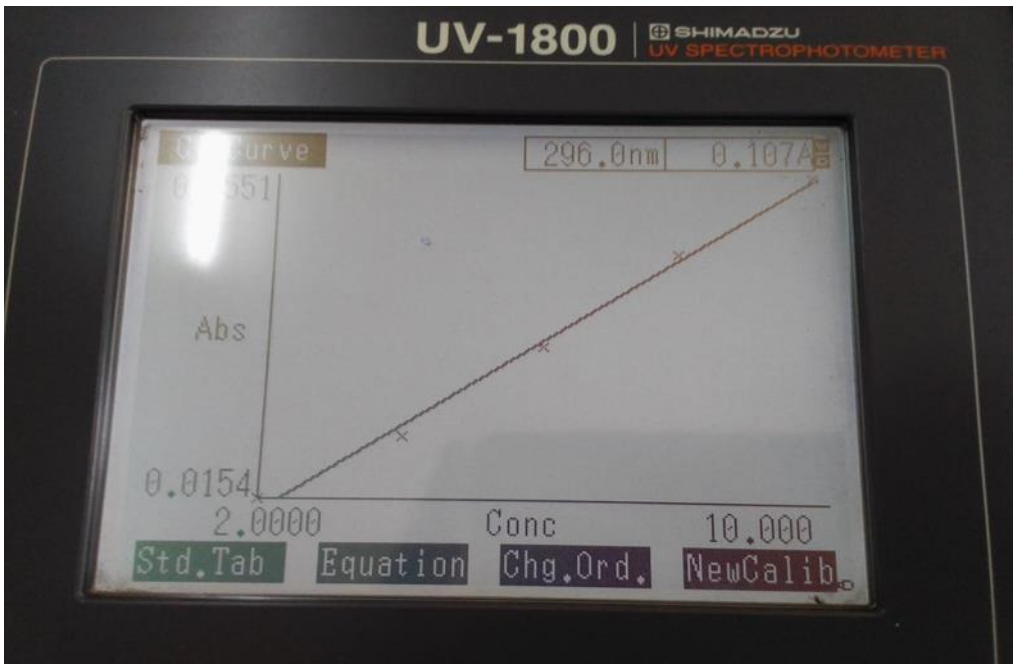

Figure A6: Standard absorbance curve for SMX.

Figure A7: Culturing of *E.coli* process

Appendix III: Similarity Index Report

Nelson Kipchumba_MSC/CE/5520/21_ Msc Thesis

by Nelson Kipchumba

Submission date: 28-Sep-2023 08:16AM (UTC-0700)
Submission ID: 2179599252
File name: Thesis_final_draft_1.docx (10.43M)
Word count: 28978
Character count: 164605

Nelson Kipchumba_MSC/CE/5520/21_Msc Thesis

ORIGINALITY REPORT

12%	9%	7%	4%
SIMILARITY INDEX	INTERNET SOURCES	PUBLICATIONS	STUDENT PAPERS

PRIMARY SOURCES

1	Submitted to Durban University of Technology Student Paper	1%
2	www.coursehero.com Internet Source	1%
3	ir.mu.ac.ke:8080 Internet Source	1%
4	hdl.handle.net Internet Source	<1%
5	Submitted to Tshwane University of Technology Student Paper	<1%
6	etd.aau.edu.et Internet Source	<1%
7	www.mdpi.com Internet Source	<1%
8	Juan Jiang, Boya Ma, Chunwei Yang, Xiaoyue Duan, Qian Tang. "Fabrication of anti-fouling and photocleaning PVDF microfiltration	<1%